

CHAPTER VI

PREDICTION TECHNIQUES

6.1 INTRODUCTION

6.1.1 Purpose

This chapter provides a guide to prediction methods and related propagation results for the evaluation of earth-space paths operating above 10 GHz. The topics covered are:

Gaseous Attenuation

Rain Attenuation

Cloud, Fog, Sand and Dust Attenuation

Signal Fluctuations and Low Angle Fading

Depolarization Effects

Bandwidth Coherence

Sky Noise

The techniques described here have been developed from recent ongoing NASA supported studies and from the relevant published literature. These techniques represent the state of knowledge of the adverse effects of the earth's atmosphere on reliable earth-space transmissions above 10 GHz.

This chapter provides propagation data in a format suitable for use by earth-space link system designers operating in the frequency range from 10 to 100 GHz. In this frequency range the troposphere can have a significant effect on the carrier-to-noise ratio of a propagating wave. Typically, the troposphere attenuates and depolarizes the carrier signal and adds broadband amplitude and

phase noise to the signal. The resulting carrier-to-noise ratio reduction reduces the allowable data rate for a given bit error rate (digital systems) and the quality of transmission (analog systems). In the most severe cases the medium will significantly attenuate the carrier and destroy the transmission capabilities of the link (termed a **link** outage). The frequency of occurrence and average outage time per year are usually of most interest to system designers. Propagation studies to date now allow the predictions to be made with a high degree of certainty and have developed means to reduce the frequency and length of these outages.

6.1.2 Organization of This Chapter

The remainder of this chapter is arranged in six relatively independent sections covering the key topics related to the interaction of the troposphere and earth-space propagation paths. Each section presents a description of selected techniques and provides sample calculations of the techniques applied to typical communications systems parameters. A guide to the sample calculations is given in Table 6.1-1.

6.1.3 Frequency Bands for Earth-Space Communication

Within the guidelines established by the International Telecommunication Union (**ITU**) for Region 2 (includes U.S. and Canada), the Federal Communications Commission (FCC) in the U.S. and the Department of Communications (**DOC**) in Canada regulate the **earth-space** frequency allocations. In most cases, the FCC and DOC regulations are more restrictive than the ITU regulations.

The services which operate via earth-space links are listed in Table 6.1-2. The definitions of each of these services are given in the ITU Radio Regulations. The specific frequency allocations for these services are relatively fixed, but modifications can be enacted at **World** Administrative Radio Conferences based on the proposals of ITU member countries.

Table 6.1-1. Guide to Sample Calculations

Paragraph Number	Description	Page Number
6.2.4	Relative humidity to water vapor density conversion	6-16
6.2.5	Gaseous Attenuation calculation	6-16
6.3.2.2	Cumulative rain attenuation distribution using the Global Model	6-29
6.3.2.4	Cumulative rain attenuation distribution using the CCIR Model	6-35
6.3.3.2	Cumulative rain attenuation distribution by distribution extension	6-41
6.3.5.1	Fade duration and return period	6-50
6.4.3.3	Estimation of fog attenuation	6-72
6.5.6.1	Variance of signal amplitude fluctuations	6-101
6.5.6.2	Phase and angle-of-arrival variations	6-103
6.5.6.3	Received signal gain reduction	6-103
6.6.2.1.1	CCIR Approximation for rain depolarization	6-106
6.6.3.3	CCIR estimate for ice depolarization	6-119
6.6.5	Prediction of depolarization statistics	6-122
6.7.3.2	Group delay and phase delay	6-131
6.8.3	Sky noise due to clear sky and rain	6-136
6.8.5	Sky noise due to clouds	6-139
6.9.2	Uplink Noise in Satellite Antenna	6-343

A review of the Radio Regulations indicates that most of the frequency spectrum above 10 GHz is assigned to the satellite services or the radio astronomy service. This does not mean that the FCC or DOC will utilize them as such, but it does highlight the potential for use of these frequency bands. Figure 6.1-1 shows those frequency segments not assigned for potential use by the services listed in Table 6.1-2 (**ITU-1980**).

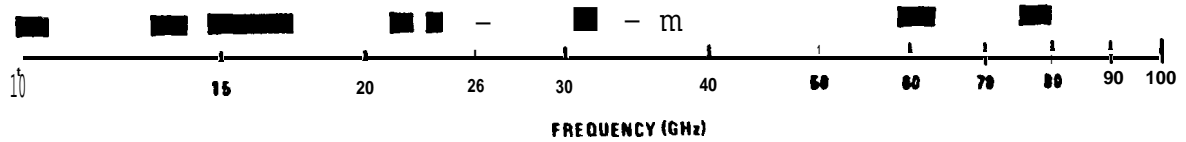


Figure 6.1-1. Frequencies Not Allocated Primarily for Earth-Space Transmissions in Region 2

Table 6.1-2. Telecommunication Services Utilizing Earth-Space Propagation Links

Fixed Satellite
Mobile Satellite
Aeronautical Mobile Satellite
Maritime Mobile Satellite
Land Mobile Satellite
Broadcasting Satellite
Radionavigation Satellite
Earth Exploration Satellite
Meteorological Satellite
Amateur Satellite
Standard Frequency Satellite
Space Research
Space Operations
Radio Astronomy

6.1.4 Other Propagation Effects Not Addressed in This Chapter

6.1.4.1 Ionospheric Effects. The ionosphere generally has a small effect on the propagation of radio waves in the 10 to 100 GHz range, whatever effects do exist (scintillation, absorption, variation in the angle of arrival, delay, and depolarization) arise due to the interaction of the radio wave with the free electrons, electron density irregularities and the earth's magnetic field. The density of electrons in the ionosphere varies as a function of geomagnetic latitude, diurnal cycle, yearly cycle, and solar cycle (among others). Fortunately, most U.S. ground station-satellite paths pass through the midlatitude electron density region, which is the most homogeneous region. This yields only a small effect on propagation. Canadian stations may be affected by the auroral region electron densities which are normally more irregular. A more complete discussion of the effects is included in Report 263-6 of **CCIR Volume VI** 1986a) .

A mean vertical one-way attenuation for the ionosphere at 15 GHz for the daytime is typically 0.0002 **dB (Millman-1958)**, the amplitude scintillations are generally not observable (Crane-1977) and the transit time delay increase over the free space propagation time delay is of the order of 1 nanosecond (**Klobuchar-1973**). Clearly for most systems operating above 10 GHz these numbers are sufficiently small that other system error budgets will be much larger than the ionospheric contributions.

The one ionospheric effect which might influence wide bandwidth systems operating above 10 GHz is phase dispersion. This topic is discussed in Section 6.7.

6.1.4.2 Tropospheric Delays. Highly accurate satellite range, range-rate and position-location systems will need to remove the propagation group delay effects introduced by the troposphere. Extremely high switching rate TDMA systems require these corrections. The effects arise primarily due to the oxygen and water vapor in the lower troposphere. Typical total additional

propagation delay errors have been measured to be of the order of 8 nanoseconds (**Hopfield-1971**).

Estimation techniques, based on the measurement of the surface pressure, temperature and relative humidity have been developed (**Hopfield-1971**, Bean and **Dutton-1966**, **Segal** and Barrington-1977) which can readily reduce this error to less than 1 nanosecond. In addition, algorithms for range (**Marini-1972a**) and range-rate (**Marini-1972b**) have been prepared to reduce tropospheric contributions to satellite tracking errors.

Since this topic is quite specialized and generally results in an additional one-way delay of less than 10 nanoseconds it is not addressed further in this report. An overview of this subject and additional references are available in CCIR Report 564-3 (**1986b**), and Flock, Slobin and Smith (1982).

6.2 PREDICTION OF GASEOUS ATTENUATION ON EARTH-SPACE PATHS

The mean attenuation of gases on earth-space paths in the 10 to 100 GHz frequency range has been theoretically modeled and experimentally measured. Above 20 GHz gaseous absorption can have a significant effect on a communication system design depending on the specific frequency of operation. Because of the large frequency dependence of the gaseous absorption, an earth-space communication system designer should avoid the high absorption frequency bands. Alternatively, designers of secure short-haul terrestrial systems can utilize these high attenuation frequency bands to provide system isolation.

6.2.1 Sources of Attenuation

In the frequency range from 10 to 100 GHz the water vapor absorption band centered at 22.235 GHz and the oxygen absorption lines extending from 53.5 to 65.2 GHz are the only significant contributors to gaseous attenuation. The next higher frequency absorption bands occur at 118.8 GHz due to oxygen and 183 GHz due to water vapor. The absorption lines are frequency broadened by

collisions at normal atmospheric pressures (low elevations) and sharpened at high altitudes. Thus the total attenuation due to gaseous absorption is ground station altitude dependent.

6.2.2 Gaseous Attenuation

6.2.2.1 One-Way Attenuation Values Versus Frequency. The Zenith one-way attenuation for a moderately humid atmosphere (7.5 g/m³ surface water vapor density) at various ground station altitudes (starting heights) above sea level is presented in Figure 6.2-1 and Table 6.2-1. These curves were computed (Crane and Blood, 1979) for temperate latitudes assuming the U.S. Standard Atmosphere, July, 45 N. latitude. The range of values indicated in Figure 6.2-1 refers to the peaks and valleys of the fine absorption lines. The range of values at greater starting heights (not shown) is nearly two orders of magnitude (Leibe-1975).

Table 6.2-1. Typical One-Way Clear Air Total Zenith Attenuation Values, A_c' (dB) (Mean Surface Conditions 21°C, 7.5 g/m³ H₂O; U.S. Std. Atmos. 45°N., July)

Frequency	ALTITUDE				
	0km*	0.5km	1.0km	2.0km	4.0km
10 GHZ	.053	.047	.042	.033	.02
15	.084	.071	.061	.044	.023
20	.28	.23	.18	.12	.05
30	.24	.19	.16	.10	.045
40	.37	.33	.29	.22	.135
80	1.30	1.08	.90	.62	.30
90	1.25	1.01	.81	.52	.22
100	1.41	1.14	.92	.59	.25

*1 km = 3281 feet

Figure 6.2-1 also shows two values for the standard deviation of the clear air zenith attenuation as a function of frequency. The larger value was calculated from 220 measured atmosphere profiles, spanning all seasons and geographical locations (Crane-1976). The smaller value applies after the mean surface temperature and humidity have been taken into account by making the corrections given below.

6.2.2.1.1 Dependence on Ground Station Altitude. The compensation for ground station elevation can be done to first order by linearly interpolating between the curves in Figure 6.2-1. The zenith **one-way** attenuation for typical ground station altitudes, found **in this way**, is tabulated in Table 6.2-1 for easy reference.

6.2.2.1.2 Dependence on Water Vapor Content. The water vapor content is the most variable component of the atmosphere. Therefore, for arid or humid regions, a correction should be made based on the expected mean values of water vapor **content when** utilizing frequencies between 10 and 50 GHz. This correction to the total zenith attenuation is linearly related to the mean local water vapor density at the surface p :.

$$\Delta A_{c1} = b_p (p_0 - 7.5 \text{ g/m}^3) \quad (6.2-1)$$

where A_{c1} is an additive correction to the zenith clear air attenuation (given by Figure 6.2-1 and Table 6.2-1) that accounts for the difference between the mean local surface water vapor density and 7.5 g/m^3 . The coefficient b_p is frequency dependent and is given by Figure 6.2-2 and Table 6.2-2 (Crane and Blood, 1979). The accuracy of this correction factor is greatest for sea level altitude.

The US and Canadian weather services generally measure relative humidity or the partial pressure of water vapor. The technique for converting these values to p is given in Section 6.2.5.

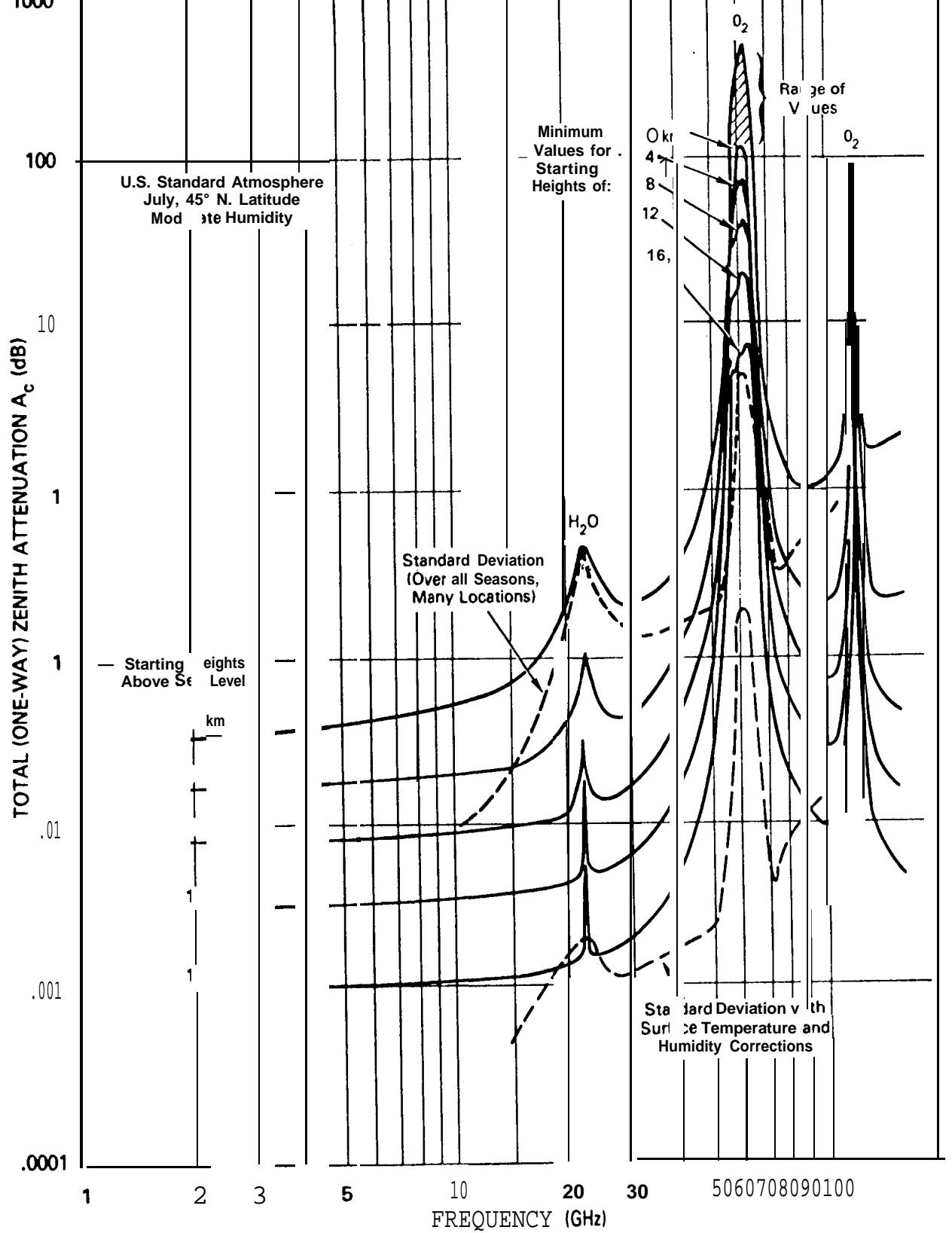


Figure 6.2-1. Total Zenith Attenuation Versus Frequency

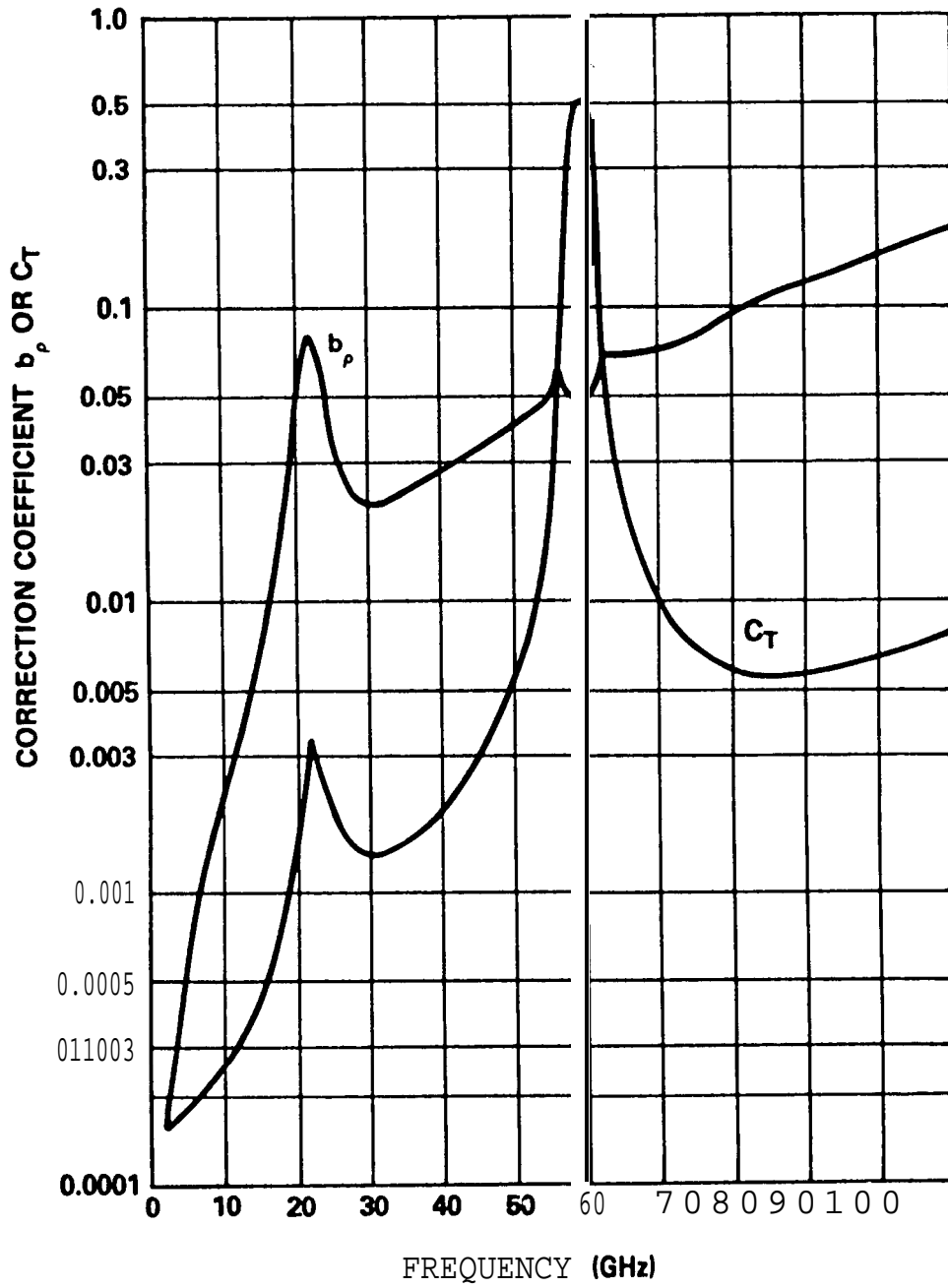


Figure 6.2-2. Water Vapor Density and Temperature Correction Coefficients

Table 6.2-2. Water Vapor Density and Temperature Correction Coefficients

Frequency (GHz)	Water Vapor Density Correction b_p	Temperature Correction C_T
10	2.10×10^{-3}	2.60×10^{-4}
15	6.34×10^{-3}	4.55×10^{-4}
20	3.46×10^{-2}	1.55×10^{-3}
30	2.37×10^{-2}	1.33×10^{-3}
40	2.75×10^{-2}	1097×10^{-3}
80	9.59×10^{-2}	5.86×10^{-3}
90	1.22×10^{-1}	5.74×10^{-3}
100	1.50×10^{-1}	6.30×10^{-3}

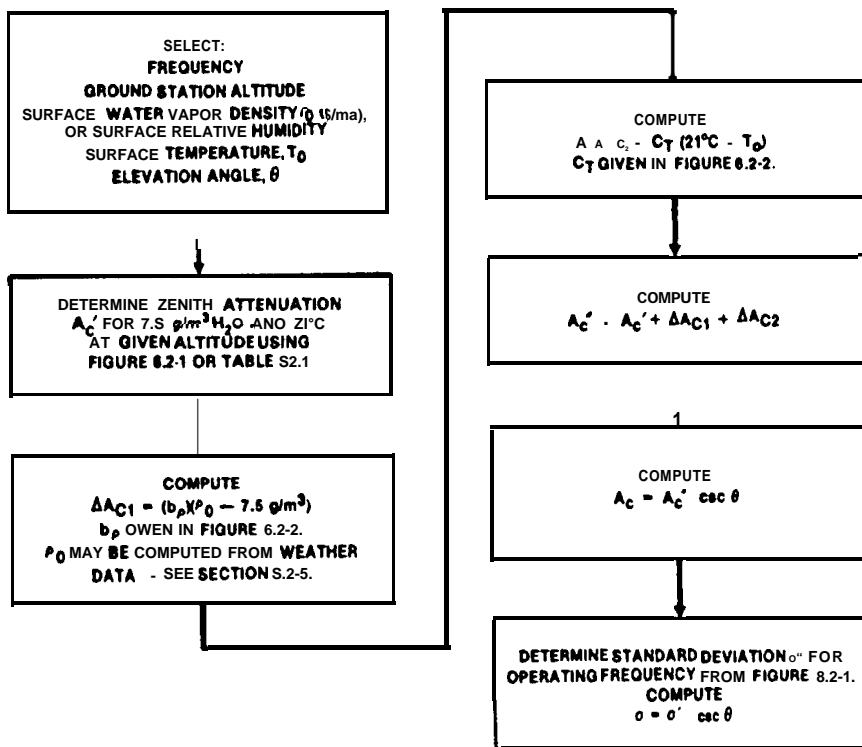


Figure 6.2-3. Technique for Computing Mean Clean Air Attenuation

6.2.2.1.3 Dependence on Surface Temperature. The mean surface temperature T_0 also affects the total attenuation. This relation (Crane and Blood, 1979) is also linear:

$$\Delta A_{c2} = c_T (21^\circ - T_0) \quad (6.2-2)$$

where T_0 is mean local surface temperature in °C.

A_{c2} is an additive correction to the zenith clear air attenuation. Frequency dependent values for c_T are given in Figure 6.2-2 and Table 6.2-2. As with water vapor correction, the accuracy of this factor decreases with altitude.

6.2.2.1.4 Dependence on Elevation Angle. For elevation angles greater than 5 or 6 degrees, the zenith clear air attenuation A_c is multiplied by the cosecant of the elevation angle θ . The total attenuation for arbitrary elevation angle is

$$A_c = A_c' \text{ Csc } \theta \quad (6.2-3)$$

The standard deviation (see Figure 6.2-1) also is multiplied by the $\text{csc } \theta$ for arbitrary elevation angles.

6.2.3 Estimation Procedure For Gaseous Attenuation

The **CCIR** has developed an approximate method to calculate the median gaseous absorption loss expected for a given value of surface water vapor density, (**CCIR-1986a**). The method is applicable up to 350 GHz, except for the high oxygen absorption bands.

Input parameters required for the calculation are:

- f - frequency, in GHz
- θ - path elevation angle, in degrees,
- h_s - height above mean sea level of the earth terminal, in km,
and
- ρ_w - water vapor density at the surface, for the location of
interest, in g/m³.

If ρ_w is not available from local weather services, representative median values can be obtained from CCIR Report 563-3 (CCIR-1986c).

The specific attenuation at the surface for dry air ($P = 1013 \text{ mb}$) is then determined from:

$$\gamma_o = \left[7.19 \times 10^{-3} + \frac{6.09}{f^2 + 0.227} + \frac{4.81}{(f - 57)^2 + 1.50} \right] f^2 \times 10^{-4} \text{ dB/km}$$

for $f < 57 \text{ GHz}$ (6.2-4)

$$\gamma_o = \left[3.79 \times 10^{-7} f + \frac{0.265}{(f - 63)^2 + 1.59} + \frac{0.028}{(f - 118)^2 + 1.47} \right] \times \frac{f^2}{(f^2 + 198)^2 \times 10^{-3}} \text{ dB/km}$$

for $63 < f < 350 \text{ GHz}$

[The application of the above relationships in the high oxygen absorption bands (50-57 GHz and 63-70 GHz) may introduce errors of up to 15%. More exact relationships are given in CCIR Report 719 (CCIR-1986d)].

The specific attenuation for water vapor, γ_w , is found from:

$$\gamma_w = \left[0.067 + \frac{3}{(f - 22.3)^2 + 7.3} + \frac{9}{(f - 183.3)^2 + 6} + \frac{4.3}{(f - 323.8)^2 + 10} \right] f^2 \rho_w \times 10^{-4} \text{ dB/km}$$

for $f < 350 \text{ GHz}$ (6.2-5)

The above expressions are for an assumed surface air temperature of **15°C**. corrections for other temperatures will be described later. Also, the above results are accurate for water vapor densities less than 12 g/m^3 . [For higher water vapor density values, see CCIR Report 719 (CCIR-1986d), and the following.]

An algorithm for the specific attenuation of water vapor which includes a quadratic dependence on water vapor density and allows

values of water vapor densities $>12 \text{ g/m}^3$, has been proposed by Gibbons (1986) and provisionally accepted by the CCIR (1988),

$$\gamma_w = \left[\frac{0.050 + 0.0021\rho_w + \frac{3.6}{(f - 22.2)^2 + 8.5}}{\frac{8.9}{(f - 325.4)^2 + 26.3}} \right] f^2 \rho_w 10^{-4} \text{ dB/km} \quad (6.2-6)$$

for $T = 15^\circ\text{C}$ and $f \leq 350 \text{ GHz}$.

Gibbons finds Eq. (6.2-6) to be valid within about $\pm 15\%$ over the range of ρ_w from 0 to 50 g/m^3 . However, in applying Eq. (6.2-6) with water vapor densities greater than 12 g/m^3 it is important to remember that the water vapor density may not exceed the saturation value ρ_s at the temperature considered. This saturation value may be expressed as (Gibbons, 1986),

$$\rho_s = 17.4 (*)^{6.1} 10^{\left(10 - \frac{29502}{T}\right)} \text{ g/m}^3 \quad (6.2-7)$$

where T is the temperature in $^\circ\text{K}$.

For temperatures in the range -20°C to $+40^\circ\text{C}$ Gibbons proposes a temperature dependence of -1.0% per $^\circ\text{C}$ for dry air in the window regions between absorption lines and -0.6% per $^\circ\text{C}$ for water vapor. The correction factors are therefore

$$\gamma_a = \gamma_a(15^\circ\text{C}) [1 - 0.01(T_0 - 15)] \quad (6.2-8)$$

$$\gamma_w = \gamma_w(15^\circ\text{C}) [1 - 0.006(T_0 - 15)] \quad (6.2-9)$$

where T_0 is the surface temperature in $^\circ\text{C}$.

The equivalent heights for oxygen, h_o , and water vapor, h_w , are determined from:

$$h_o = 6 \text{ km} \quad \text{for } f < 57 \text{ GHz} \quad (6.2-10)$$

$$h_o = 6 + \frac{40}{(f - 118.7)^2 + 1} \text{ km} \quad \text{for } 63 < f < 350 \text{ GHz}$$

$$h_w = \left[2.2 + \frac{3}{(f - 22.3)^2 + 3} + \frac{1}{(f - 183.3)^2 + 1} + \frac{1}{(f - 323.8)^2 + 1} \right] \text{ km} \quad \text{for } f < 350 \text{ GHz} \quad (6.2-11)$$

The total slant path gaseous attenuation through the atmosphere, A_g , is then found.

For $\theta \geq 10^\circ$:

$$A_g = \frac{\gamma_o h_o e^{-\frac{h_s}{h_o}} + \gamma_w h_w}{\sin \theta} \text{ dB} \quad (6.2-12)$$

For $\theta < 10^\circ$:

$$A_g = \frac{\gamma_o h_o}{g(h_o)} + \frac{\gamma_w h_w}{g(h_w)} \text{ dB} \quad (6.2-13)$$

with

$$g(h) = 0.661x + 0.3394x^2 + \frac{h}{1545.5} \quad (6.2-14)$$

$$x = \sqrt{\sin^2 \theta + \frac{h_s}{4250}} \quad (6.2-15)$$

where h is replaced by h_o or h_w as appropriate.

The above procedure does not account for contributions from trace gases. These contributions are negligible except in cases of very low water vapor densities ($\leq 1 \text{ g/m}^3$) at frequencies above about 70 GHz.

6.2.4 Conversion of Relative Humidity to Water Vapor Density

The surface water vapor density ρ_0 (g/m^3) at a given surface temperature T_0 may be found from the ideal gas law

$$\rho_0 = (\text{R.H.}) e_s / R_w (T_0 + 373) \quad (6.2-16)$$

where **R.H.** is the relative humidity, e_s (N/m^2) is the saturated partial pressure of water vapor corresponding to the surface temperature T_0 ($^{\circ}\text{C}$) and $R_w = 461 \text{ joule/kgK} = 0.461 \text{ joule/gK}$. A plot of e_s in various units is given in Figure 6.2-4. For example, with

$$\text{R.H.} = 50\% = 0.5$$

$$T_0 = 20^{\circ}\text{C}$$

$$e_s \approx 2400 \text{ n/m}^2 \text{ at } 20^{\circ}\text{C} \text{ from Figure 6.2-4}$$

then

$$\rho_0 = 8.9 \text{ g/m}^3.$$

The relative humidity corresponding to 7.5 g/m^3 at 20°C (68°F) is $\text{R.H.} = 0.42 = 42\%$.

6.2.5 A Sample Calculation for Gaseous Attenuation

This section presents an example calculation for the total path gaseous attenuation, using the CCIR procedure described in Section 6.2.3.

Assume the following input parameters for a K_a band link:

Frequency, $f = 29.3 \text{ GHz}$

Path Elevation Angle, $\theta = 38^{\circ}$

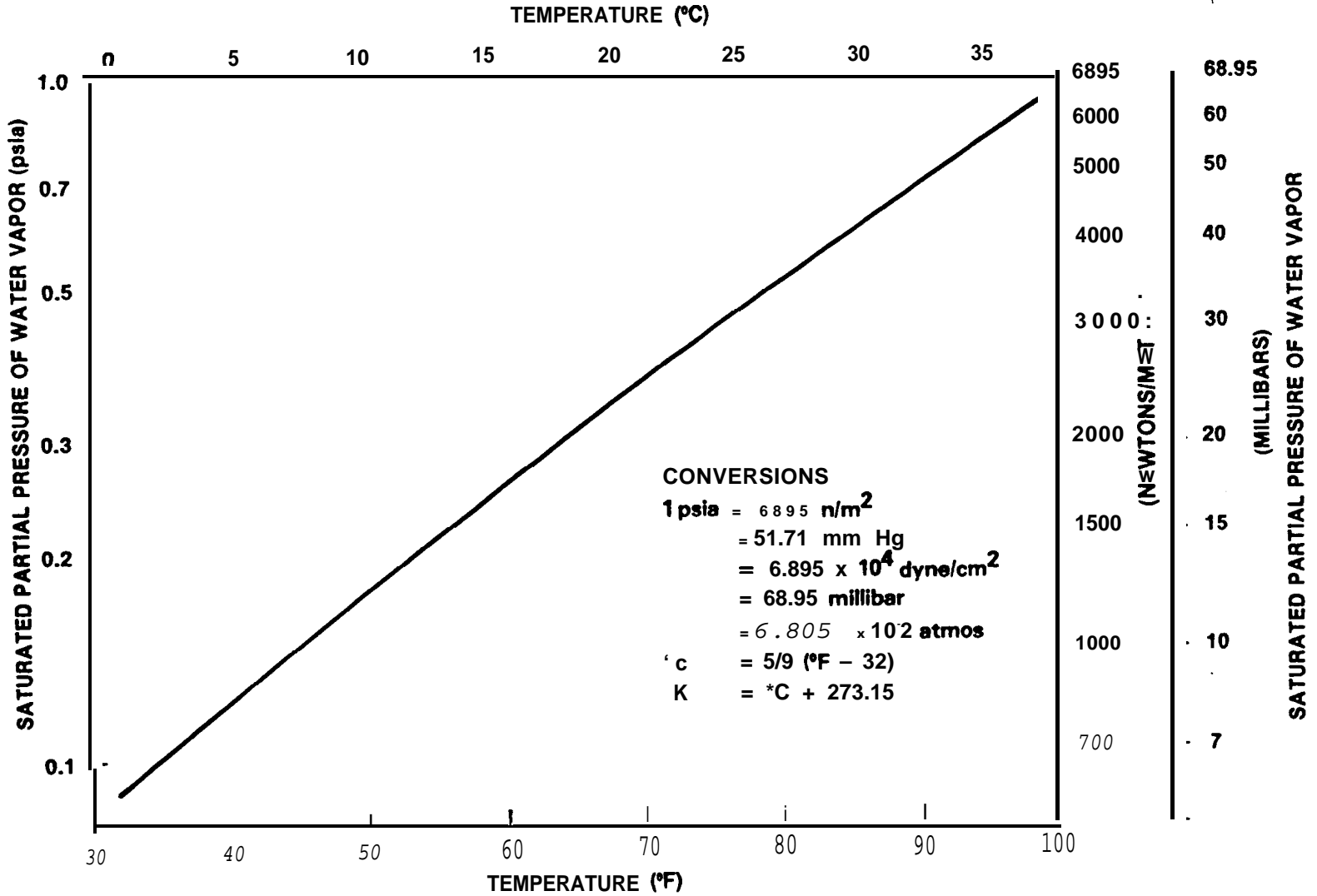


Figure 6.2-4. The Saturated Partial Pressure of Water Vapor Versus Temperature

Height above mean sea level, $h_s = .2$ km

Surface water vapor density, $\rho_w = 7.5$ g/m³

Surface temperature, $T_0 = 20^\circ\text{C}$

Step 1. Calculate the specific attenuation coefficients for oxygen, γ_o , and for water vapor, γ_w , from Equations (6.2-4) and (6.2-6) respectively;

$$\gamma_o = 0.01763 \text{ dB/km} \quad (\text{from } f < 57 \text{ GHz relationship})$$

$$\gamma_w = 0.0777 \text{ dB/km}$$

Step 2. Correct γ_o and γ_w for 20°C , using equations (6.2-8) and (6.2-9) respectively;

$$\gamma_o = 0.01763 [1 - 0.01(20 - 15)] = 0.01675 \text{ dB/Km}$$

$$\gamma_w = 0.0777 [1 - 0.006(20 - 15)] = 0.07537 \text{ dB/Km}$$

Step 3. Calculate the equivalent heights for oxygen, h_o , and for water vapor, h_w , from Equations (6.2-10) and (6.2-11) respectively;

$$h_o = 6 \text{ km}$$

$$h_w = 2.258 \text{ km}$$

Step 4. The total slant path gaseous attenuation is determined from Equation (6.2-8);

$$\begin{aligned} A_g &= [(0.018) (6)e^{-(0.2)/(6)} + (0.078) (2.258)1/\sin (38)] \\ &= 0.1579 + 0.2764 = 0.4343 \text{ dB} \end{aligned}$$

The results show that the contribution from oxygen absorption is 0.1579 dB, and the contribution from water vapor is 0.2764 dB, for a total of 0.4343 dB.

6.3 PREDICTION OF CUMULATIVE STATISTICS FOR RAIN ATTENUATION

6.3.1 General Approaches

6.3.1.1 Introduction to Cumulative Statistics. Cumulative statistics give an estimate of the total **time**, over a long **period**, that rain attenuation or rate can be expected to exceed a given amount. They are normally presented with parameter values (rain rate or attenuation) along the abscissa and the total percentage of time that the parameter value was exceeded (the "exceedance time") along the ordinate. The ordinate normally has a logarithmic scale to most clearly show the exceedance times for large values of the parameter, which are often most important. Usually, the percentage exceedance time is interpreted as a probability and the statistical exceedance curve is taken to be a cumulative probability distribution function. Because of the general periodicity of meteorological phenomena, cumulative statistics covering several full years, or like periods of several successive years, are the most directly useful. (A technique exists, however, for extending statistics to apply to periods greater than those actually covered. This is described in Section 6.3.4.) Statistics covering single years or periods would be expected to exhibit large fluctuations from year to year, because of the great variability of the weather. In most geographic regions, data covering ten years or more is usually required to develop stable and reliable statistics.

Cumulative rain rate or attenuation exceedance statistics alone give no information about the frequency and duration of the periods of exceedance. Rather, only the total time is given. The nature of rain attenuation, however, is such that the exceedance periods are usually on the order of minutes in length. Different phenomena besides rain give rise to attenuation variations occurring on a time scale of seconds. These amplitude **scintillations**, as they are **called**, are not considered in this **section**, but are discussed in Section 6.5.

6.3.1.2 procedures for Calculating Cumulative Rain Attenuation Statistics. The system designer needs reliable cumulative attenuation statistics to realistically trade off link margins, availability siting and other factors. Needless to say, applicable millimeter-wave attenuation measurements spanning many years seldom exist. It is therefore necessary to estimate statistics, using whatever information is available.

An estimate of the rain attenuation cumulative statistics may be determined in several ways. The optimum way depends on the amount of rain and/or attenuation data available, and on the level of sophistication desired. However, it is recommended that the simplest calculations be carried out first to provide an approximation for the statistics and also to act as a check on the results of more sophisticated calculations.

The flow charts in Figures 6.3-1, 6.3-7 and 6.3-13 will assist in applying selected calculation procedures. The steps are numbered sequentially to allow easy reference with the accompanying discussions in Sections 6.3.2, 6.3.3 and 6.3.4. These are the procedures given:

- Analytical Estimates using the Global Model (Section 6.3.2, Figure 6.3-1). Requires only Earth station location, elevation **angle**, and frequency.
- . Analytical Estimates using the **CCIR** Model (Section 6.3.2, Figure 6.3-7). Requires only Earth station location, elevation angle, and frequency.
- Estimates Given Rain Rate Statistics (Section 6.3.3, Figure 6.3-1). Requires cumulative rain rate exceedance statistics for vicinity of the Earth station location, elevation **angle**, and frequency.
- . Estimates Given Rain Rate and Attenuation Statistics (Section 6.3.4, Figure 6.3-13). Requires attenuation statistics which

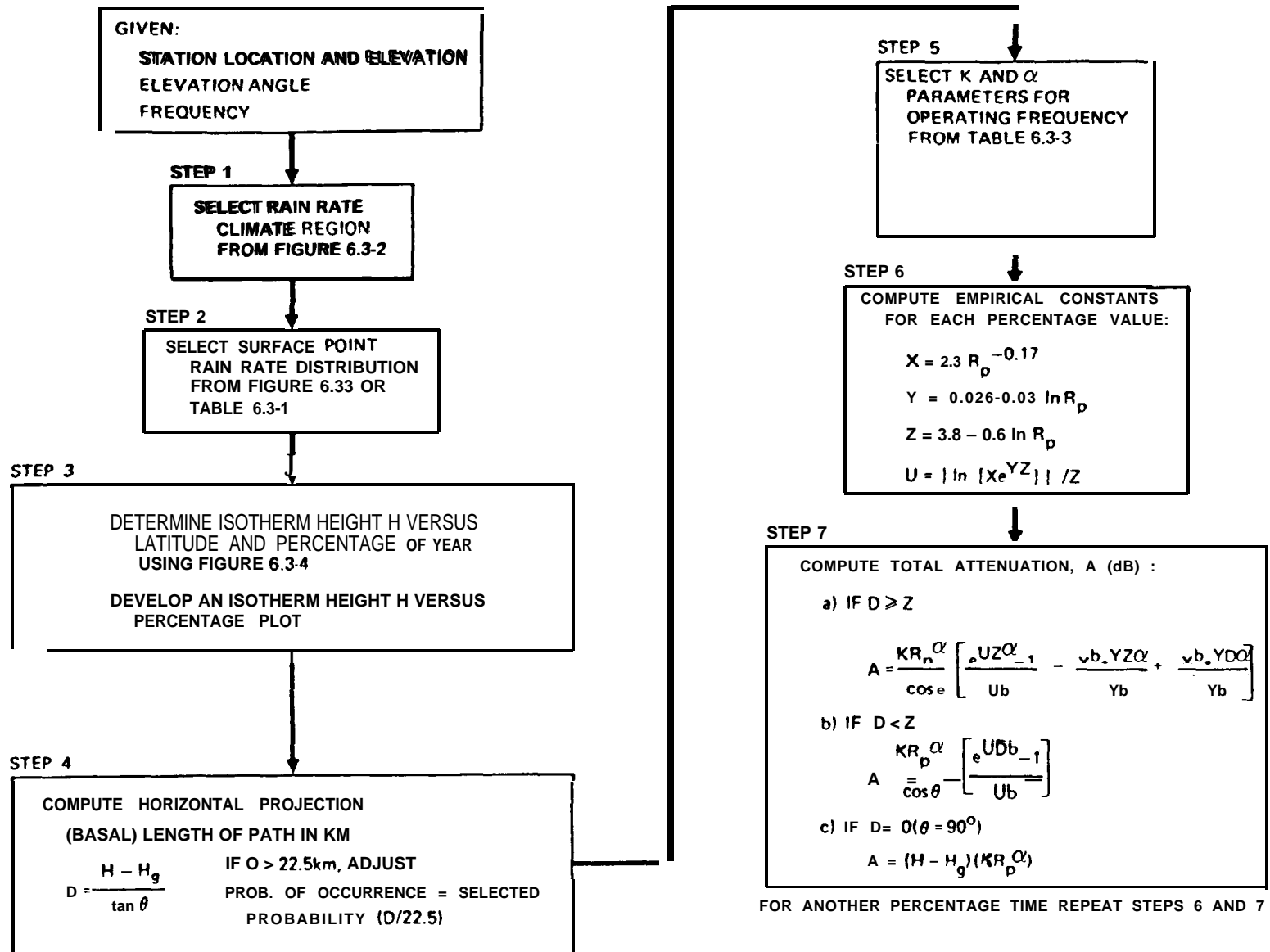


Figure 6.3-1. Analytic Estimate procedure for Cumulative Rain Rate and Attenuation Statistics Using the **Global Model**

may be for frequency and elevation angle different from those needed.

6.3.1.3 Other Considerations. Generally the yearly cumulative statistics are desired. The worst-month or 30-day statistics are sometimes also needed, but are not derivable from the data presented here. Worst 30-day statistics are discussed in Section 6.3.7.

The attenuation events due to liquid rain only are considered here. Liquid rain is the dominate attenuation-producing precipitation because its specific attenuation is considerably higher than snow, ice, fog, etc. The contribution of these other hydrometers is estimated in later sections.

The cumulative statistics are appropriate for earth-space paths for geostationary or near-geostationary satellites with relatively stable orbital positions. The modifications required to develop statistics for low-orbiting satellites is unclear because of the possibly nonuniform spatial distribution of rain events arising from local topography (lakes, mountains, etc.). However, if one assumes these effects **are** of second-order, low orbiting satellites may simply be considered to have time-dependent elevation angles.

6.3.2 Analytic Estimates of Rain Attenuation from Location and Link Parameters

The following analytic estimation techniques provide reasonably precise estimates of rain attenuation statistics. The first technique is based on the modified Global Prediction Model (Crane and Blood- 1979, Crane- 1980, 1980a). Only parts of the model relevant to the contiguous US and Canada, and elevation angles greater than 10° , are presented here. The second technique uses the CCIR Model and is perhaps the simplest prediction approach. Example applications of both techniques are given. The analytical developments for the global model and the CCIR model are presented in Sections 3.4 and 3.6, respectively.

The models require the following inputs:

- a) Ground station latitude, longitude and height above mean sea level
- b) The earth-space path elevation angle
- c) The operating frequency

6.3.2.1 Global Model Rain Attenuation Prediction Technique. Figure 6.3-1 gives the step-by-step procedure for applying the Global Model. The steps are described in detail below.

Step 1 - At the Earth terminal's geographic latitude and longitude, obtain the appropriate climate region using Figure 6.3-2. For locations outside the Continental U.S. and Canada, see Section 3.4.1. If long term rain rate statistics are available for the location of the ground **terminal**, they **should** be used instead of the model distribution functions and the procedure of Section 6.3.3 should be employed.

Step 2 - Select probabilities of exceedance (P) covering the range of interest (**e.g., .01, .1 or 1%**). Obtain the terminal point rain rate R (mm/hour) corresponding to the selected values of P using Figure 6.3.3, Table 6.3-1 or long term measured values if available.

Step 3 - For an Earth-to-space link through the entire atmosphere, obtain the rain layer height from the height of the 0° isotherm (melting layer) H₀ at the path latitude (Figure 6.3-4). The heights will vary correspondingly with the probabilities of exceedance, P. To interpolate for values of P not given, plot H₀ (P) vs Log P and sketch a best-fit curve.

Step 4 - Obtain the horizontal path projection D of the oblique path through the rain volume:

$$D = \frac{H_0 - H_g}{\tan \theta} ; \theta \geq 10^\circ \quad (6.3-1)$$

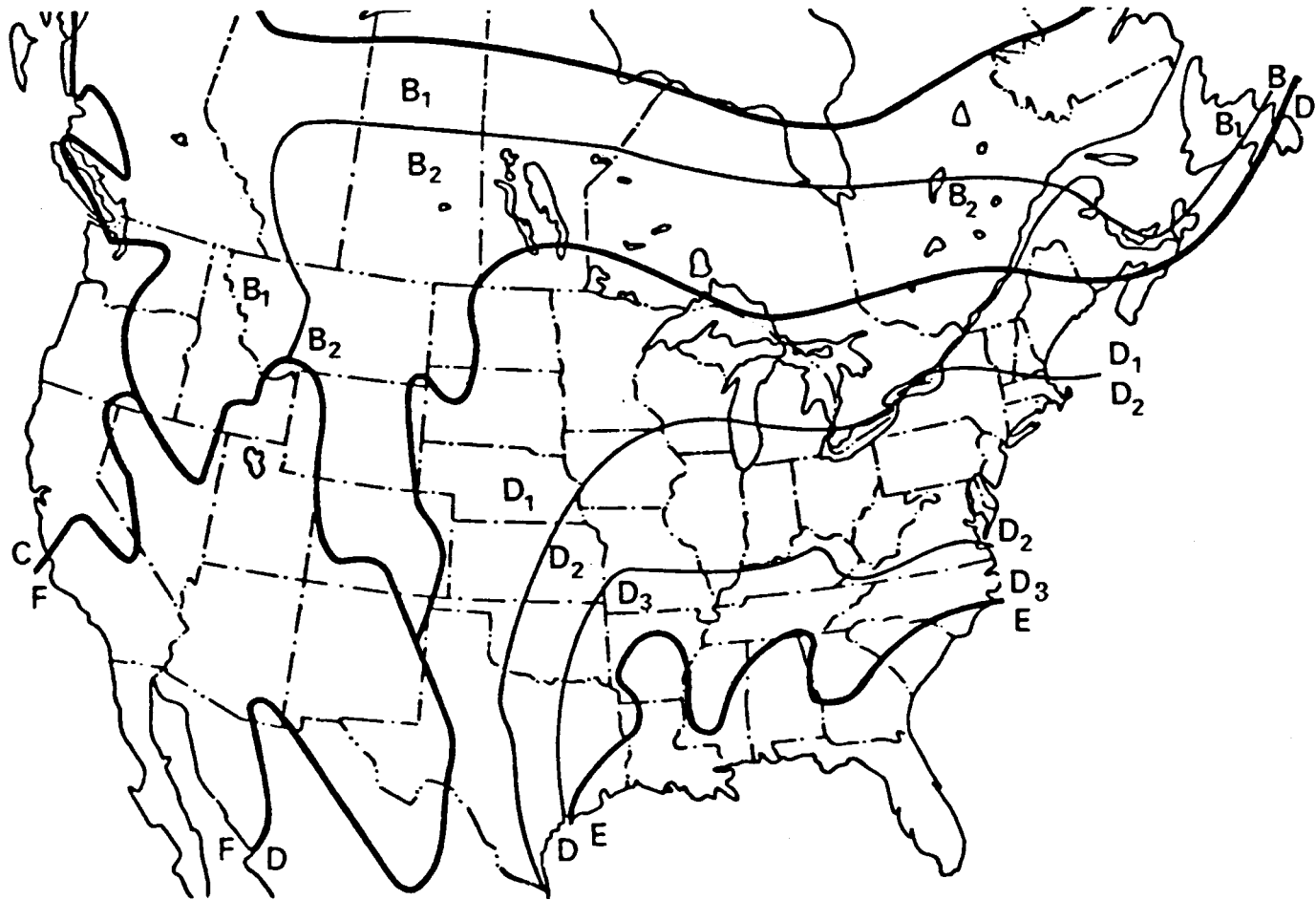


Figure 6.3-2. Rain Rate Climate Regions for the Continental U.S. and Southern Canada

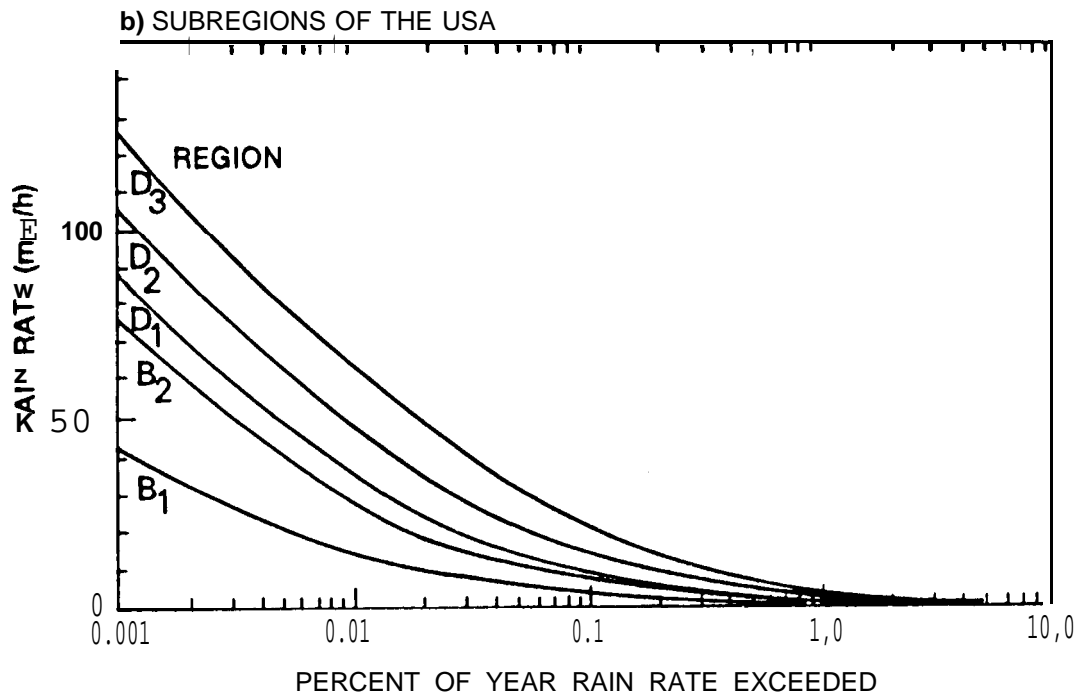
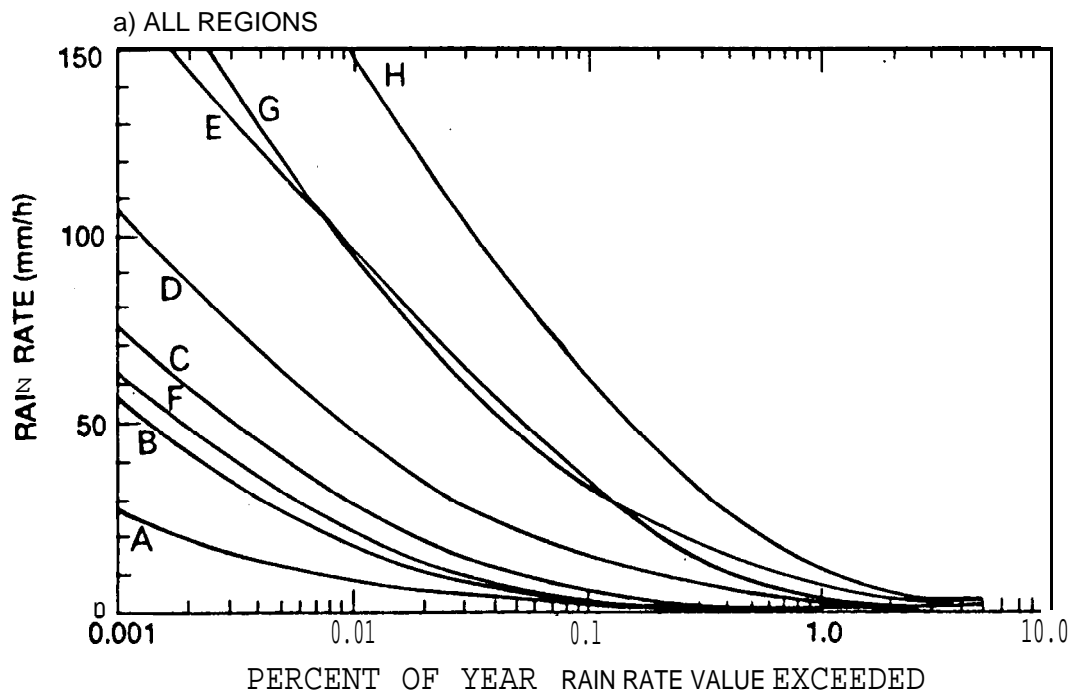


Figure 6.3-3. Point Rain Rate Distributions as a Function of Percent of Year Exceeded

Table 6.3-1. Point Rain Rate Distribution Values (mm/hr) Versus Percent of Year Rain Rate is Exceeded

Percent of Year	RAIN CLIMATE REGION												Minutes per Year	Hours per Year
	A	1	B	2	C	1	D=D ₂	3	E	F	G	H		
0.001	28.5	45	57.5	70	78	90	108	126	165	66	185	253	5.26	0.09
0.002	21	34	44	54	62	72	89	106	144	51	157	220.5	10.5	0.18
0.005	13.5	22	28.5	35	41	50	64.5	80.5	118	34	20.5	178	26.3	0.44
0.01	10.0	15.5	19.5	23.5	28	35.5	49	63	98	23	94	147	52.6	0.88
0.02	7.0	11.0	13.5	16	18	24	35	48	78	15	72	119	105	1.75
0.05	4.0	6.4	8.0	9.5	11	14.5	22	32	52	8.3	47	86.5	263	4.38
0.1	2.5	4.2	5.2	6.1	7.2	9.8	14.5	22	35	5.2	32	64	526	8.77
0.2	1.5	2.8	3.4	4.0	4.8	6.4	9.5	14.5	21	3.1	21.8	43.5	1052	17.5
0.5	0.7	1.5	1.9	2.3	2.7	3.6	5.2	7.8	10.6	1.4	12.2	22.5	2630	43.8
1.0	0.4	1.0	1.3	1.5	1.8	2.2	3.0	4.7	6.0	0.7	8.0	12.0	5260	87.7
2.0	0.1	0.5	0.7	0.8	1.1	1.2	1.5	1.9	2.9	0.2	5.0	5.2	10520	175
5.0	0.0	0.2	0.3	0.3	0.5	0.0	0.0	0.0	0.5	0.0	1.8	1.2	26298	438

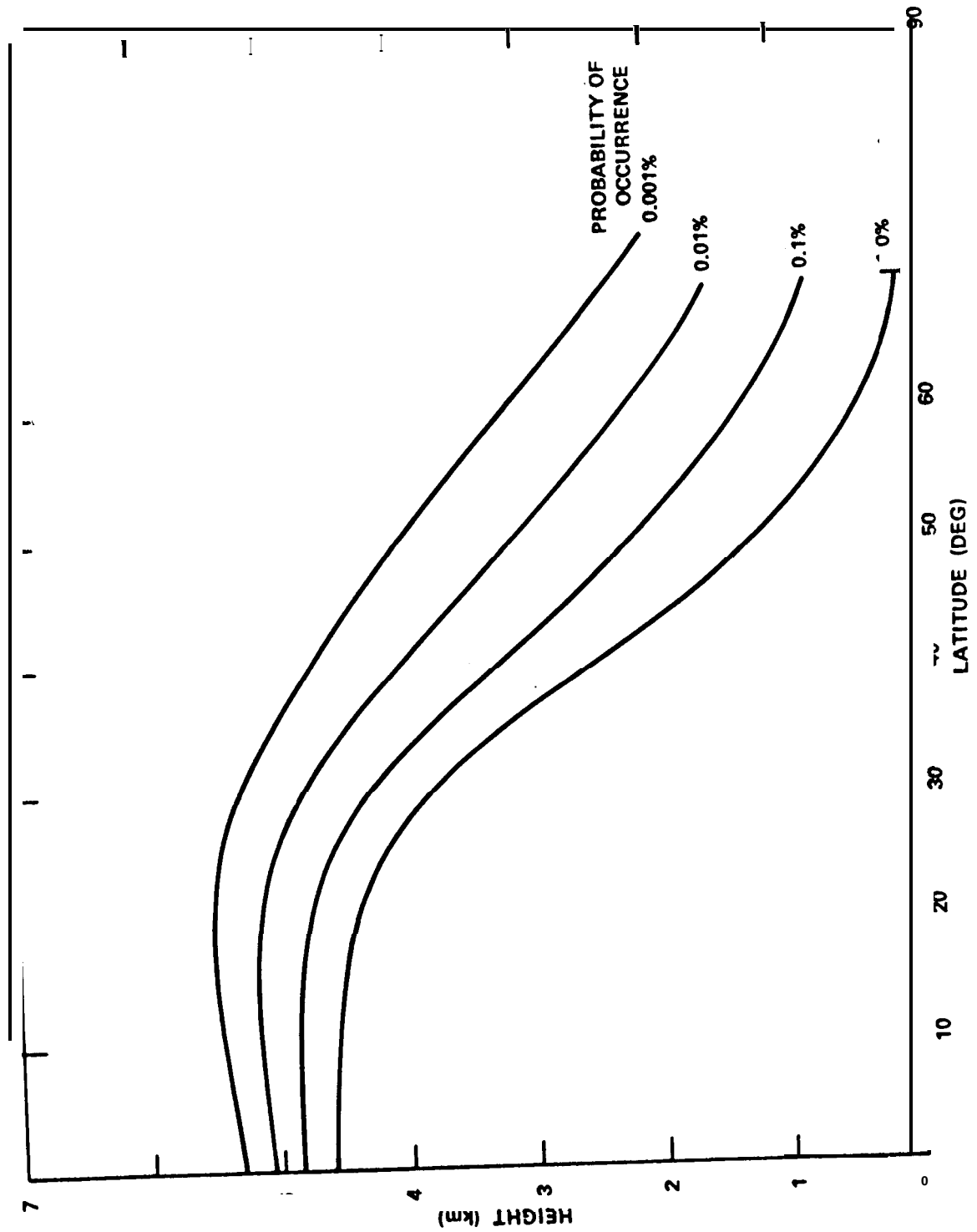


Figure 6.3-4. Latitude Dependence of the Rain Layer 0°C Isotherm Height as a Function of Probability of Occurrence

$H_0 = H_0(P) =$ height (km) of isotherm for probability P

$H_g =$ height of ground terminal (km)

$\theta =$ path elevation angle

Test $D \leq 22.5$ km; if true, proceed to the next step. If $D \geq 22.5$ km, the path is assumed to have the same attenuation value as for a 22.5 km path but the probability of exceedance is adjusted by the ratio of 22.5 km to the' path length:

$$\text{New probability of exceedance, } P' = P \left(\frac{22.5 \text{ km}}{D} \right) \quad (6.3-2)$$

where $D =$ path length projected on surface. This correction accounts for the effects of traversing multiple rain cells at low elevation angles.

Step 5 - **Obtain** the specific attenuation coefficients, k and α , at the frequency and polarization angle of **interest**, from **Table 6.3-3**. For frequencies not in the table, use logarithmic interpolation for K and linear interpolation for α . The subscript H columns are for horizontal linear polarization and the subscript V columns are for vertical linear polarization. [For polarization tilt angles other than horizontal or vertical, use the relationships on Figure **6.3-6**, Step **4**, to obtain K and α].

Step 6 - **Using** the R_p values corresponding to each exceedance probability of **interest**, calculate the empirical constants X , Y , Z and U using

$$x = 2.3 R_p^{-0.17} \quad (6.3-4)$$

$$Y = 0.026 - 0.03 \ln R_p \quad (6.3-5)$$

$$z = 3.8 - 0.7 \ln R_p \quad (6.3-6)$$

$$u = [\ln(Xe^{YZ})]/z \quad (6.3-7)$$

Step 7 - If $Z \leq D$, compute the total attenuation due to rain exceeded for P % of the time using

$$A = \frac{k R_p^\alpha}{\cos \theta} \left[\frac{e^{UZ\alpha} - 1}{U\alpha} - \frac{X^\alpha e^{YZ\alpha}}{Y\alpha} + \frac{X^\alpha e^{YD\alpha}}{Y\alpha} \right]; \theta \geq 10^\circ \quad (6.3-8)$$

where A = Total path attenuation due to rain (dB)

k, a = parameters relating the specific attenuation to rain rate (from Step 5).

R_p = point rain rate

e = elevation angle of path

D = horizontal path projection length (from step 4)

If $D < Z$,

$$A = \frac{k R_p^\alpha}{\cos \theta} \left[\frac{e^{UD\alpha} - 1}{U\alpha} \right] \quad (6.3-9)$$

If $D = 0, \theta = 90^\circ$,

$$A = (H - H_g) (K R_p^\alpha) \quad (6.3-10)$$

This procedure results in an analytical estimate for the attenuation, A, exceeded for P percent of an average year. The use of a programmable calculator or computer for performing these calculations is highly recommended.

6.3.2.2" A Sample Calculation for the Global Model The following information is given for the **Rosman**, NC Earth Station operating with the **ATS-6** satellite.

Earth station latitude :	35°N
Earth station longitude:	277°E.
Earth station elevation:	0.9 km

Antenna elevation Angle: 47°

Operating frequency: 20 GHz

We wish to find an analytic estimate for the cumulative attenuation statistics using the procedure of Figure 6.3-1.

1. Select rain rate climate region for Rosman, NC:
From Figure 6.3-2, Rosman is located in region **D₃**.
- 2* Select surface point rain rate distribution:
From Table 6.3-1, region **D₃** has the following distribution:

<u>R</u>	<u>R_p</u>
0.01	63
0.02	48
0.05	32
0.10	22
0.20	14.5
0.50	7.8
1.0	4.7

3. Determine isotherm **height**:

From Figure 6.3-4, the following isotherm height estimates apply at 35° latitude.

<u>R</u>	<u>H</u>
0.01	4.4 km
0.1	3.75
1.0	3.2

By plotting these, the following additional points may be interpolated

0.02	4.2
0.05	3.95
0.2	3.55
0.5	303

4. Compute D:

Using $\theta = 47^\circ$ and $H_g = 0.9$ km, we obtain

<u>x</u>	<u>D</u>
0.01	3.25 km
0.02	3.1
0.05	2.85
0.1	2.65
0.2	2.45
0.5	2.25
1.0	2.15

5. Select K and a:

The specific attenuation coefficients, K and a are selected from Table 6.3-3 at 20 GHz, horizontal polarization.

$$K = 0.0751$$

$$a = 1.10$$

6. Compute empirical constants:

For **example**,

<u>x</u>	<u>X</u>	<u>Y</u>	<u>Z</u>	<u>U</u>
0.1	1.36	-0.067	1.95	0.091
0.2	1.46	-00054	2.20	0.118

0.5 1.62 -0.036 2.57 0.153

7. Compute attenuation, A:

We note from step 6 that at 0.2%, D is greater than **Z**. This also holds for percentages less than 0.1%. Thus the formula of Step 7 (a) is used to find the attenuation for $\% \leq 0.1$.

For $\% \geq 0.5$, D is less than **Z**, so the formula of Step 7 (b) applies. The attenuation values found in this way are plotted versus percentage **exceedance** in Figure 6.3-5. The figure includes statistics derived from 20 GHz attenuation measurements made at Rosman with the **ATS-6** over a 6-month period.

6.3.2.3 CCIR Model Rain Attenuation Prediction Technique

This section presents the step by step procedure for application of the **CCIR** rain attenuation prediction model, described in detail in Section 3.6. The procedure is outlined in Figure 6.3-6.

Step 1 Obtain the rain rate, **R_{0.01}**, exceeded for 0.01% of an average year for the ground terminal location of interest. If this information is not available from local data sources, an estimate can be obtained by selecting the climate zone of the ground terminal location from Figure 6.3-7, and the corresponding rain rate value for that climate zone from Table 6.3-2. (For locations not found on Figure 6.3-7, see Figures 3.6-1 and 3.6-2).

[Important Note: The **CCIR** rain climate zones are **not** the same as the climate regions of the Global Model described earlier.]

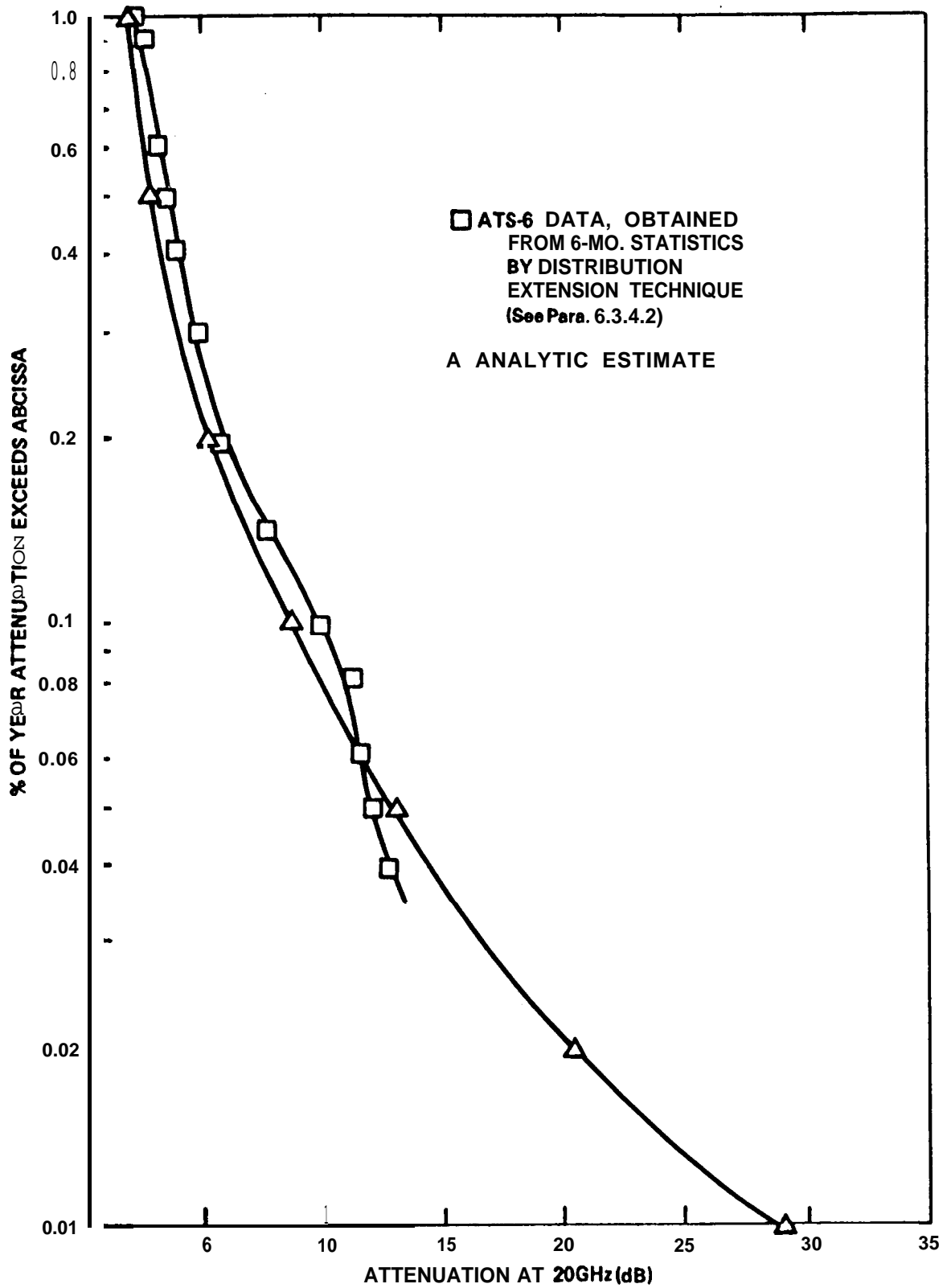


Figure 6.3-5. Analytic Attenuation Estimate and Actual Measurements

Table 6.3-2. Rain Rates Exceeded for 0.01% of the Time

Climate	A	B	C	D	E	F	G	H	J	K	L	M	N	P
Rate	8	12	15	19	22	28	30	32	35	42	60	63	95	145

Step 2 Determine the effective rain height, h_r , from:

$$\begin{aligned}
 h_r &= 4.0 \\
 &= 4.0 - 0.075 (\phi - 36) \quad \phi^0 < \phi < 36^\circ \\
 &\quad \phi \geq 36^\circ
 \end{aligned}
 \tag{6.3-11}$$

where ϕ is the latitude of the ground station, in degrees N or S.

Step 3 Calculate the slant path length, L_s , horizontal projection, L_G , and reduction factor, r_p , from:

For $\Theta \geq 5^\circ$,

$$L_s = (h_r - h_0) / \sin(\Theta) \tag{6.3-12}$$

$$L_G = L_s \cos(\Theta) \tag{6.3-13}$$

$$r_p = \frac{1}{1 + 0.045 L_G} \tag{6.3-14}$$

where Θ is the elevation angle to the satellite, in degrees, and h_0 is the height above mean sea level of the ground terminal location, in km. (For elevation angles less than 5° , see Section 3.6).

Step 4 Obtain the specific attenuation coefficients, K and a , at the frequency and polarization angle of interest from Table 6.3-3. For frequencies not on the table, use logarithmic interpolation for K and linear interpolation for a . For polarization tilt angles other than linear horizontal or vertical, use the relationships on Figure 6.3-6, Step 4, to obtain K and a .

Step 5 Calculate the attenuation exceeded for 0.01% of an average year from:

$$A_{0.01} = K R_{0.01}^a L_s r_p \tag{6.3-15}$$

Step 6 Calculate the attenuation exceeded for other percentage values of an average year from:

$$A_p = 0012 A_{0.01} p^{-(0.546 + 0.043 \log p)} \quad (6.3-16)$$

This relationship is valid for annual percentages from 0.001% to 1.0%.

6.3.2.4 Sample Calculation for the CCIR Model

In this section the CCIR model is applied to a specific ground terminal case. Consider a terminal located at Greenbelt, MD., at a latitude of 38°N, and elevation above sea level of 0.2 km. The characteristics of the link are as follows:

Frequency: 11.7 GHz

Elevation Angle: 29°

Polarization: Circular

Step 1 Figure 6.3-7 indicates that the terminal is in climate zone K, with a corresponding $R_{0.01}$ of 42 mm/h (Table 6.3-2).

Step 2 The effective rain height, from Eq (6.3-11), is

$$h_r = 4.0 - 0.075(38 - 36) = 3.85$$

Step 3 The slant path length, horizontal projection, and reduction factor are determined from Eq.'s (6.3-12, -13, -14) respectively;

$$L_s = (3.85 - 0.2) / \sin(29^\circ) = 7.53$$

$$L_G = (7.53) \cos(29^\circ) = 6.58$$

$$r_p = 1 / [1 + (0.045)(6.58)] = 0.771$$

Step 4 The specific attenuation coefficients are determined by interpolation from Table 6.3-3, with a **polarizaiton** tilt angle of 45° (circular polarization);

$$K = 0.0163, a = 1.2175$$

Step 5 The attenuation exceeded for 0.01% of an average year, from Eq. (6.3-15), is;

$$\begin{aligned} A_{0.01} &= (0.0163) (42)^{1.2175} (7.53) (0.771) \\ &= 8.96 \text{ dB} \end{aligned}$$

Step 6 The attenuation exceeded for other percentages is then determined from Eq. (3.6-16);

<u>%</u>	<u>Attenuation (dB)</u>
1.0	1.08
0.5	1.56
0.3	2.02
001	3.42
0.05	4.67
0.03	5.80
0.01	8.96
0.005	11.48
0.003	13.65
0.001	19.16

Figure 6.3-8 shows a plot of the resulting attenuation prediction distribution, compared with three years of measured distributions obtained with the CTS satellite (Ippolito 1979). The **CCIR** prediction is seen to over-predict slightly for higher percentage values, and to vastly under-predict for percentages below about 0.01%

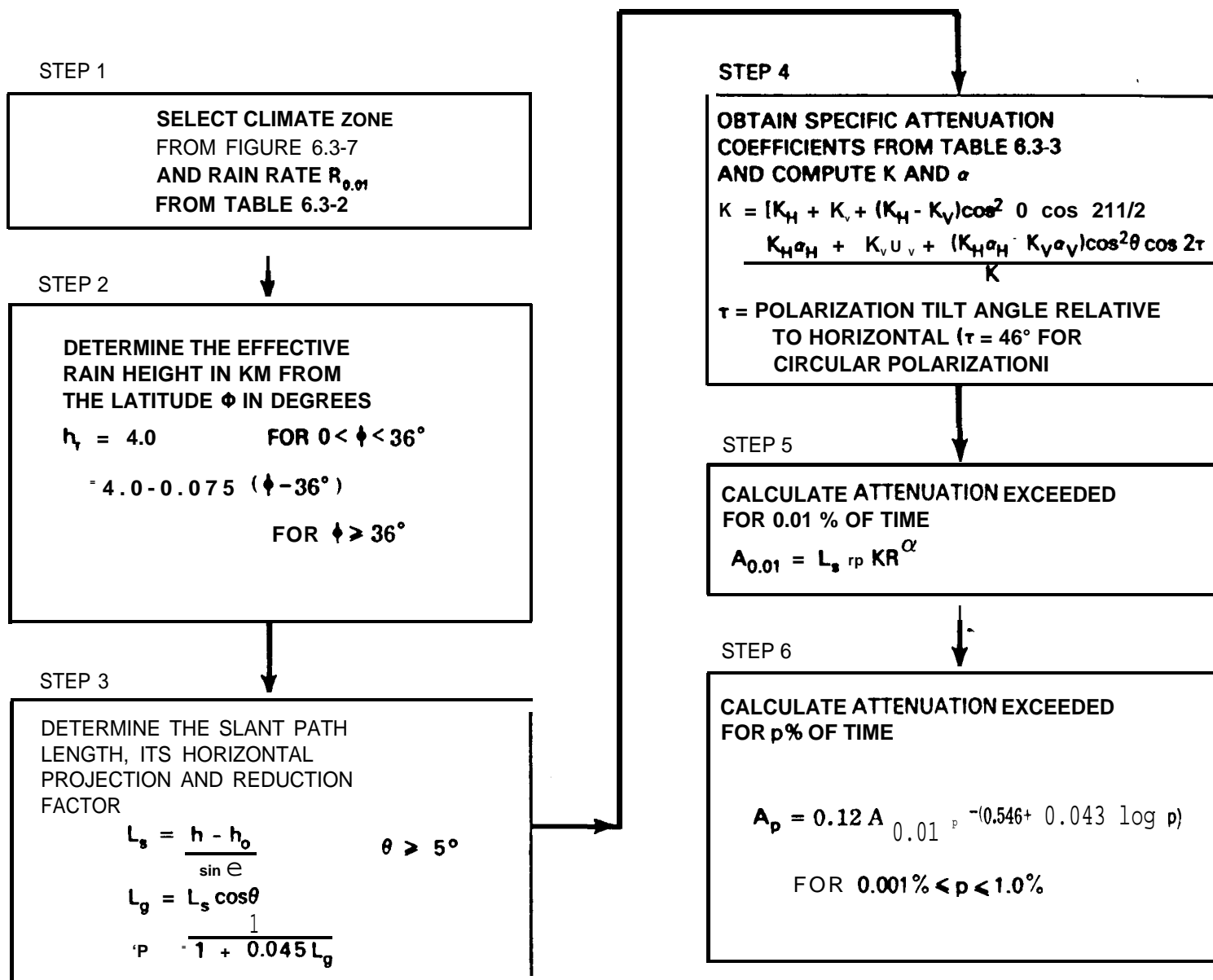


Figure 6.3-6. Analytical Estimate Procedure for Cumulative Rain Rate and Attenuation Statistics Using the CCIR Model

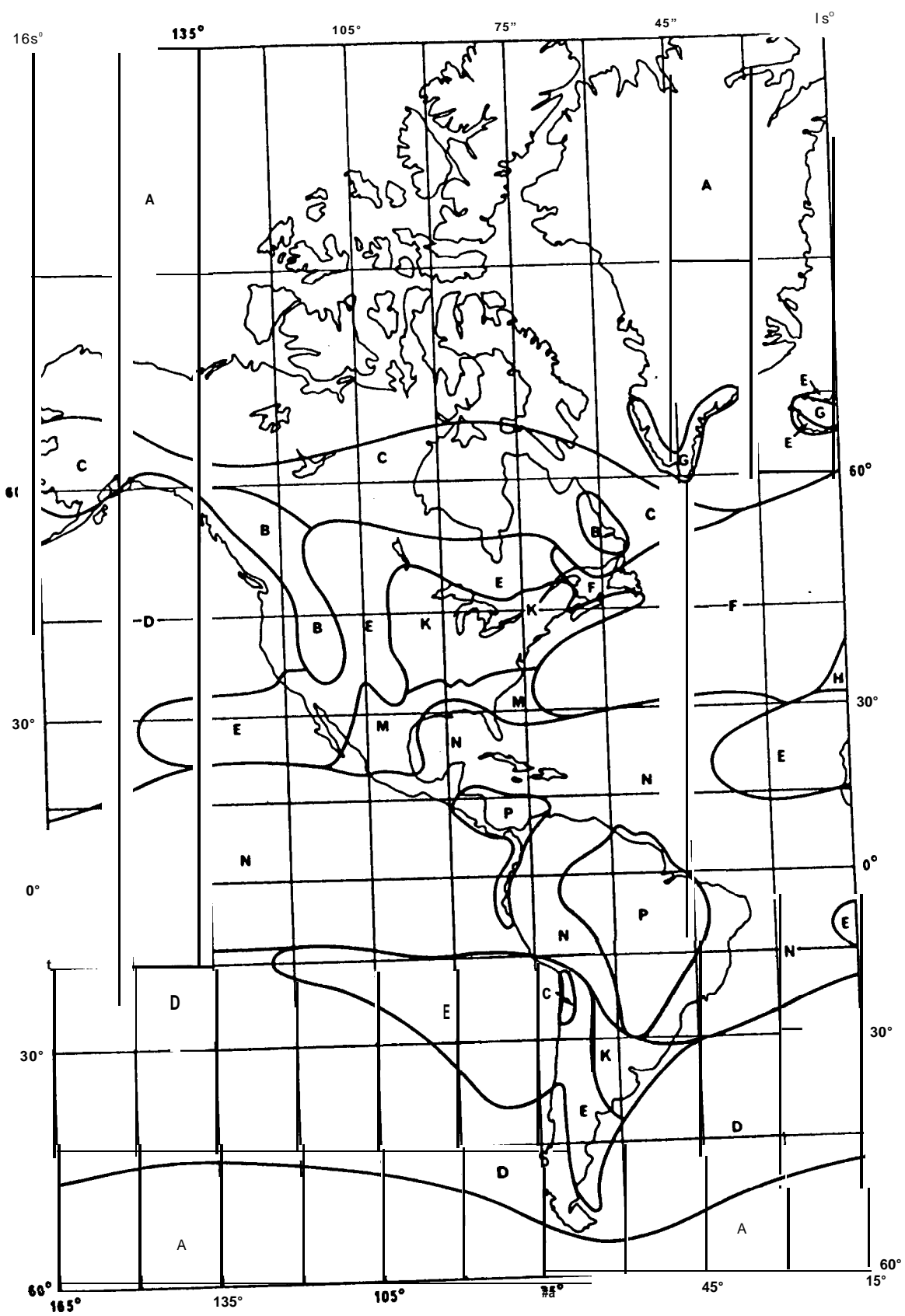


Figure 6.3-7. CCIR Rain Climate Zones for ITU Region 2

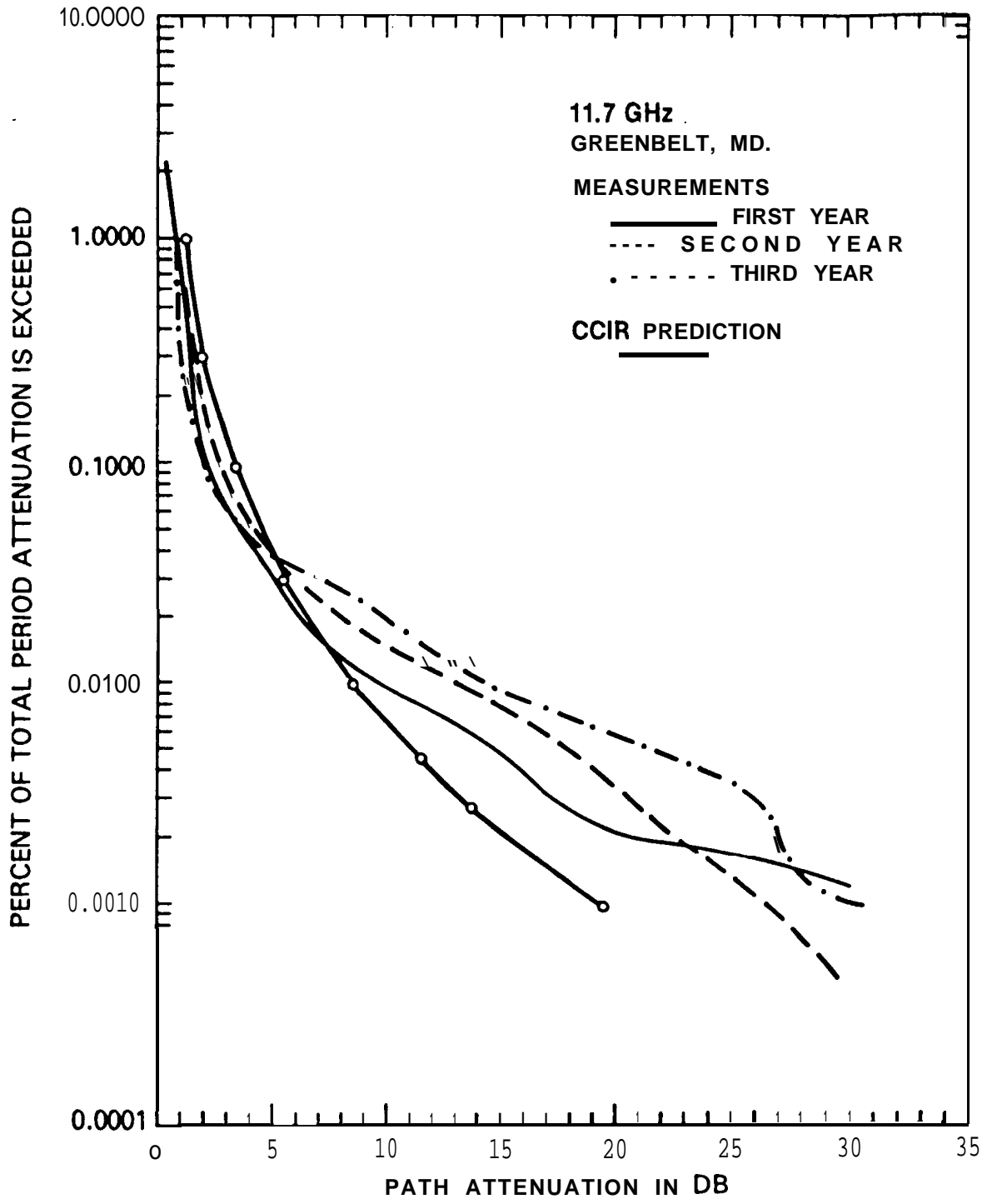


Figure 6.3-8. Comparison of **CCIR** Prediction with Measured Data, Greenbelt, MD. 11.7 GHz

Table 6.3-3. Regression Coefficients for Estimating Specific Attenuation in **Step 4** of Figure 6.3-6

Frequency (GHz)	'H	'V	α_H	α_V
1	0.0000387	0.0000352	0.912	0.880
2	0.000154	0.000138	0.963	0.923
4	0.000650	0.000591	1.12	1.07
6	0.00175	0.00155	1.31	1.27
8	0.00454	0.00395	1.33	1.31
10	0.0101	0.00887	1.28	1.26
12	0.0188	0.0168	1.22	1.20
15	0.0367	0.0347	1.15	1.13
20	0.0751	0.0691	1.10	1.07
25	0.124	0.113	1.06	1.03
30	0.187	0.167	1.02	1.00
35	0.263	0.233	0.979	0.963
40	0.350	0.310	0.939	0.929
45	0.442	0.393	0.903	0.897
50	0.536	0.479	0.873	0.868
60	0.707	0.642	0.826	0.824
70	0.851	0.784	0.793	0.793
80	0.975	0.906	0.769	0.769
90	1.06	0.999	0.753	0.754
100	1.12	1.06	0.743	0.744
120	1.18	1.13	0.731	0.732
150	1.31	1.27	0.710	0.711
200	1.45	1.42	0.689	0.690
300	1.36	1.35	0.688	0.689
400	1.32	1.31	0.683	0.684

* Values for k and a at other frequencies can be obtained by interpolation using a logarithmic scale for k and frequency and a linear scale for a

6.3.3 Estimates of Attenuation Given Rain Rate Statistics

6.3.3.1 Discussion and Procedures. If the rainfall statistics can be reconstructed from Weather Service data or actual site measurements exist for a period of at least 10 years near the ground station **site**, these may be utilized to provide ' R_p versus percentage exceedance. The temporal resolution required of these measurements is dependent on the smallest percentage resolution required. For example, if 0.001% of a year (5.3 minutes) statistics are desired, it is recommended that the rain rate be resolved to increments of no more than 1-minute to provide sufficient accuracy. This can be done utilizing techniques described in Chapter 2 of this handbook, but 5-minute data is more easily obtained.

The cumulative statistics measured near the ground station site replaces Steps 1 and 2 of Figure 6.3-1. The attenuation statistics are generated using the procedures in Steps 3 through 7 of Figure 6.3-1.

6.3.3.2 Example. **Again** we take the case of the 20 GHz ATS-6 link to Rosman, NC. We have cumulative **rain** rate statistics for Rosman for a six-month period as shown in Figure 6.3-9. (Data spanning such a short period should not be used to estimate long-term statistics. The use here is for demonstration purposes only.) We first select values of rain rate R corresponding to several values of percentage exceedance. :

<u>%</u>	<u>R_p</u>
0.01	66
0.02	55
0.05	34
0.10	16.5
0.20	10.5
0.50	4.5
1.0	2.3

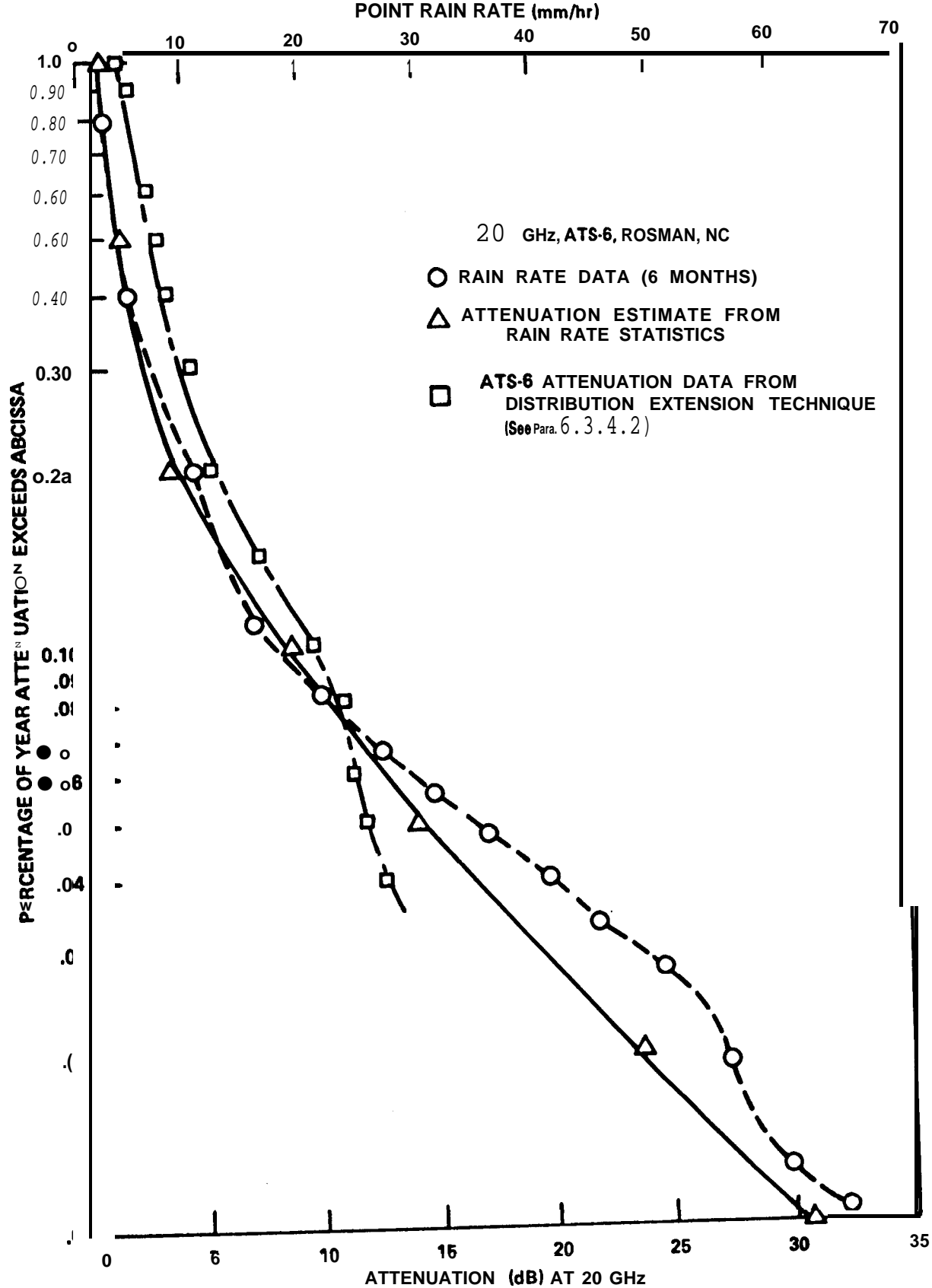


Figure 6.3-9. Attenuation Statistics Estimate Based on Measured Rainfall Statistics

We now proceed exactly as in the Global Model application example (Section 6.3.2.2), using these values of R_p instead of those in Table 6.3-1 or Figure 6.3-3.

The results of these calculations are shown in Figure 6.3-9, along with the measured attenuation statistics. This data is presented to demonstrate the technique. More accurate data, covering a longer **period**, is presented in Chapter 5.

6.3.4 Attenuation Estimates Given Limited Rain Rate and Attenuation Statistics

6.3.4.1 Discussion and Procedures. The system designer will virtually never find attenuation statistics spanning a number of years for his desired location, operating frequency and elevation angle. But by applying distribution extension and scaling procedures to the limited statistics available, the designer **may** make useful estimates of the statistics for the situation at hand.

Distribution extension allows one to take concurrent rain rate and attenuation measurements intermittently over a limited period of time, then convert the data into cumulative attenuation statistics covering the entire year. The conversion requires stable cumulative rain rate statistics for the site or a nearby weather **station**, and measurements taken over a statistically significant fraction of the year. Distribution extension is required in practice because it is often costly to make continuous attenuation measurements over extended periods. Rather, data are taken only during rainy periods.

Scaling is required to account for differences between the frequency and elevation angle applying to the available statistics, and those applying to the actual system under consideration. This scaling is based on empirical formulas **which**, to the first order approximation depend only on the frequencies or the elevation angle and apply equally to all attenuation values. To a better approximation, however, the rain rate corresponding to the attenuation and other factors must be considered as well.

Figure 6.3-10 shows a generalized procedure for applying the distribution extension and scaling techniques described in this section.

6.3.4.2 Attenuation Distribution Extension. The technique is illustrated in Figure 6.3-11. The upper two curves represent cumulative rain rate and attenuation statistics derived from measurements taken over some limited period of time. The measurement time may consist for example, of only the rainy periods from April through September. The **exceedance** curves are plotted as functions of the percentage of the total measurement time. The lower solid curve represents the cumulative rain rate statistics, measured over an extended period at the same location as the attenuation measurements, or derived from multi-year rainfall records from a nearby weather station.

A curve approximating the long-term cumulative attenuation distribution (the bottom curve in Figure 6.3-11) is derived from the three upper curves by the following graphical procedure:

- 10 Select a percent exceedance value, **E_1** , and draw a horizontal line at that value intersecting the limited-time rain rate and attenuation distribution curves at points **a** and **b**, respectively.
2. At the rain rate value **R** corresponding to **E_1** , project a line down to intersect (at point **c**) the long-term rain rate curve at the **exceedance** value **E_2** .
3. At the attenuation value **A** corresponding to **E_1** , project a line down to the exceedance value **E_2** . This (point **d**) is a point on the long-term attenuation curve.

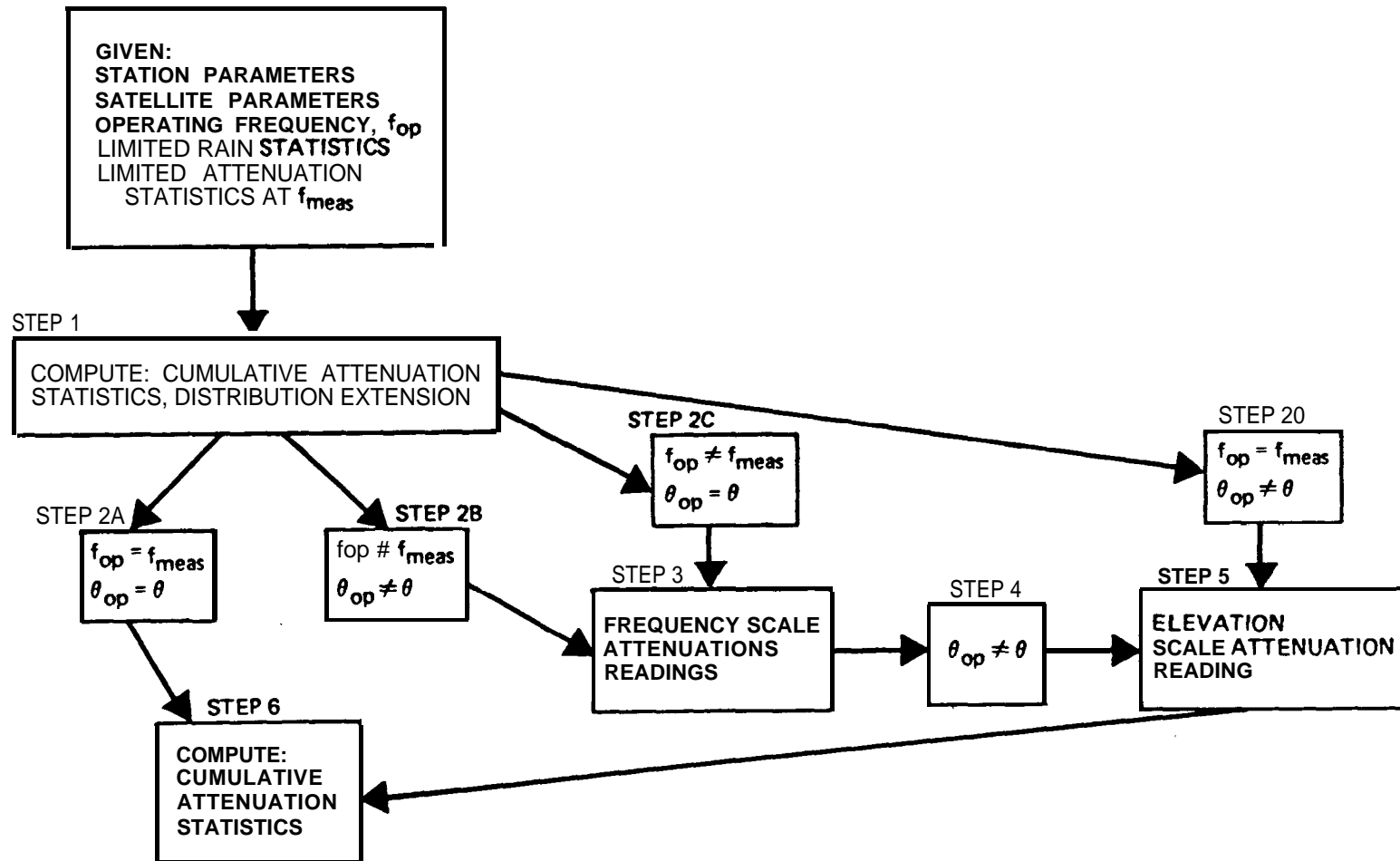


Figure 6.3-10. procedure for Generation of Cumulative Attenuation Statistics Given Limited Rain Rate and Attenuation Statistics

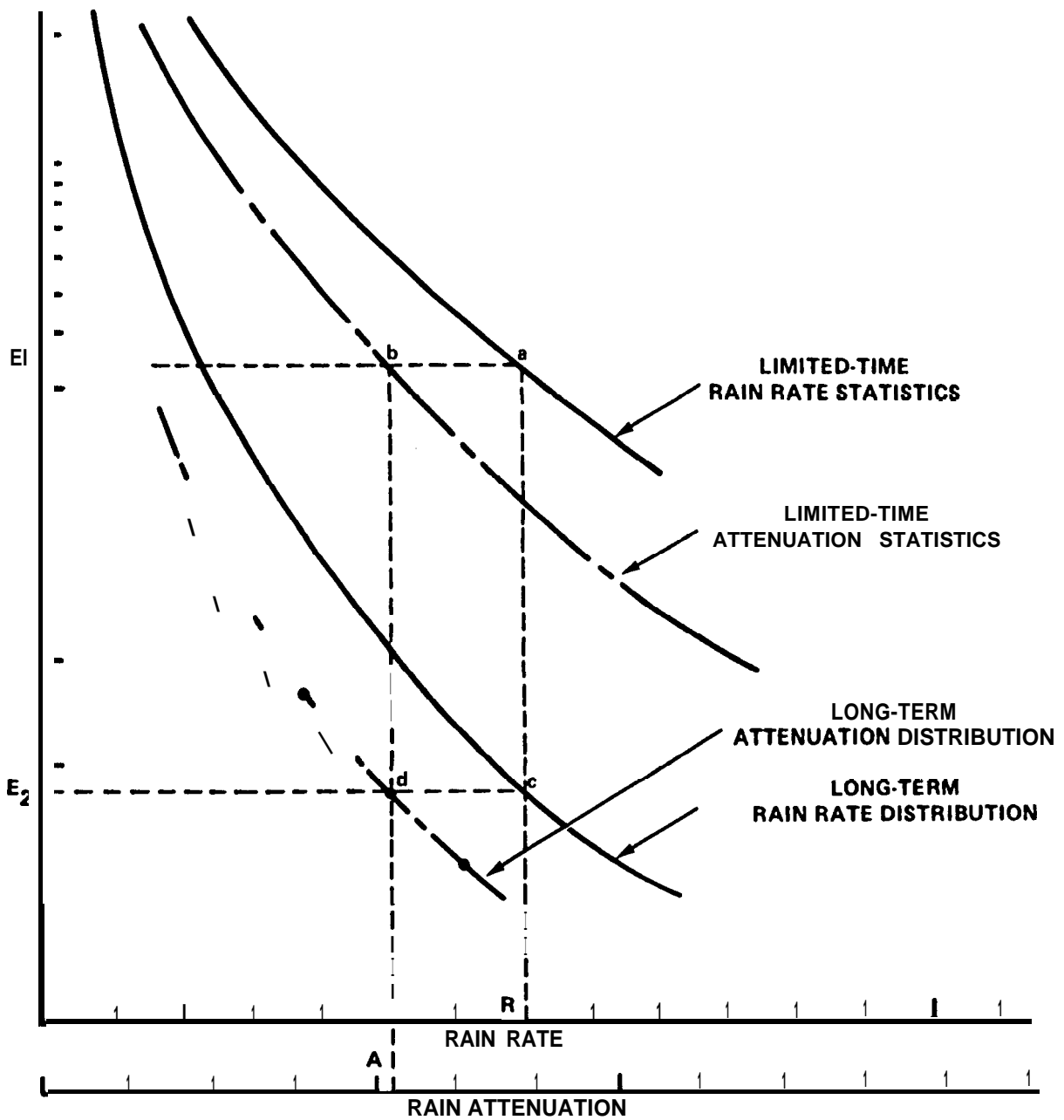


Figure 6.3-11. Construction of Cumulative Attenuation Statistics Using the Distribution Extension Technique

4. Repeat the process for several points and join them with a smooth curve.

Distribution extension in this manner assumes that the values of rain rate and attenuation **remain** the same as the measured **values**, on the average, for times of the year different than the measurement period. This is not necessarily so. The physical distribution of raindrops along the propagation path in a stratiform rain, for example, differs from the distribution in a mild convective storm. Both conditions could produce local rainfall at the same rate, but the attenuation produced could be quite different. Thus in regions where there is wide seasonal variation in how rain **falls**, distribution extension should be used with caution. The reliability of the extended distribution depends on how "typical" of the **whole** year the rainfall was during the measurement period. If the shapes of the limited-time and the long-term distribution curves are similar, the limited-time sample is statistically significant and the distribution extension will be valid.

6.3.4.3 Frequency Scaling. If frequency scaling of measured rain attenuation (Step 3 of Figure 6.3-10) is **required**, the specific attenuation scaling technique is recommended. In this technique specific attenuation data is utilized to scale the attenuation A from frequency f_1 to frequency f_2 . Referring to the equation for rain attenuation in Step 7 of Figure 6.3-1, the result is

$$\frac{A_2}{A_1} = \frac{k_2}{k_1} R_p^{\alpha_2 - \alpha_1} \cong \frac{k_2}{k_1} \quad (\text{for } \alpha_1 \cong \alpha_2) \quad (6.3-17)$$

where

$$A_1 = A_1(f_1), A_2 = A_2(f_2), k_1 = k_1(f_1), \dots, \text{etc.} \quad (6.3-18)$$

This is a fair estimate for small frequency ratios (**e.g., less than 1.5:1**), and moderate rain **rates**, but errors can be large otherwise. This is because the above equation **implicitly** assumes that rainfall

is homogeneous over the propagation path, which is usually not true. By assuming a simple Gaussian model for the rain rate with distance along the **path**, Hedge (1977) derived an expression for attenuation ratio that includes an inhomogeneity correction factor, and uses the high correlation between attenuation and peak rain rate to eliminate the rain rate:

$$\frac{A_2}{A_1} = \frac{k_2}{k_1} \left(\frac{A_1}{k_1} \sqrt{\frac{\alpha_1}{\pi}} \right)^{\frac{\alpha_2}{\alpha_1} - 1} \sqrt{\frac{\alpha_1}{\alpha_2}} \quad (6.3-19)$$

This yields a better fit to empirical data.

6.3.4.4 Elevation Angle Scaling. Step 5, the elevation angle scaling between the operational elevation angle θ_{op} and the measured data angle θ_{meas} is somewhat complex. The first order approximation, the cosecant rule, is recommended, namely

$$\frac{A(\theta_2)}{A(\theta_1)} = \frac{\text{csc } \theta_2}{\text{csc } \theta_1} = \frac{\sin \theta_1}{\sin \theta_2} \quad (6.3-20)$$

If more detailed calculations are desired the full formulas in Figure 6.3-1 are utilized.

6.3.4.5 Example of Distribution Extension. Figure 6.3-12 shows an example of applying the distribution extension technique. The upper two curves are cumulative rain-rate and attenuation statistics derived from more than 600 total minutes of measurements over the July through December 1974 period. The bottom curve in the figure is the measured distribution of rain rate for the entire six-month period (263,000 minutes). Comparison of the two rain rate distributions shows that they are very similar in shape. This indicates that the rain rate measurements made during attenuation measurements are a statistically significant sample of the total rainfall, and that using the distribution extension technique is

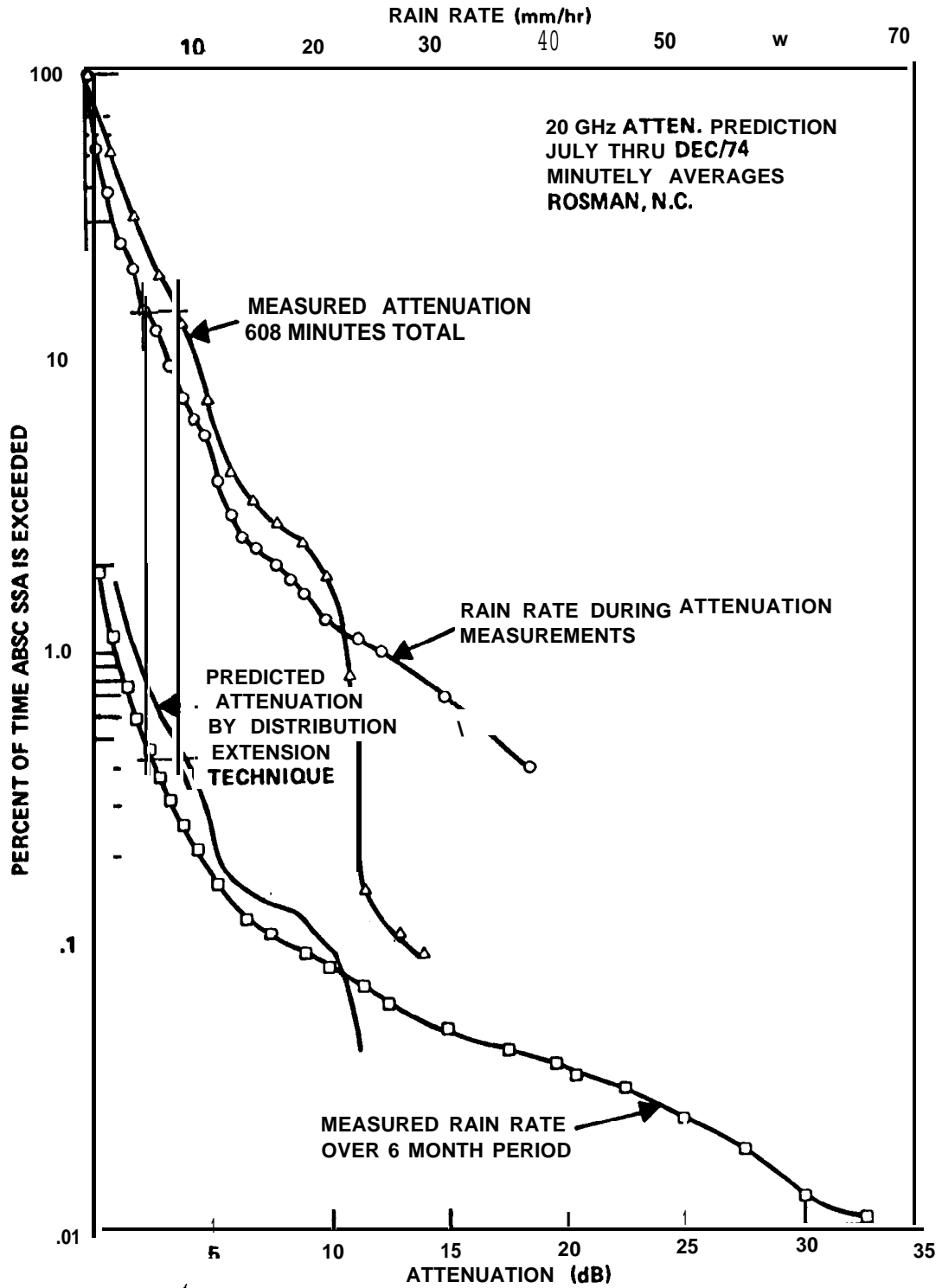


Figure 6.3-12. Example of Distribution Extension Technique

valid. The extended attenuation distribution, constructed as described in paragraph 6.3.4.2, is shown in the figure.

6.3.5 Fading Duration

System designers recognize that at some level of rain rate R_m the entire system margin will be utilized. The cumulative rain rate statistics indicate the percentage of time the rain rate exceeds R_m . In this section, a technique is presented for estimating an upper bound on the duration of the periods that the rain rate exceeds a given R_m . This is equivalent to the duration of fades exceeding the depth corresponding to R_m .

Experimental fade duration statistics are presented in Chapter 5 (Section 5.6). As mentioned in that section, experimental data has confirmed that the duration of a fade greater than a given threshold tends to have a log-normal probability distribution. This is equivalent to the logarithm of the duration having a normal distribution. Given sufficient experimental data, one may determine the parameters of the best-fitting log-normal distribution, and use these to extrapolate from the empirical distribution. Such extrapolation could be used in lieu of, or in addition to, the technique described here when fade duration data is available.

6.3.5.1 Estimating Fade Duration Versus Frequency of Occurrence.

The US and Canadian weather services have published maximum rainfall intensity (rain rate) - duration - frequency curves which provide the point rain rates for several hundred locations on the North American continent (**U.S.** Dept. **Comm.-1955** and Canada Atmos. Env.-1973). Two typical sets of curves for the close-proximity cities of Baltimore, MD and Washington, **D.C.** are shown in Figure 6.3-13. The return periods are computed using the analysis of **Gumbel** (1958) since data is not always available for the 100-year return period. These curves are derived from the single maximum rain-rate event in a given year and are termed the annual series. For microwave propagation studies, curves that consider all high rain rate **events** are necessary. Such curves, called the partial-duration **series**, are

not normally **available**, but empirical multipliers have been found for adjusting the annual series curves to approximate the **partial-duration series** (Dept. **Commerce-1955**). To **obtain** the **partial-duration curve**, the rain rates on the annual series curve for the desired return period are multiplied by the appropriate factors, given in Table 6.3-4.

Table 6.3-4. Multiplicative Factors to Convert Annual to Partial-Duration Series

RETURN PERIOD (YEARS)	MULTIPLY ANNUAL SERIES RAIN RATE BY
2	1.13
5	1.04
10	1.01
25, 50, 100	1.00

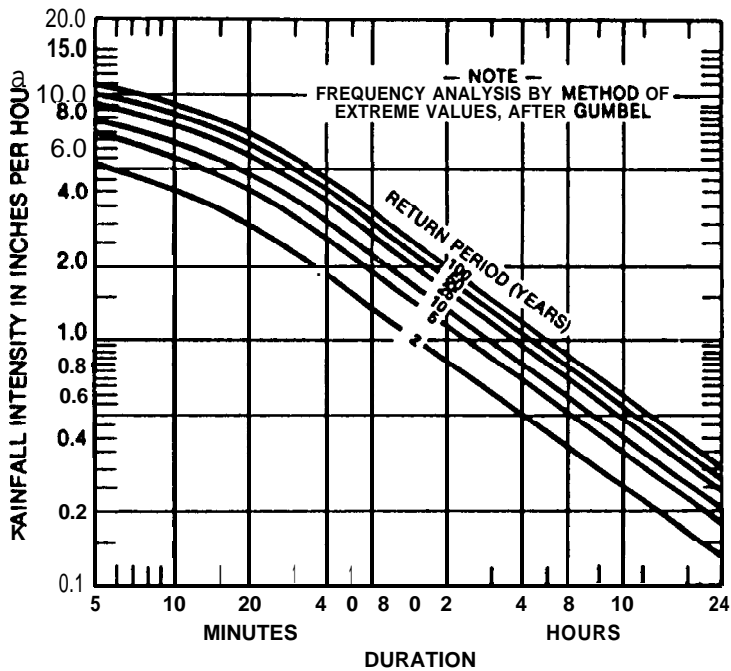
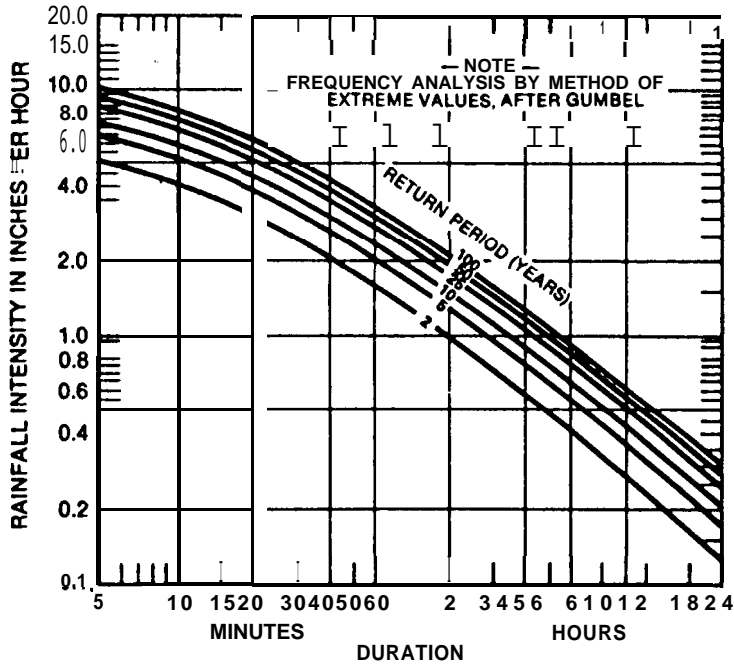


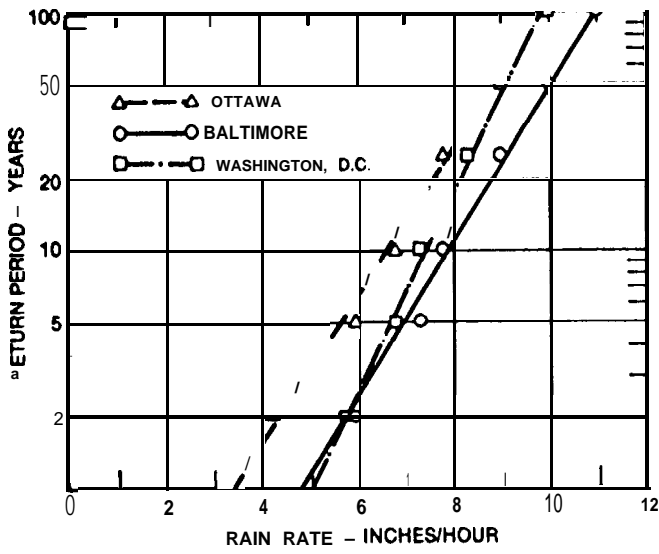
Figure 6.3-13. Typical Rain Rate-Duration-Frequency Curves.
From U. S. Weather Service, Annual Series

The intensity-duration-frequency curves actually give the average rain rate over the duration period, whereas the instantaneous rain rate is of interest from a propagation standpoint. The curves therefore do not directly give the frequency versus duration of fades of a given depth. However, for short averaging periods (e.g., five minutes), the instantaneous rain rate would be expected to stay fairly close to the average rain rate, and would certainly never exceed it for the entire period. The curves then can be used to approximate the frequency of short-duration fades, and to place an upper bound on the frequency in any case.

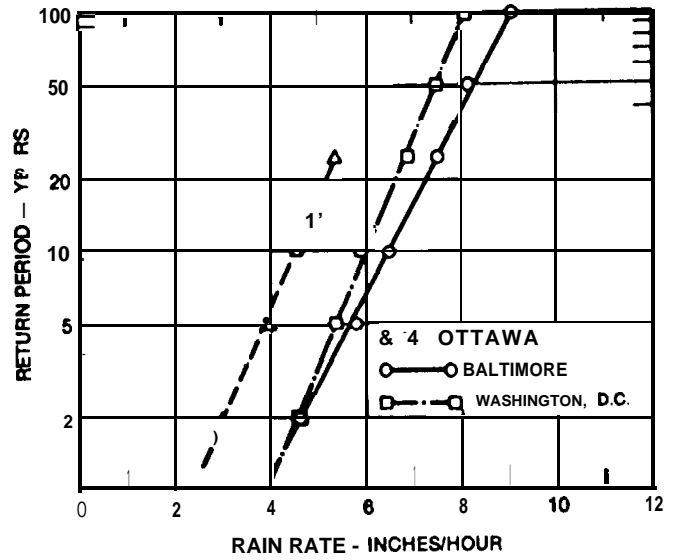
The minimum return period shown on Figure 6.3-13 is two years. It is desirable to be able to extrapolate to one year. This can be done using the **Gumbel** frequency analysis technique for extreme values. This has been accomplished graphically, for durations of 5 through 60 minutes as shown in Figure 6.3-14. The data used in the curves has been adjusted using the multipliers of Table 6.3-4 to correspond to the partial-duration series. For example, the rain rate expected in Baltimore in a 5-minute period once in 2 years is $5.2 \times 1.13 = 5.9$ inches per hour. Extrapolating to one year yields 4.8 inches per hour (122 mm/h). Similar calculations may be done for other duration periods to generate a 1-year return period curve for the partial-duration series.

The recommended technique for estimating the maximum fade period to be expected in an N-year rain event is described in Figure 6.3-15. Here the station parameters (latitude, longitude, etc.), operating frequency and link margin (after clear air attenuation is removed) are required inputs. By iteratively solving the attenuation equation in Figure 6.3-1 the maximum allowable point rain rate R_{pm} is obtained. The estimate of the maximum fade duration for the worst rain in 1,2,5,10 or more years is then obtained from data for the partial-duration series rain rate-duration-frequency curves (see Figure 6.3-9). For example, if the system maximum allowable rain rate R_{pm} is 5 inches/hour (125 mm/hr), a system in

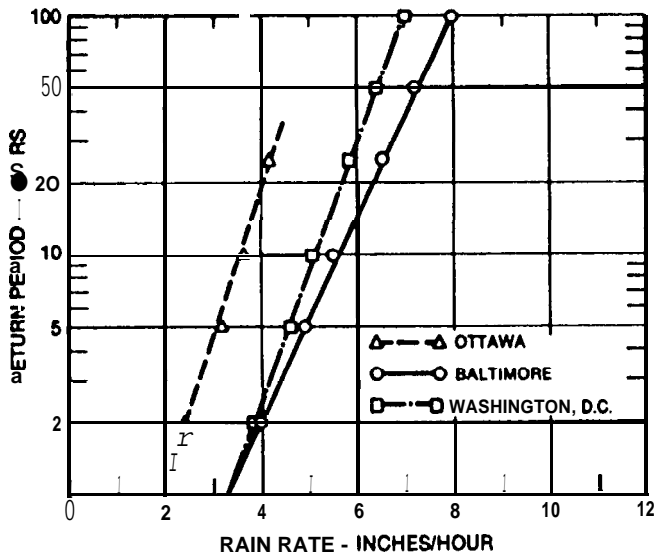
5-MINUTE RAIN RATE



10-MINUTE RAIN RATE



15-MINUTE RAIN RATES



30-MINUTE RAIN RATES

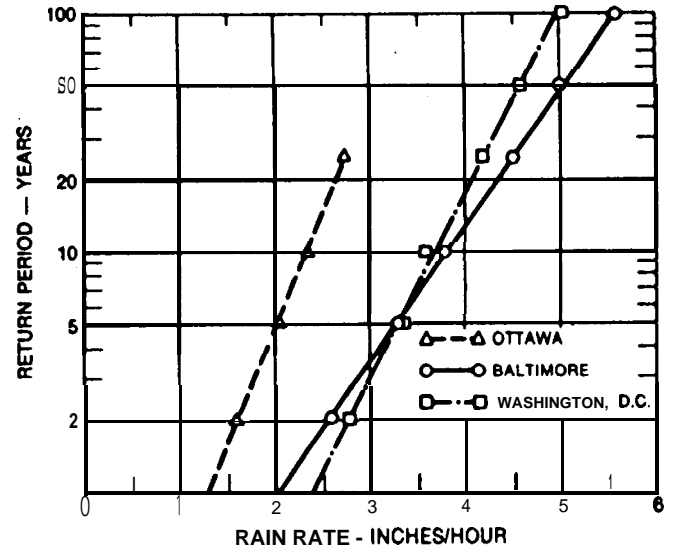


Figure 6.3-14. Extrapolated Partial-Duration Rain Rate-Duration-Frequency Curves

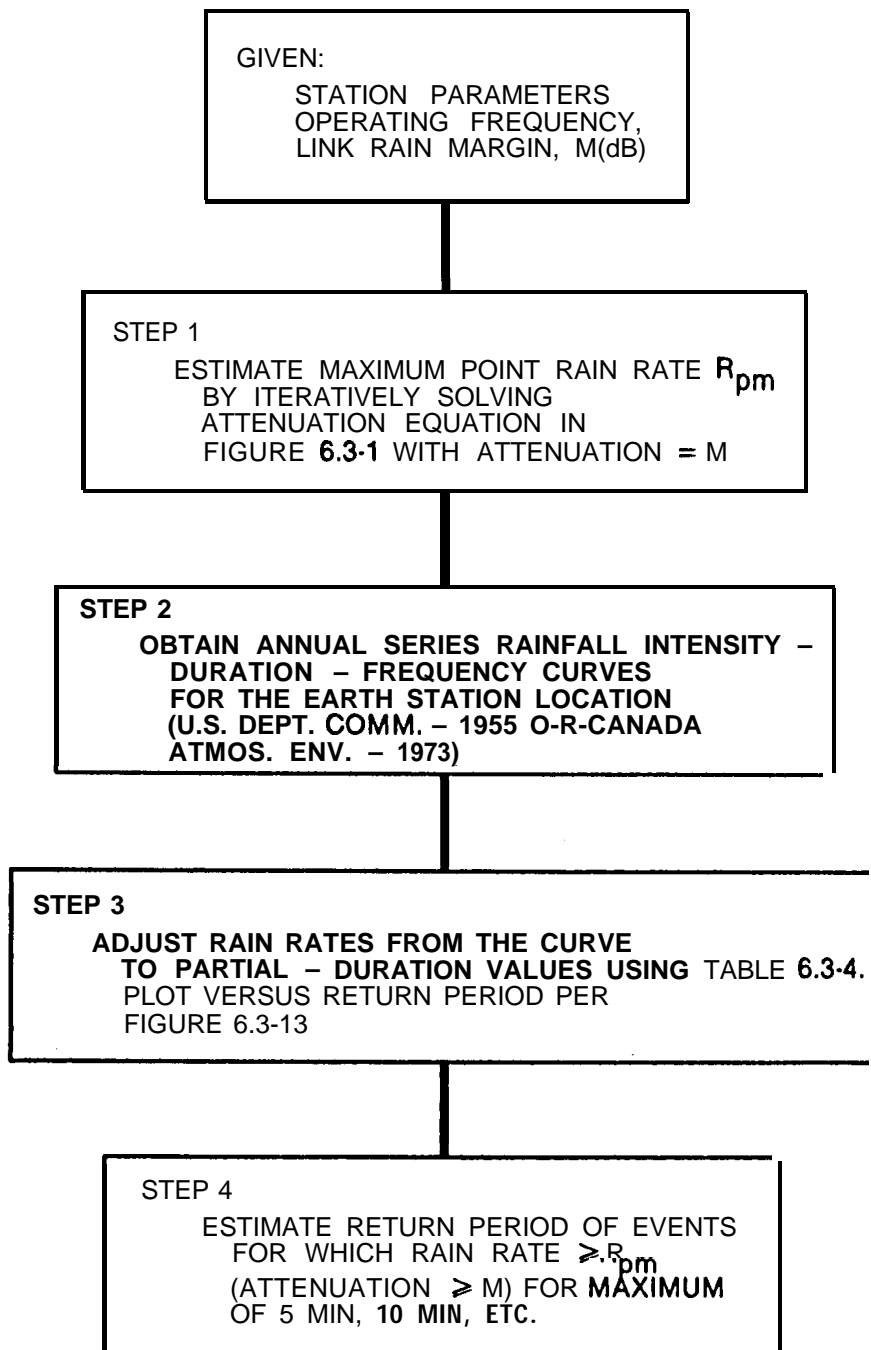


Figure 6.3-15. Technique for Estimating Frequency of Occurrence of Fades of Given Duration

Washington, **D.C.** should on the average expect one maximum 5-minute fade each year, one maximum 10-minute fade every three **years**, etc.

6.3.5.2 Annual and Daily Temporal Distribution of Intense Rain Events. The temporal distribution of rain-induced fade events can be important to a designer since loss of a link during low utilization periods may be tolerable. Figure 6.3-16a shows the distribution, by season, of "record" rainfall events at 207 weather stations throughout the **U.S.** The events are measured in terms of depth-duration, which specifies the total number of inches of rain and the time over which it fell. The durations are shown in the figure, and range from 5 minutes to 24 hours. Figure **6.3-16b** shows the distribution of the maximum events by the times when they start. It is clear that the short-duration events, having the most intense rain (and the deepest fades) occur predominantly in the summer months and during the afternoon hours. There are regional variations of course: throughout much of the west coast, summer rains are insignificant. In the **midwest**, nocturnal thunderstorms are common. The figure also shows that more than 40% of the record 24-hour rainfall events happen in the fall, when steady stratiform rains are the rule. The regional variations in the time distribution of heavy rains is clearly shown in Figure 6.3-17 (Rasmussen- 1971). It gives the time of day of the maximum thunderstorm frequency, based on 10 years' observations. A phenomenon not indicated by the map is the existence of secondary peaks in thunderstorm frequency in many regions.

6.3.6 Rate of Change of Attenuation

Experimental data related to the rate-of-change of attenuation is relatively sparse. Apparently experimenters have not analyzed their measurements to obtain this information except during some extreme attenuation occurrences. Some measurements made at **Rosman, NC** of the CTS 11.7 GHz beacon showed a maximum rate-of-change of 2 **dB/sec** on April 24, 19-7 (**Ippolito-1979**). This translates to change of rain rate from 50 **mm/hr** to 57 **mm/hr** in one second. Assuming this

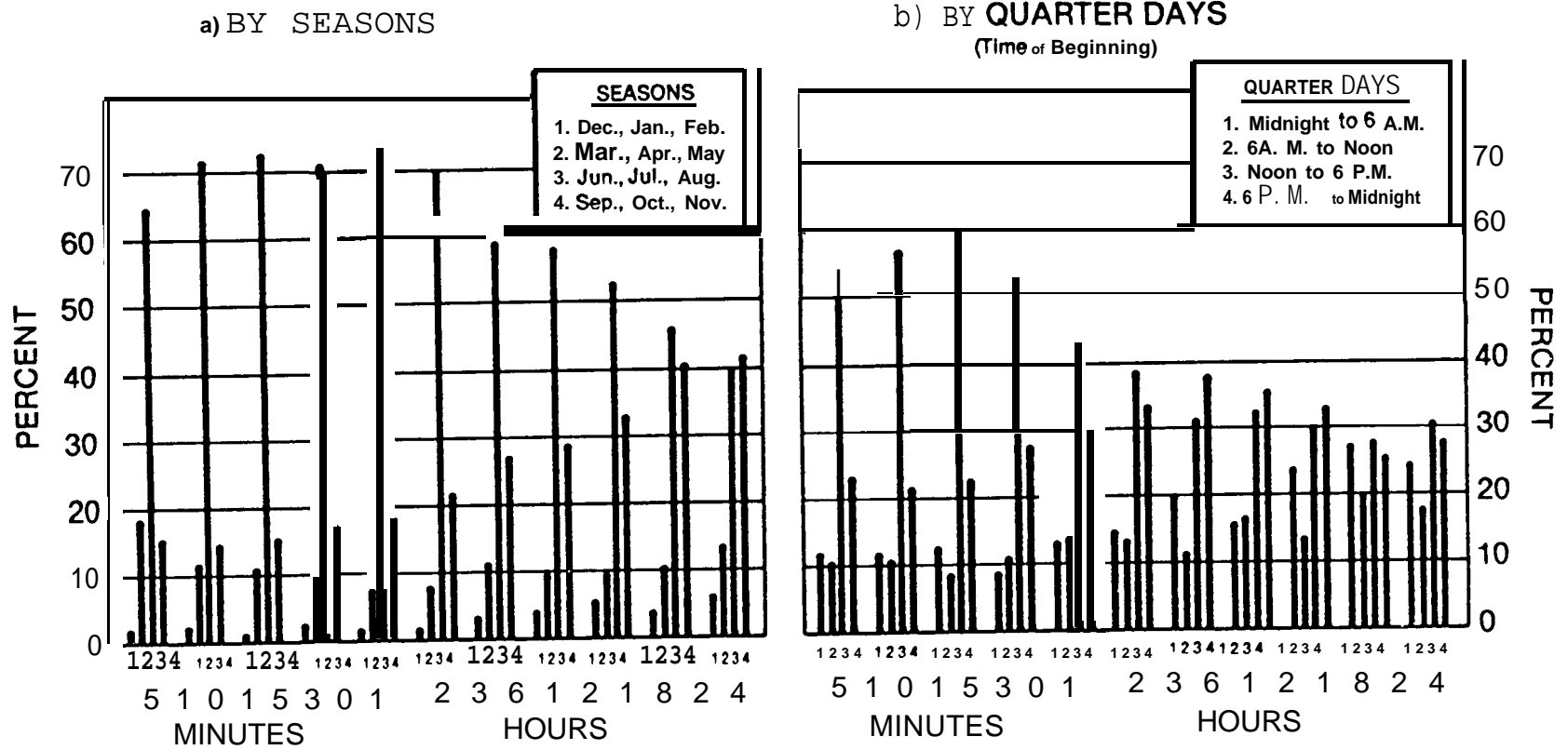


Figure 6.3-16. Distribution of Maximum Rainfall Occurrences at U.S. First-Order Stations (U.S. Dept. Comm.-1947)

change in rain **rate**, the rate of change of attenuation would have been 4 **dB/sec** at 20 GHz.

Maximum fade rates of 0.1 **dB/sec** at 15 GHz are reported by Hedge (1974) and Strickland (1977). Dintelmann (1981) reports fade rates of u-p to 0.6 dB/sec in Europe at 11.7 GHz.

6.3.7 Worst-Month Statistics

Worst-month statistics are of interest to those faced with designing a system to meet performance criteria expressed in terms of a percentage of any calendar month, or of any contiguous 30-day period. The system designer in this case needs to find the percentage of time that some threshold value of attenuation or rain rate will be exceeded within a given month. For every threshold value, there corresponds a month of the year having the highest percentage of time exceeding the threshold (i.e., the percentage exceedance). This is designated the "worst-month" for that threshold. The percentage exceedance in this month, to be expected once every year or every given number of **years**, is of most interest. For high rain rates, the worst-month would probably correspond to the period of highest thunderstorm intensity or frequency, whereas the worst-month for lower rain rates might be when most rainfall is of the steady, stratiform variety.

An exponential model has been devised (Crane and **Debrunner-1978** and **CCIR-1978**, Rpt 723) for estimating the ratio of the Percentage exceedance for a given threshold value in the worst-month to the average annual percentage exceedance for the same threshold. This exponential relationship is expected for statistics of rare events (**Gumbel-1958**).

Let X_{ij} be the percentage exceedance in month i corresponding to a threshold rain rate j . In a given year, there is for each value j a month h with the highest X_{ij} , denoted X_{hj} . The worst-month statistic is the value of X_{hj} that is equalled or exceeded, on average, once in N years where N (the return period) is specified.

The probability that the worst month percentage exceedance is equal to or greater than X_{hj} is given by:

$$P(X_{hj}) = \frac{1}{12N} \quad (6.3-21)$$

The exponential model, which applies when X_{hj} is small, states:

$$P(X_{hj}) = C_{0j} \exp(-X_{hj}/C_{1j}) \quad (6.3-22)$$

where C_{0j} and C_{1j} are empirical constants. Inverting this equation yields:

$$X_{hj} = C_{1j} \ln C_{0j} - \ln P(X_{hj}) \quad (6.3-23)$$

Figure 6.3-18 is a plot of monthly probabilities of exceeding preselected thresholds X_{ij} for 44 consecutive months of attenuation measurements. It clearly follows the straight-line relation of the model, with $C_{0j} = 0.19$ and $C_{1j} = 7.8 \times 10^{-4}$.

The ratio of the N-year worst-month percentage exceedance X_{hj} to Y_j , the average annual percentage exceedance for the same threshold j , is given by

$$Q_{jN} = \frac{X_{hj}}{Y_j} = \frac{\ln(12N C_{0j})}{C_{0j}} \quad (6.3-24)$$

For the case of $N=1$ year, this is bounded by:

$$\frac{12}{M} \leq Q_{j1} \leq 12 \quad (6.3-24)$$

Where M is the number of months in the year that intense rains typically fall. If $M < 3$, the exponential model should be questioned. The lower bound has been shown to be a fair estimate of Q_{j1} for rain rates with annual percentage exceedances in the .001% to .01% range.

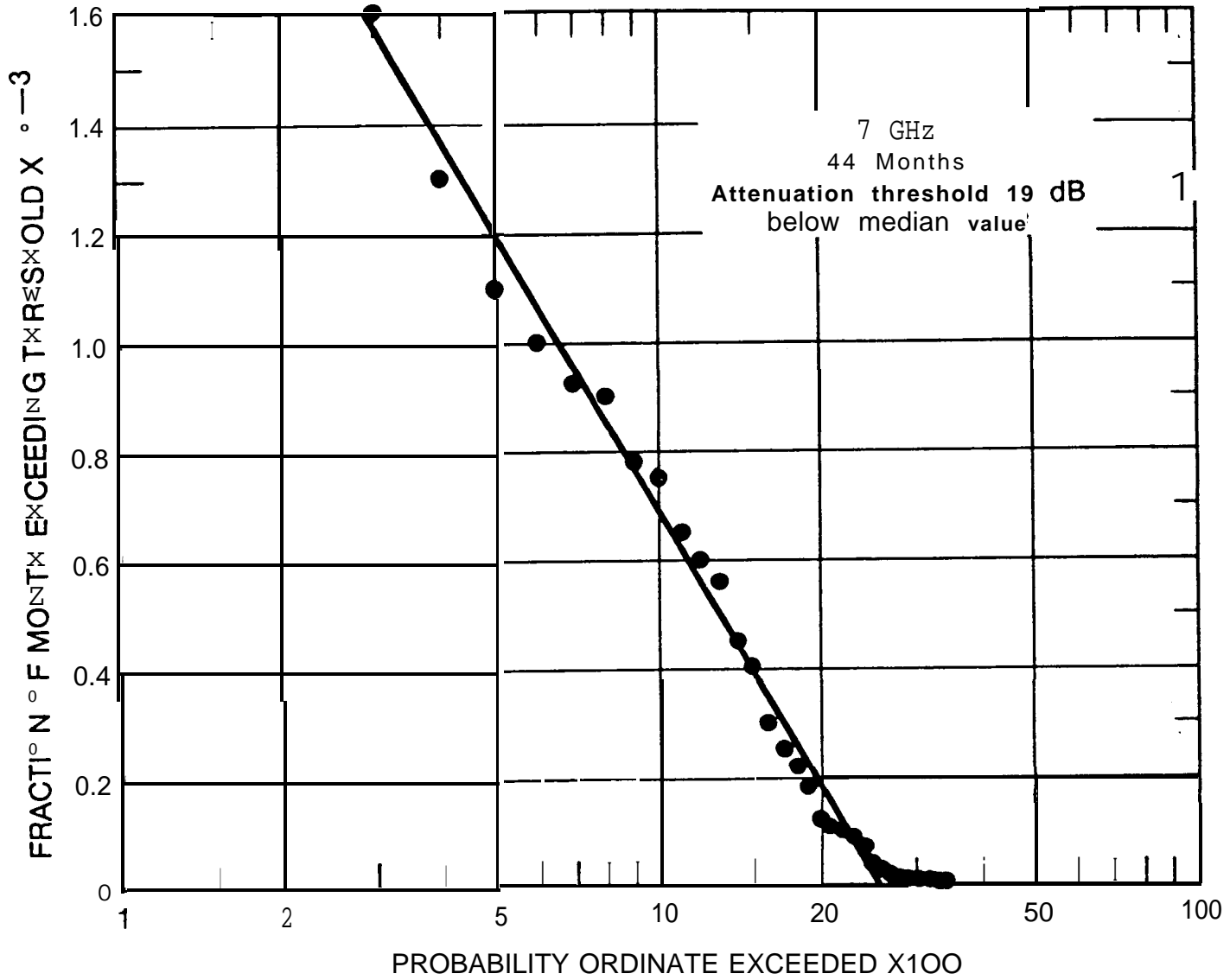


Figure 6.3-18. Probability of Attenuation Threshold Being Exceeded for the Indicated Fraction of Time Per Month (CCIR-1978, Rpt 723)

The worst-month versus annual probability relationship has been found to be closely approximated by a power law of the form

$$\overline{Q} = A\overline{Y}^{-\beta} \quad (6.3-25)$$

where Q is the ratio of the average worst-month probability to the average annual probability (Y) and A and β are coefficients. The observed ranges of coefficient values are $1.2 \leq A \leq 3.3$ and $0.167 \leq \beta \leq 0.074$ (CCIR Rep. 723-1, 1982a). A useful approximate relationship between worst-month exceedance time percentages (p) and annual time percentages (p_w) is (CCIR, 1982a):

$$p = 0.29 p_w^{1.15} \quad (6.3-26)$$

where p and p_w are in percent. The corresponding coefficient values for the previous power law relationship are $A = 1.64$ and $\beta = 0.13$. These values yielded Q ratios in good agreement with average values for different locations in North America and Europe. For current CCIR recommendations, the reader is referred to CCIR report 723-2, "Worst Month Statistics", (CCIR, 1986e).

6.4 CLOUD, FOG, SAND AND DUST ATTENUATION

6.4.1 Specific Attenuation of Water Droplets

The water droplets that constitute clouds and fog are generally smaller than about .01 cm in diameter. This allows the **Rayleigh** approximation to be used to calculate specific attenuation in clouds and fog for frequencies up to 100 GHz. Using this approximation, the specific attenuation α_c is, unlike the case of rain, independent of the droplet size distribution. It is proportional to the liquid water content ρ_l :

$$\alpha_c = K_c \rho_l \text{dB/km} \quad (6.4-1)$$

ρ_l is normally expressed in units of g/m^3 . The attenuation constant K_c is a function of frequency and temperature and is given by Figure 6.4.1 (CCIR Rpt. 721-1, 1982a). The curves given in the figure assume pure water droplets. The values for salt-water droplets, corresponding to ocean fogs and mists, are higher by approximately 25% at 20°C and 5% at 0°C (Koester and Kosowsky-1978).

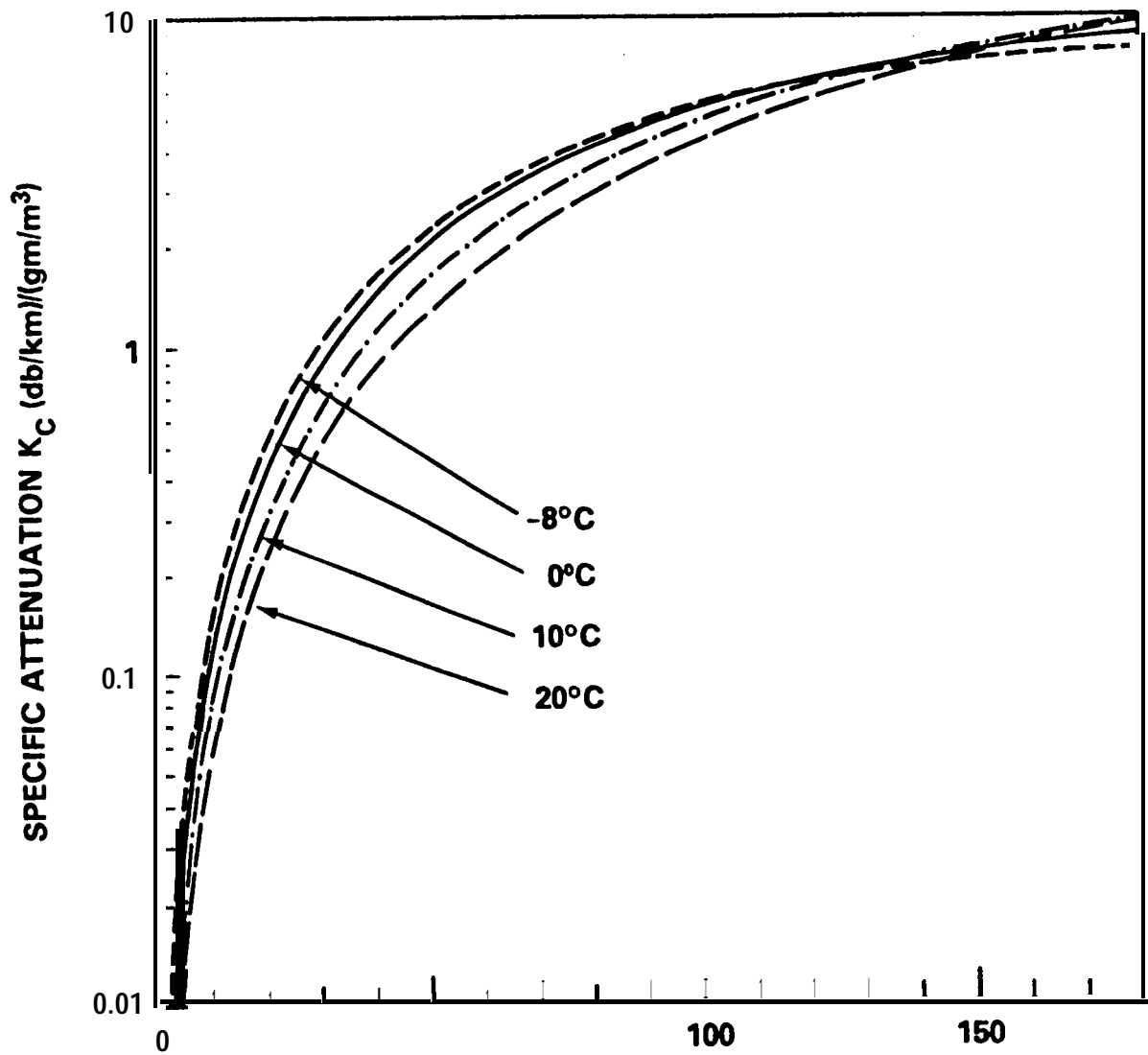


Figure 6.4-1. Attenuation Coefficient K_C Due to Water Droplets
 (from CCIR 1982a, Rpt 721-1)

6.4.2 Clouds

6.4.2.1 Water Content of Clouds. The liquid water content of clouds varies widely. For stratiform, or layered, clouds, the value was observed to most often fall in the range of 0.05 to 0.25 g/m^3 . For the most dense of this type of cloud, stratocumulus, maximum values from 0.3 to 1.3 g/m^3 have been measured (Mason-1971). Cumulus clouds, especially the large cumulonimbus and cumulus congestus that accompany **thunderstorms**, have the highest values of liquid water content. Fair weather cumulus were found to have liquid water contents generally less than 1 g/m^3 . Peak values exceeding 5 g/m^3 were found in cumulus congestus clouds by Weickmann and ~~aufm~~ Kampe (1953). They estimated an average value of 2 g/m^3 for cumulus **congestus** and 2.5 g/m^3 for cumulonimbus. A review of typical values is given in Slobin (1982).

Clouds are not homogeneous masses of air containing evenly distributed droplets of water. Rather, the **liquid** water content can vary widely with location within a single cloud. On the average, the liquid water **content in** smaller cumulus **congestus** clouds increases fairly steadily with distance up from the base, then begins to drop off somewhere in the mid-to-upper parts. It also generally decreases with horizontal distance from the center toward the edges. Small-scale variations are also present, however. Sharp differences have been observed in localized regions on the order of 100 m across. One would expect fairly rapid local variation with time as well, due to the complex patterns of air movement taking place within cumulus clouds. Updraft wind velocities greater than 10 m/s exist within cumulonimbus clouds (Rogers-1976).

6.4.2.2 Measured Attenuation of Clouds. Typical path lengths through cumulus **congestus** clouds probably fall between about 2 and 8 km. Using the estimated average liquid water content from above (2 g/m^3), and the attenuation coefficient from Figure 6.4.1, this implies an added path loss at 35 GHz of about 4 to 16 dB. Fortunately, this calculation grossly overestimates the actual attenuation that has been observed through these clouds. This

appears to be generally true, as seen in Tables 6.4-1 and 6.4-2, which present measurements from two sources.

Table 6.4-1. Zenith Cloud Attenuation Measurements, From Lo, Fannin and Straiton (1975)

Cloud Type	Number of Observations	Mean Cloud Attenuation (dB)		Mean Gaseous Attenuation (dB)	
		35 GHz	95 GHz	35 GHz	95 GHz
Alto cumulus	7	.02	.23	.38	1.93
Altostratus	2	.15	.30	.34	1.73
Strato cumulus	22	.18	.61	.43	2.14
Stratus	8	.13	.12	.42	2.14
Nimbostratus	5	.14	.11	.44	2.32
Cumulus	20	.12	.34	.41	2.12
Cumulonimbus	6	.34	2.36	.40	2.07

Table 6.4-2. Zenith Cloud Attenuation Measurements, CCIR Rpt. 721-2 (1986f)

Cloud Type	Cloud Att	ation (dB)
	95 GHz	150 GHz
stratocumulus	0.5 - 1	0.5 - 1
Small, Fine Weather Cumulus	0.5	005
Large Cumulus	1.5	2
Cumulonimbus	2 - 7	3 - 8
Nimbostratus (Rain Cloud)	2 - 4	5 - 7

In Table 6.4-1, the gaseous attenuation, calculated for the measured surface relative humidity, is given for comparison. The cloud attenuation is in most cases 40% or less of the gaseous attenuation. For frequencies removed from the 35 and 95 GHz "windows," the cloud attenuation would be a smaller fraction of gaseous attenuation. In Table 6.4-1, the number of observations is rather small for all but two types of clouds. The numbers given should therefore not be given undue statistical significance. Also, in using both tables, one should bear in mind the great variability in size and state of development of the clouds observed,

The 35 and 95 GHz data of Table 6.4-1 or 6.4-2 may be roughly scaled in frequency, using the frequency dependence of attenuation coefficient from Figure 6.4-1. Scaling in this manner is quite approximate, as is seen from Table 6.4-1. The ratio of attenuation coefficients at 35 and 95 GHz varies between about 3.9 for -8°C to 6.3 for 20°C . The ratio of average cloud attenuations measured at those frequencies is, from the table, 3.4 for stratocumulus, 2.8 for **cumulus**, and 6.9 for cumulonimbus. In another series of measurements on individual fair weather cumulus clouds (Lo, et al-1975) this ratio was usually between 3.7 and 5.5.

There appears to be a large discrepancy between tables 6.4-1 and 6.4-2 in the attenuation of nimbostratus clouds at 95 GHz. The large values of Table 6.4-2 may be due to the inclusion of precipitation in the path, however, because the presence of nimbostratus clouds would usually be accompanied, sooner or later, by precipitation at the ground station, the higher values of attenuation would be expected. This does not necessarily apply to cumulonimbus clouds, however. Because of the large vertical development and limited horizontal extent of these clouds, a typical ($30-40^{\circ}$ elevation angle) propagation path may be intercepted by them without significant rainfall at the ground station.

6.4.2.3 Statistics of Microwave Effects of Clouds. A JPL study (Slobin 1982), has made estimates of the statistics of cloud effects for the continental U.S., Alaska and Hawaii. The presence of clouds in space-earth downlink antenna beams has two primary effects: signal attenuation and an increase in system noise temperature. For very low-noise receiving systems, such as those used for deep-space communication, the noise effect can be quite significant. Cloud noise statistics may therefore be important in siting such systems and in scheduling their use. Cloud effects can normally be ignored in a high-reliability system designed with a rain margin. However, clouds must be considered for systems with minimal margin that are intended for continuous use, such as a deep-space link receiving unrepeatable spacecraft data.

The JPL study determined that the U.S. could be divided into fifteen regions of statistically "consistent" clouds, as shown in Figure 6.4-2. The region boundaries shown in the figure are highly stylized and should be interpreted liberally. Some boundaries coincide with major mountain ranges (Cascades, Rockies, and Sierra Nevada), and similarities may be noted between the cloud regions and the rain rate regions of the Global Model. Each cloud region is considered to be characterized by observations at a particular National Weather Service observation station. The locations and three-letter identifiers of these stations are shown in the figure. For each of these stations, an "average year" was selected on the basis of rainfall measurements. The "average year" was taken to be the one in which the year's monthly rainfall distribution best matched the 30-year average monthly distribution. Hourly surface observations for the "average year" for each station were used to derive cumulative distributions of zenith attenuation and noise temperature due to oxygen, water vapor, and clouds, for a number of frequencies ranging from 8.5 to 90 GHz.

The following method was employed to calculate the cumulative distributions.

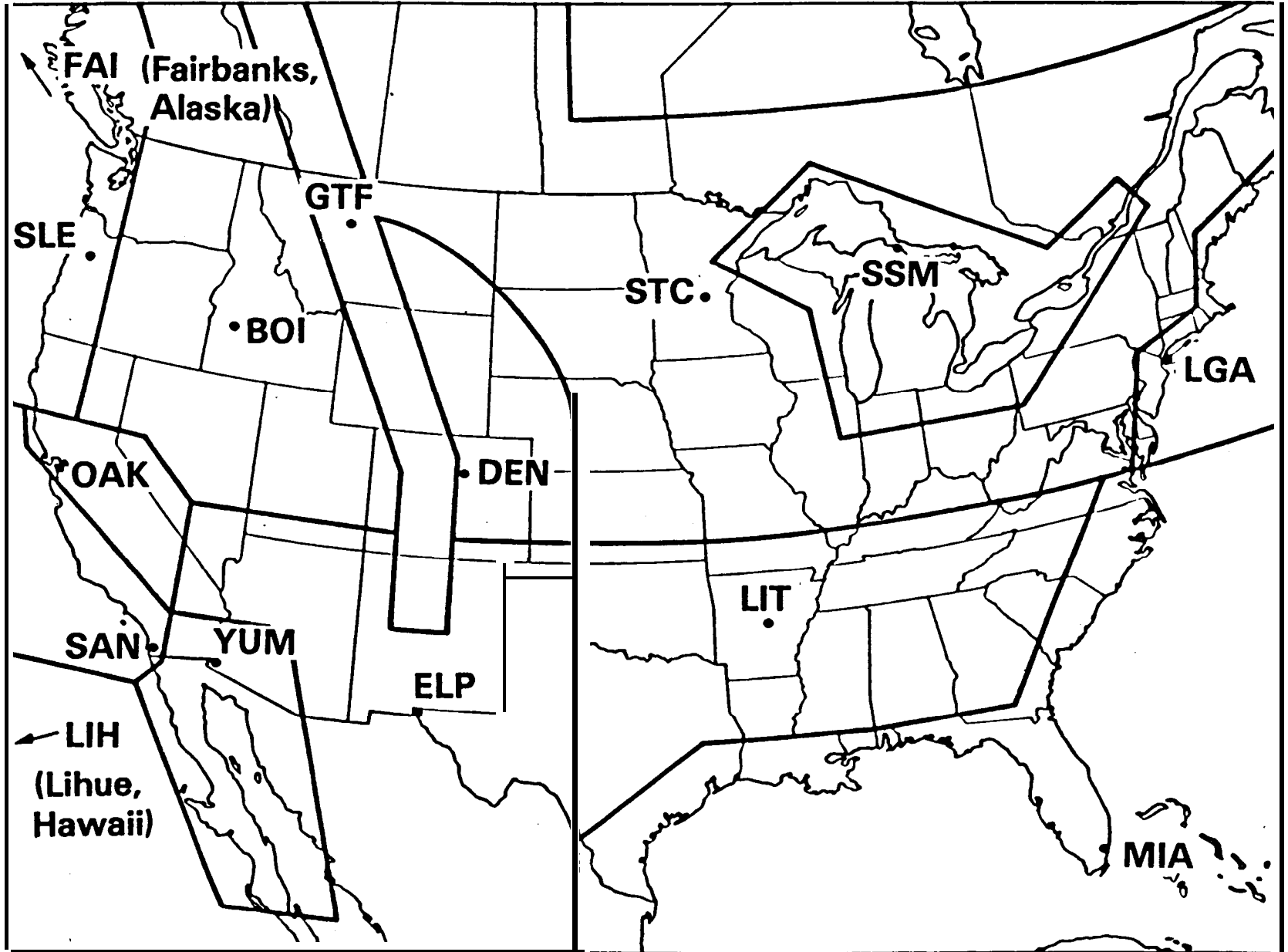


Figure 6.4-2. Consistent Cloud Regions

- For each hour's observations, the attenuation of each reported cloud layer (up to four) was calculated based on the layer's" water particle **density**, thickness, and temperature. The attenuation due to water vapor and oxygen was also found using the reported surface conditions.
- . Total attenuation and noise temperature due to all cloud layers and gases were calculated for sixteen possible cloud configurations, corresponding to all combinations of cloud presence or absence at the four layer heights.
- . Cumulative probability distributions for attenuation and noise temperature were calculated using the reported **percent-** coverage values corresponding to each cloud layer. For example, if the percentage of coverage was 60 percent for layer 1 and 20 percent for layer 2, then the probability of various configurations of clouds present in the antenna beam would be as follows:

no clouds present:	$(1-.6) (1-.2) = 0.32$
layer 1 clouds only present:	$(.6) (1-.2) = 0.48$
layer 2 clouds only present:	$(1-.6) (.2) = 0.08$
clouds in both layers present:	$(.6) (.2) = 0.12$

Typical cumulative attenuation and noise temperature distributions calculated in this way are shown in Figure 6.4-3. The curves apply to zenith paths only, but can be extended to slant paths using a cosecant law. Such extension will probably lead to overestimation at low elevation angles and small time percentages. This is because clouds with large vertical development have less thickness for slant paths than for zenith paths. At time percentages where rain effects become significant (cumulative distributions greater **than 95%**), the **attenuation and noise** temperature due to the rain should be considered also.

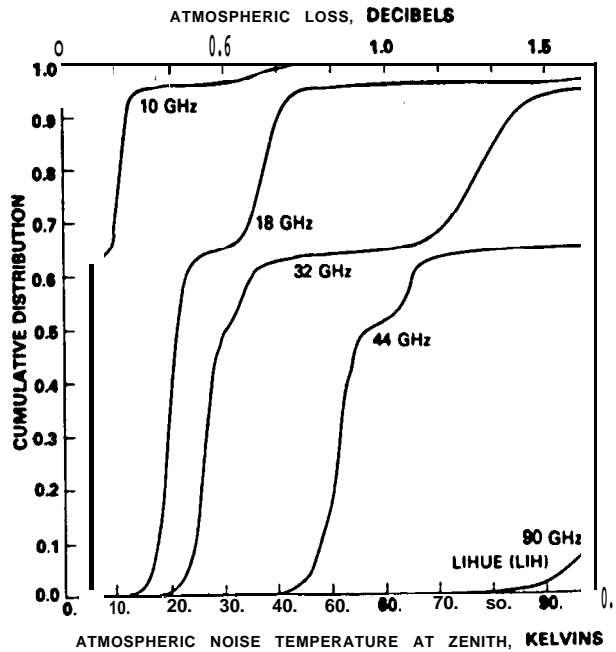
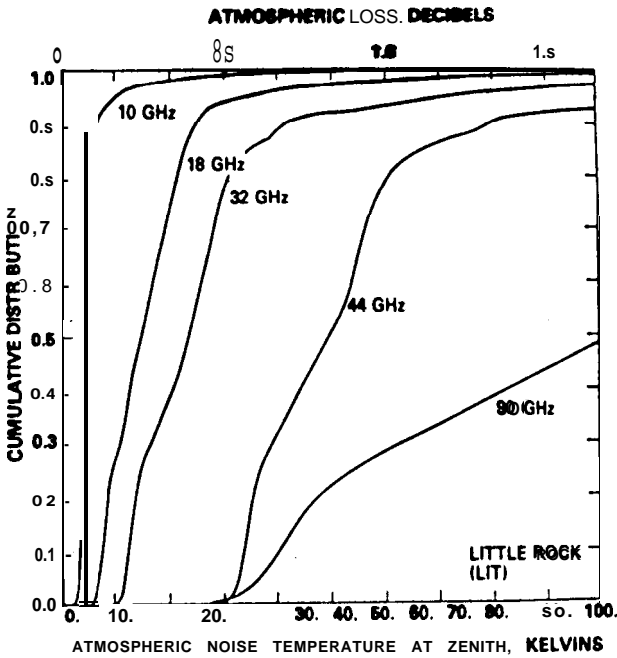
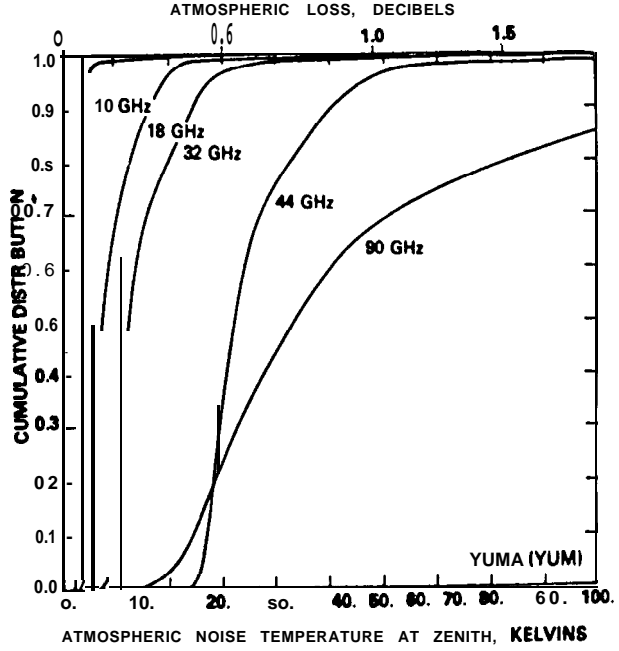
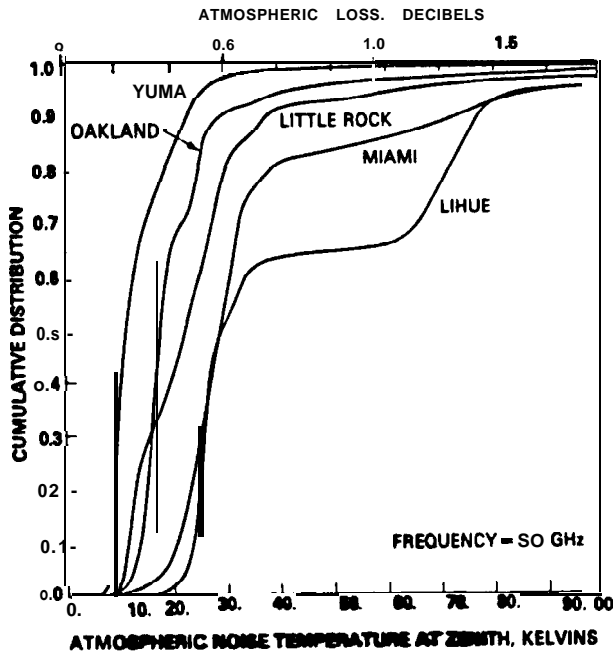


Figure 6.4-3. Examples of Cloud and Gaseous Effects Statistics

Plots of noise temperature and attenuation statistics, both full-year and quarter-year, are available for the 15 regions at 15 frequencies (8.5, 10, 12, 15, 18, 20, 25, 28, 30, 32, 35, 39, 44, 49 and 90 GHz). Interested persons should contact Stephen Slobin, Jet Propulsion Laboratory, Pasadena, CA 91109.

6.4.3 Fog

6.4.3.1 Water Content of Fog. Fog results from the condensation of atmospheric water vapor into water droplets that remain suspended in air. Fog is characterized by optical visibility, which is defined as the distance over which a black target against the sky horizon background can **just** be discerned by the human eye. The international definition of fog is satisfied when visibility is less than one kilometer (Koester and Kosowsky-1970).

There are two main types of fog, differing in the locale and method of formation. Advection fog is coastal fog that forms when **warm**, moist air moves over colder water. The liquid water content of advection fog does not normally exceed 0.4 g/m³. Radiation fog forms inland at night, usually in valleys and low marshes, and along rivers. Radiation fog can have a liquid water content up to 1 g/m³. Empirical relations have been found (Koester and Kosowsky-1970) between the liquid water content, ρ_l , and the visibility, $V(\text{km})$:

$$\rho_l = (18.35 V)^{-1.43} \text{ for advection fog} \quad (6.4-2)$$

$$\rho_l = (42.0 V)^{-1.54} \text{ for radiation fog} \quad (6.4-3)$$

6.4.3.2 Attenuation of Fog. The specific attenuation of fog (in dB/km) is estimated using the curves in Figure 6.4-1. The 10°C curve is recommended for the summer, and the 0°C curve should be used for other seasons. Typical liquid water content values for both types of fog vary between about 0.1 and 0.2 g/m³. The specific attenuation of this, assuming a temperature of 10°, would be about 0.08 to 0.16 dB/km at 35 GHz, or 0.45 to 0.9 dB/km at 95 GHz. (See Figure 6.4-1.) In a typical fog layer 50 m thick, a path at a 30° elevation angle would be in the fog only 100 m, producing less than 0.1 dB of

attenuation at 95 GHz. This suggests that fog attenuation **would**, in most cases, be negligible.

6.4.3.3 Fog Attenuation Estimation Method. A relatively **simple** procedure for the estimation of fog attenuation from fog density or fog visibility data has been developed by **Altshuler** (1984). A regression analysis was performed on a large set of fog attenuation data over a wide range of frequencies (10 to 100 **GHz**) and temperatures (**-8 to 25°C**), using tabulated values of indices of refraction. The resulting analysis produced the following expression:

$$a_f = -1.347 + 11.152/f + 0.060f - 0.022T \quad (6.4-4)$$

where

a_f is the normalized fog attenuation, in **dB/km/g/m³**

f is the frequency in **GHz**, and

T is the temperature in **°C**

The total fog attenuation is found by multiplying a_f by the fog density, in **g/m³**, and the fog **extent**, in km. Unfortunately, the fog density is not easily obtainable, and can vary greatly. Fog, however, is often characterized by visibility, which is much easier to measure than fog density.

The fog density, M, is empirically related to the visibility, V, by:

$$M = (0.024/V)^{1.54} \quad (6.4-5)$$

where V is in km, and M is in **g/m³**.

The total fog attenuation, A_f (**dB**), is then available from:

$$A_f(\text{dB}) = a_f * M * L_f \quad (6.4-4)$$

where L_f is the fog extent, in km.

The standard error of the estimation procedure described above is 0.14 db. The author recommends in a later publication that the procedure should not be used for frequencies below 30 GHz, since the error is comparable in magnitude to the fog attenuation itself (Altshuler-1986) .

As an example of an application of the procedure, consider a link at 44 GHz, with a fog visibility of 120 m (0.12 km). The fog density is then

$$M = (0.024/0.12)^{1.54} = 0.0839$$

The normalized fog attenuation, at a temperature of 25°C, will be, from Eq. (6.4-4);

$$a_f = 0.996 \text{ dB/km/g/m}^3$$

The total fog attenuation, assuming a fog extent of 2 km, will then be, from Eq. (6.4-6)

$$A_f \text{ (dB)} = (0.996)(0.0839)(2) = 0.167 \text{ dB}$$

The fog attenuation, as expected, is very low, and is not usually a factor in satellite link system design for frequencies below 100 GHz .

6.4.4 Sand and Dust Attenuation

Sand and dust scatter electromagnetic energy and their effect may be evaluated via Mie scattering. To date simulated measurements have been carried out in the laboratory (Ahmed and Auchterlouis-1976) . At 10 GHz and concentrations of sand and dust less than 10-5 g/m³ the measured specific attenuation was less than 0.1 dB/km for sand and 0.4 dB/km for clay. Severe storms have concentrations exceeding these values.

Ghobrial, et al (1978) have calculated a theoretical specific attenuation for sand. Based on the characteristics of particles collected during sandstorms, they conclude that negligible attenuation is suffered by X-band transmissions through sandstorms. This is due to the small particle size compared to the wavelength and the low loss tangent for sand.

Chu (1979) reported that attenuation coefficients from sand particles at microwave frequencies were linearly proportional to frequency, and inversely proportional to optical visibility. The attenuation coefficients for distributions of identical particles were linearly proportional to particle radius. Other theoretical analyses have shown that sand and dust particle attenuation at microwave frequencies tends to be significant at very high particle concentrations (visibilities of less than **20m**), or at high moisture contents, or both [**Bashir** et al. (1980), Ansari and Evans (1982), **Goldhirsh** (1982)].

Blowing sand and dust storms occur in some regions of the U.S. These are recorded by the Weather Service as part of the Local **Climatological** Data (LCD) at the 291 stations. Ground stations needing this information should review the data recorded by a nearby LCD recording station.

The vertical extent of these sand storms is unknown, but it seems unlikely that high concentrations would exceed 1 km. The path length is expected to vary between 1/2 and 3 km, generally resulting in a total additional attenuation due to sand of the order of **1 dB** or less. No measured satellite beacon link data is available to confirm these results.

6.5 PREDICTION OF SIGNAL FLUCTUATIONS AND LOW-ANGLE FADING ON EARTH-SPACE PATHS

The amplitude, phase, and angle-of-arrival of a microwave signal passing through the troposphere vary due to inhomogeneities in the refractivity (clear air). The effects occur on time scales shorter

than a minute and on spatial scales shorter than a kilometer. At low elevation angles, the amount of troposphere traversed is **significant**, and **so**, below approximately 10 degree elevation angles, low-angle fading must be considered.

6.5.1 Antenna Aperture Effects

The effects of tropospheric turbulences and the antenna can not be totally decoupled because, of course, the measurements and operating systems utilize antennas. The antenna aperture processes the incident wavefront with its spatial and temporal fluctuations into a received signal with only temporal variations.

Wavefront tilt due to inhomogeneities and gradients in the refractivity appear to the antenna as an angle-of-arrival variation. Average elevation angle ray bending is usually 10 times more pronounced than azimuthal ray bending. However, wave tilt fluctuations tend to be randomly distributed in angle relative to the slant path propagation direction, at least when the majority of the path is above the regime of surface effects (surface effects extend upwards several hundred meters).

Fluctuations occurring on spatial scales smaller than the size of the aperture are often referred to as wavefront ripple. This phase incoherence results in an instantaneous gain loss or degradation.

The fluctuations described herein apply to the ground station downlink because its antenna is in close proximity to the turbulent medium. An uplink satellite path will suffer fluctuation gain degradation only due to scattering of energy out of the path. Because of the large distance traversed by the wave since leaving the troposphere, the wave arrives at the satellite antenna as a plane wave (no ripple) and with only minute angle-of-arrival effects. Interference to satellites on the geostationary arc can occur due to the refraction and diffraction of radio relay links oriented toward the satellite.

6.5.2 Amplitude Fluctuations

6.5.2.1 Overview. The phenomena of amplitude and angle-of-arrival fluctuations combine to form received signal amplitude fluctuations. For many cases of propagation one or more of these effects may often be neglected. For example, a receiving system which employs an antenna with a wide beamwidth will not experience **angle-of-arrival**-induced amplitude fluctuations for most elevation angles. However, such simplification is not always possible. The theory of wave propagation and scattering in random media allows a combination of the turbulence induced effects to be performed in the context of weak fluctuations along a line-of-sight path. The work of **Ishimaru (1978)**, which defines coherent and incoherent field components as a plane wave propagates through a random medium, provides a method of combining amplitude and angle-of-arrival effects into a model of received signal amplitude fluctuation. A model utilizing the concept of incident **plane** wave decomposition (see Figure 6.6-1) has been proposed by Theobald and Hedge (1978).

6.5.2.2 Variance of Received Signal Amplitude. The assumption of weak turbulence is invoked for a plane wave incident on a region of turbulence, propagating a distance L_t (km) and impinging on a circular aperture of diameter d_a (meters). The antenna is assumed to have a Gaussian pattern function with half-power beamwidth B (degrees). If v_d is the received signal voltage, assuming a square-law first **mixer**, an expression for signal variance relative to average power is

$$S^2 = 10 \log_{10} \left(\frac{\langle v_d^2 \rangle - \langle v_d \rangle^2}{\langle v_d \rangle^2} \right) \quad (6.5-1)$$

$$= 10 \log_{10} \left(\frac{l_c \sigma_1^2 + \frac{l_i B^2}{5.55 \sigma_2^2 + 4B} - l_i \left(\frac{B^2}{2.77 \sigma_2^2 + B^2} \right)^2}{l_c + l_i \left(\frac{B^2}{2.77 \sigma_2^2 + B^2} \right)} \right)$$

where

$$l_i = 1 - \exp[-L_t/L_0]$$

$$l_c = (1 - l_i) / (1 + \sigma_1^2)$$

$$\sigma_1^2 = \text{electric field amplitude variance}$$

σ^2_2 = angle-of-arrival variance (deg²)

L_t = path length

L_0 = a function of density and crosssection of scattering along the path.

Measurements at The Ohio State University of the **ATS-6**, 20 and 30 GHz beacons as the satellite underwent synchronous orbit transition were used to derive empirical constants for this model. The path length, L_t , was determined as a function of elevation angle, θ , using an effective turbulence height, h_t , of 6 km in the formula

$$L_t = \left[h_t^2 + 2r_e h_t + (r_e \sin \theta)^2 \right]^{1/2} - r_e \sin \theta \quad (6.5-2)$$

where r_e = mean earth radius = 6371 km.

The constants were

$$L_0 = 180 \text{ km}$$

$$\sigma^2_1 = 2.6 \times 10^{-7} f(\text{GHz})^{7/12} L_t(\text{km})^{11/6}$$

$$\sigma^2_2 = 5.67 \times 10^{-6} L_t(\text{km})^{1.56} d_a(\text{m})^{-1/3}$$

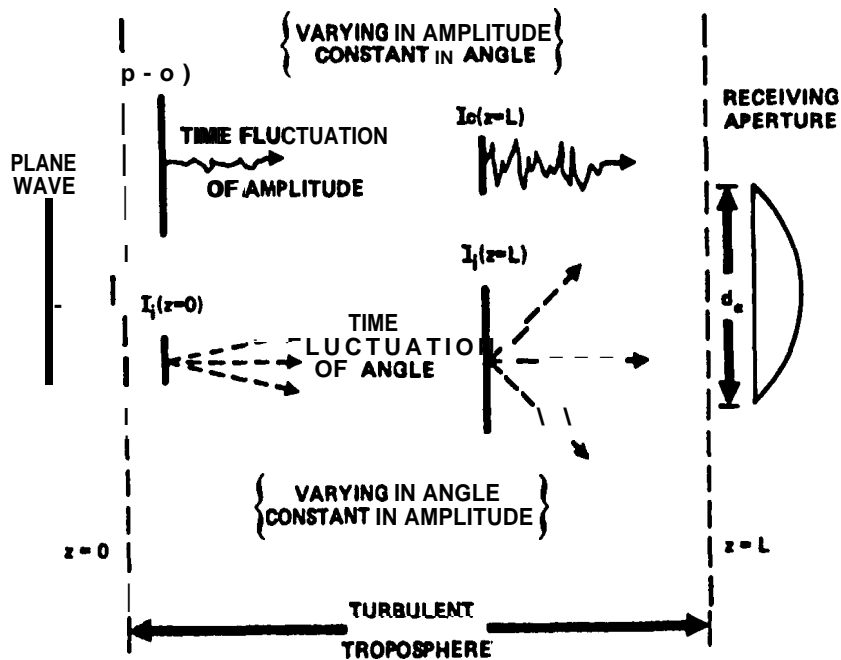


Figure 6.5-1. Decomposition into Coherent and Incoherent Components

A plot of the variance measurement, S^2 , expressed in, dB, is shown in Figure 6.5-2 for four representative frequencies for a 4.6 m diameter aperture. S^2 is plotted as a function of elevation angle and equivalent path length for a 6 km high region of turbulence.

Figure 6.5-2 represents the average s^2 as derived from the O.S.U. empirical constants. However, since both σ^2_1 , and σ^2_2 may be represented in closed form as a function of C^2_n (Tatarski-1961), instantaneous, diurnal, or seasonal values for s^2 may be found from this model given an estimate of the appropriate C^2_n .

6.5.2.2.1 Applicability of the Model. The empirical constants which were found from observed data are applicable for the prediction of average turbulence-induced propagation effects in a temperate climate, during the warmer seasons of the year, and under non-precipitating clear-air conditions. It is necessary to derive local estimates of C^2_n for the model if these conditions are not the same.

6.5.2.2.2 Distribution of Amplitude Variance. It is known that peak-to-peak variations of 30 N-units in the refractive index are expected on a time scale of days and hours (Theobald-1978). Corresponding fluctuations in received signal amplitude variance expressed in dB would be expected to be about 20 dB peak-to-peak for a fluctuation of 30 N-units out of an average of 345. Figure 6.5-3 shows a representative case of average amplitude variance at 30 GHz for a 4.6 m diameter aperture as a function of elevation angle. Curves for plus or minus 10 dB variation in C^2_n about the average are shown for comparison.

A more exact representation of the expected distribution of amplitude variance may be obtained given measured statistics of variance variability about the average. Figures 6.5-4a and b present probability distribution functions of variance differences for 2 and 30 GHz earth-space signals measured over a period of 26 days. The satellite was undergoing transition in elevation from 0.38° to 45° and the mean variance was removed as a function of elevation angle. The 90% confidence limits of 14.6 and 14.7 dB, respectively, are in good agreement with the statistics of expected refractive index variation.

08-9

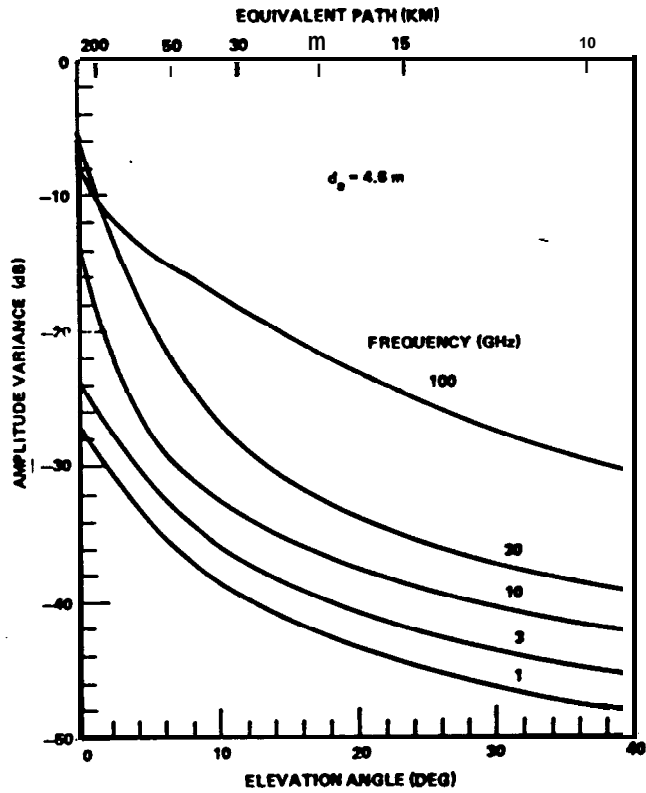


Figure 6.5-2. Amplitude Variance for a 4.6M Diameter Aperture for 1 to 100 GHz

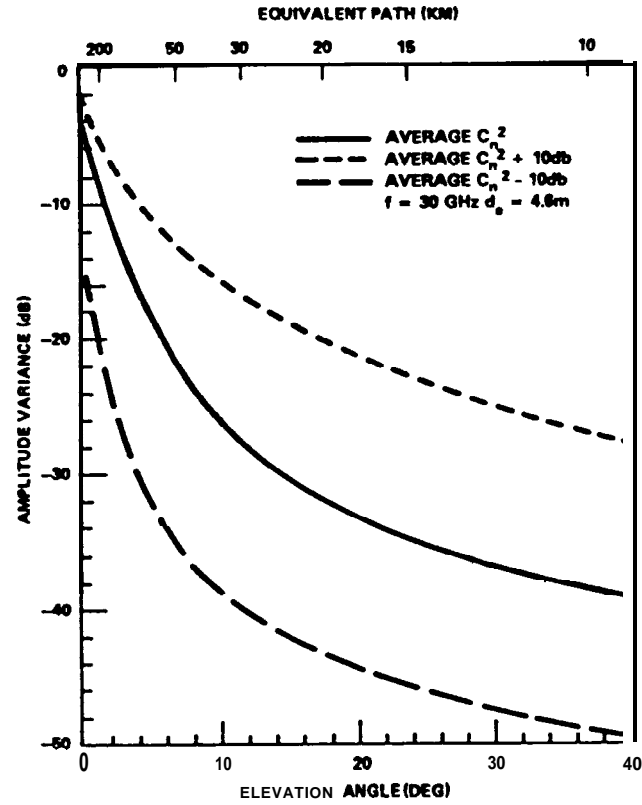


Figure 6.5-3. Effect of 20 dB Peak-to-Peak (30 N-units) Variation of C_n^2 on Amplitude Variance

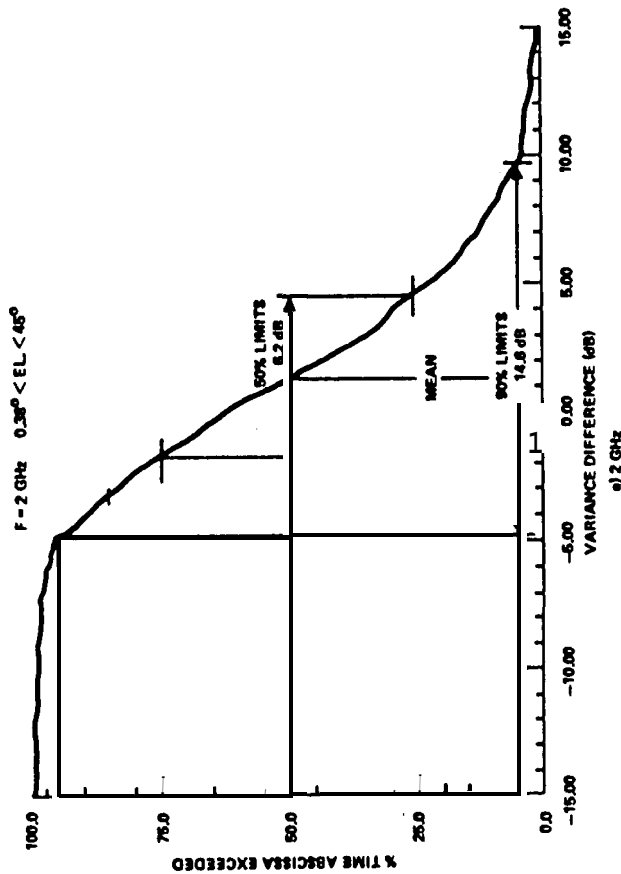
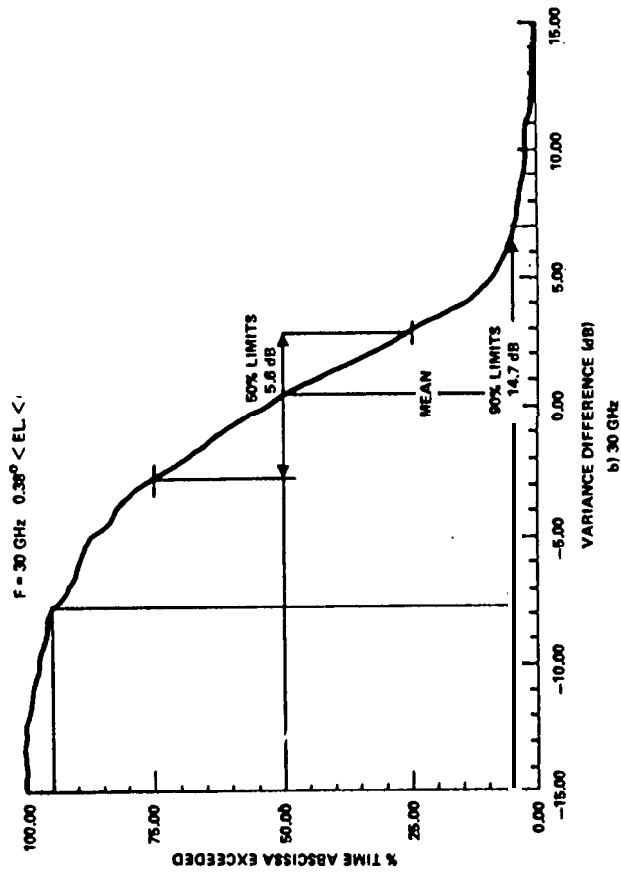


Figure 6.5-4. Distribution of Amplitude Variance from that Predicted from Average Turbulence-Induced Fluctuation Theory

6.5.2.2.3 Power Spectral Density. The formulation of the structure of the power spectral density of turbulence-induced amplitude fluctuations has been derived from classical turbulence theory (**Tatarski-1961**). The theoretical spectrum of amplitude fluctuations in a medium characterized by a real refractive index is found to roll off as $f_f^{-8/3}$, or **-26.6 dB/decade**, in fluctuation frequency f_f . This behavior is not a function of operating frequency, as long as the wavelength is small or on the order of the smallest refractive inhomogeneities. Deviation from this slope will occur due to **non-stationarity** of the scintillation process.

The spectral slope was calculated for time records of 102,4 seconds at 2 and 30 GHz on the **ATS-6** CW beacons as the satellites moved in elevation angle from 0.38 to 25 degrees (Baxter and Hodge-1978). Spectral slope was found to be essentially independent of equivalent path length and measured statistics were well centered about the theoretical value of **-26 dB/decade**. Figures 6.5-5a and b present the probability distribution functions of the 2 and 30 GHz spectral slopes, respectively. Figure 6.5-6 presents the worst-case confidence limits of distribution of spectral slope from an average **-26.6 dB/decade**, for 50% and 90% of total time. Such an estimate may be used to directly find the expected fading rates and spectral components due to turbulence-induced amplitude scintillation. The data represents clear air statistics over a period of 26 days.

6.5.2.2.4 Estimation of Gain Degradation. The model for received signal amplitude variance has also been used to derive an expression for gain reduction, R, defined by (**Theobald and Hedge - 1978**)

$$R = 10 \log_{10} \frac{\langle v_d^2 \rangle}{\langle v_d^2 \rangle_{\text{no angle fluctuation}}} \tag{6.5-3}$$

$$R = 10 \log_{10} \frac{I_c + I_i \left| \frac{B^2}{2.77 \sigma_2^2 + B^2} \right|^2}{I_c + I_i}$$

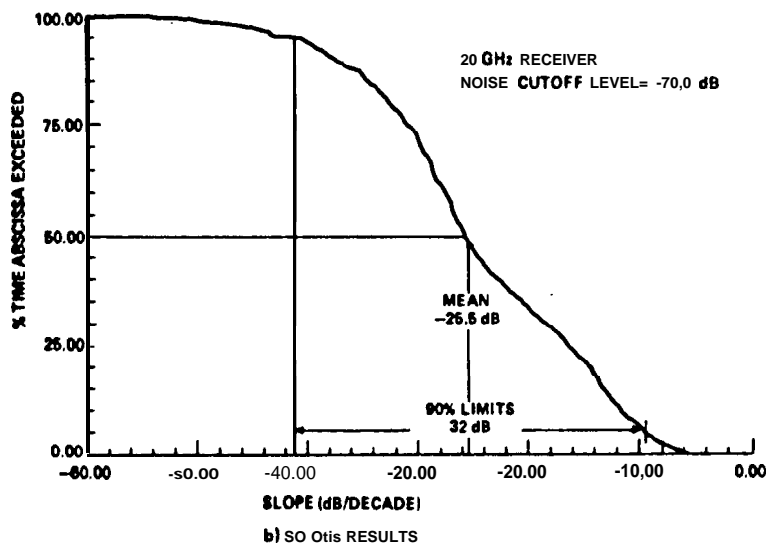
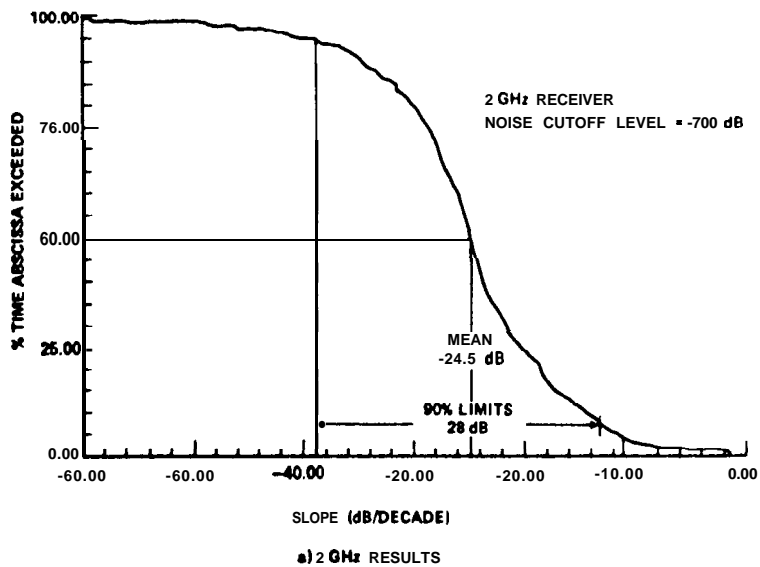


Figure 6.5-5. Probability Density Function of Spectral Slope

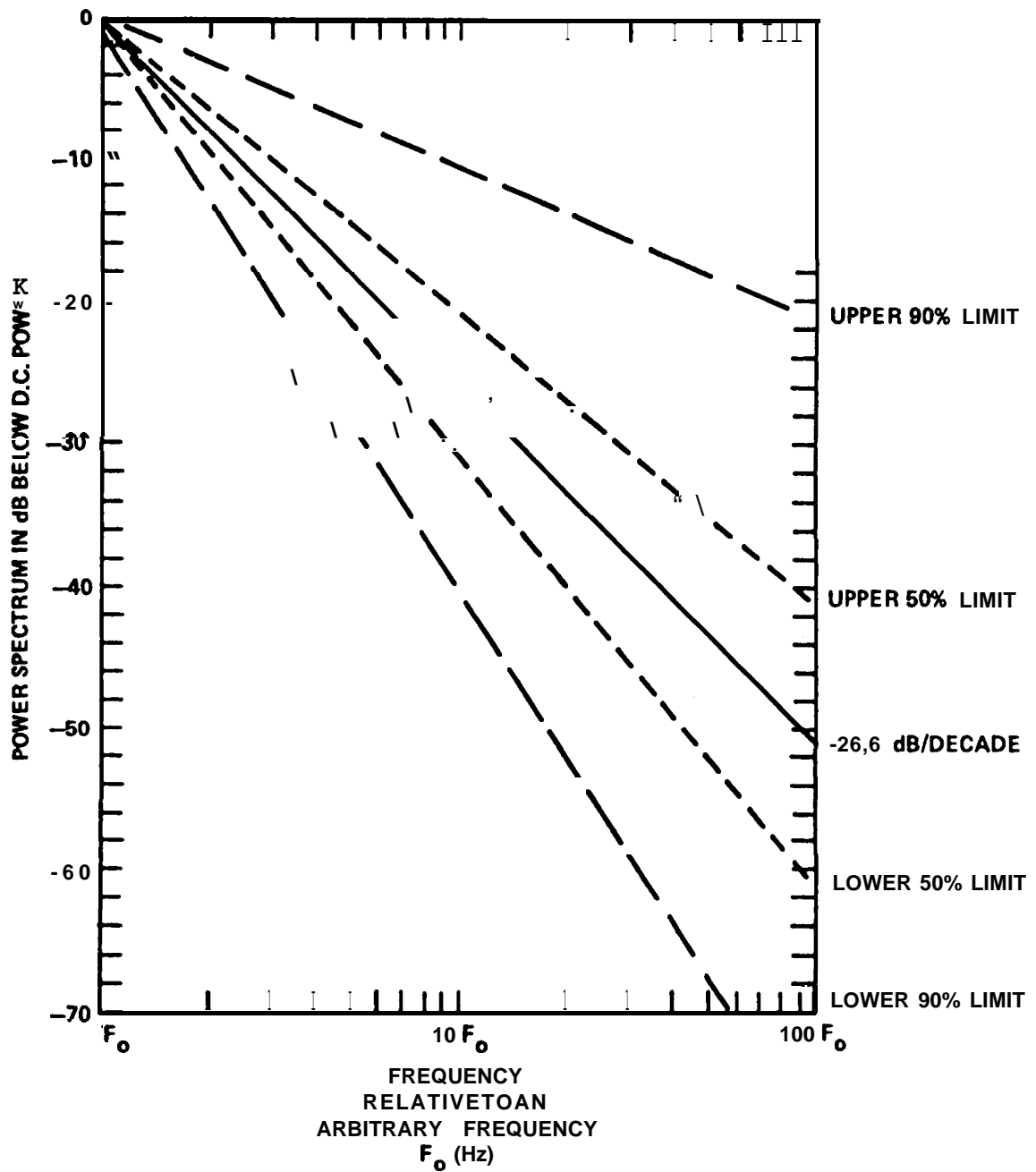


Figure 6.5-6. Confidence Limits of Distribution of Spectral Slope from Average -26dB/Decade

where the constants are the same as those defined for the variance expression, σ^2 . This value for R may then be combined with atmospheric gas loss in order to obtain an estimate of average received signal level for an earth-space path. Figure 6.5-7 presents an example of predicted signal levels for 2, 7.3 and 30 GHz for antenna beam widths of 1.8° , 0.3° , and 0.15° , respectively. Also included are measured signal levels, relative to zenith, from the ATS-6 2 and 30 GHz (Devasirvatham and Hedge-1977) transmissions and TACSATCOM 7.3 GHz (McCormick and Maynard-1972) beacons as the satellites were moving in elevation angle.

6.5.2.3 Low Angle Scintillations/Fading. At low elevations (typically less than 10 degrees) scintillations and fades occur due to refractive effects and multipath effects in the troposphere. In addition for stations utilizing antennas with significant sidelobe levels intercepting the ground, classic multipath is possible and should be considered. However, the effects reported here are generally thought to not include the effects of ground-reflected multipath.

Because no unified theory for low-angle fading exists, the design of future systems must be done by similarity. As more data becomes available and more systems require low elevation angle operation, undoubtedly a low-angle fading theory will be developed.

6.5.2.3.1 Presentation of Selected Experimental Results. Concise summaries of low-angle fading data and long term statistics for a variety of locations is presented in Tables 6.5-1 and 6.5-2, respectively. These results are typical of the magnitude of the effect, however to date no comprehensive model attempts to explain these effects. A typical plot of the signal amplitude variance at 20 and 30 GHz as observed in Columbus, Ohio between 42 and 2 degrees is shown in Figure 6.5-8 (compare with Figure 6.5-2). Because the distribution suggested a cosecant behavior, a minimum **mean-square-error** curve was fit to the data as noted in Figure 6.5-8.

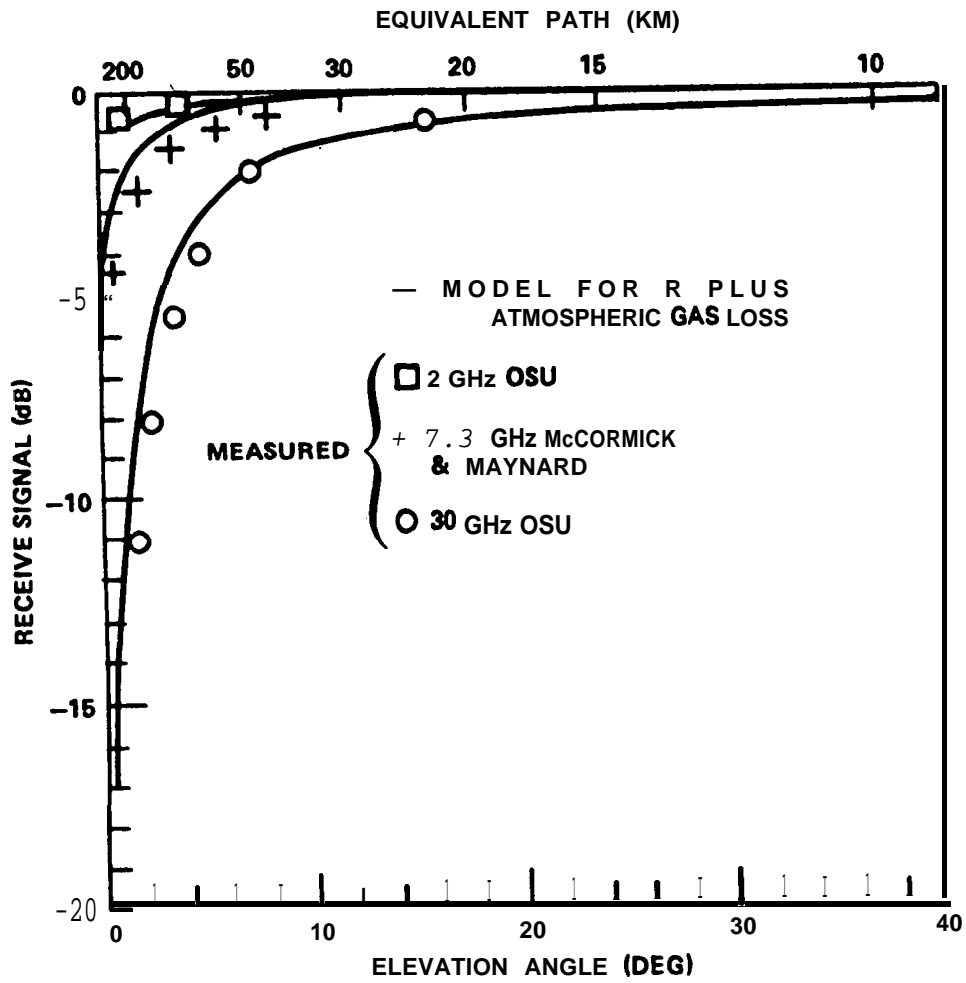


Figure 6.5-7. Predicted and Measured Signal Level as a Function of Elevation Angle

Table 6.5-1. Fading Data Predominantly Due to Scintillation from Satellites at Low Angles of Elevation

[CCIR Report 564-1, 19781

Location	Satellite	θ (degrees)	Fading data
United Kingdom; Martlesham, Suffolk	ATS4 ; 30 GHz	6.5 3.3 2A	6.5 (dB) (peak-to-peak) } Maximum in 10 (dB) (peak-to-peak) } turbulent windy 18 (dB) (peak-to-peak) } conditions
United Kingdom; Birmingham	ATS-6; 30 GHz	0.3-1.2 1-2	Occasional deep fades of 20 dB Slow enhancements and sudden fades of 20 dB
USA ; Virginia [Stutzman <i>et al</i> , 1975]	ATS-6; 20 GHz	9 4.7-5.1 4.5	2-3 dB Before and after light rain 2-7 dB Hazy conditions 8-15 dB Partly cloudy conditions
USA ; Ohio	ATS-6; 2 and 30 GHz	2.8 0.38	3 dB at 2 GHz 15 dB at 30 GHz 7 dB at 2 GHz 20 dB at 30 GHz Maximum effect in cumulus clouds
USA; Massachusetts	IDCSP; 7 GHz	10 3	0.03-0.2 dB r.m.s. 10 dB r.m.s. was observed occasionally in summer. Elevation angle fluctuations of up to 0.01° at 3° elevation and 0.002° at 10° elevation (r.m.s values in 5-min period).
Canada; Eureka [Strickland <i>et al</i> , 1977]	Anik II; 4 and 6 GHz	1	Data similar to the two frequencies. Fades of 11 and 20 dB predicted for 1% and 0.1% of worst month.
United Kingdom; Goonhilly [Harris, 1977]	Indian Ocean Satellite; (INTELSAT IV) 4 and 6 GHz	6.5	3 dB (peak-to-peak) exceeded for 0.3% of time on 4 GHz down-link, in a 9-month continuous measurement.
USA; Maryland [Ippolito, 1976]	ATS-6 ; 20 and 30 GHz	2.5-9	1.5 dB (peak-to-peak) at 19° increasing to 11 dB at 2.5° at 30 GHz. Values at 20 GHz about 40-70% of those at 30 GHz. Occasional deep fades during light rain.

Table 6.5-2. Statistical Fading Data Predominantly Due to Scintillation and Clear Air Low Elevation Angle Fading

[CCIR Report 564-3, 1986b]

Satellite and frequency	Location of measurements	Antenna diameter (m)	Elevation angle	peak-to-dk amplitude exceeded for given percentages (dB)					Period of measurement	Reference
				Whole period			Worst month			
				0.1 %	0.3%	1 %	0.1%	1%		
Intelsat 1 V-A 1.8 GHz	Mu, Finland	3	5.4°	3.7	3.2	2.6	4.2	3.2	May 1977-May 1978	[Allnutt, 1985]
Intelsat 1V-A 1.9 GHz	Dulu, Finland	3	3.5°	3.7	3.2	2.6	4.5	3.3	July 1979-July 1980	[Allnutt, 1985]
Anik-A 1 and 6 GHz	Eureka, Canada	4.6	1°				20	11		[Strickland <i>et al.</i> , 1977]
Intelsat-IV 4 and 6 GHz combined	Goonhilly, United Kingdom (to Bahrain)	30	6.5° (57")	3.7	3	2.6	4	3	9 months	[Harris, 1977]
Intelsat-IV, 4 and 6 GHz combined	Goonhilly United Kingdom Yamaguchi, Japan	27.3	6.5° 9"	4.6	4.3	3.6	6	5.2		
7 GHz	Ottawa, Canada	9.1	1°			15			Summer period	[Webber and McCormick, 1980]
			2-3°			8	-	-		
			5°	5.5	-	2.8	-	-		
OTS 11.8 GHz	Svalbard Norway	3	3.2°				6.5	3.4	April-December 1979 June-August 1980	[Gutteberg, 1981a]
Intelsat-V 11.45 GHz	Chilbolton, United Kingdom	3	8.9°	4	3.4	2.7	-	-	July-September 1983	[Lo <i>et al.</i> , 1984]

68-9

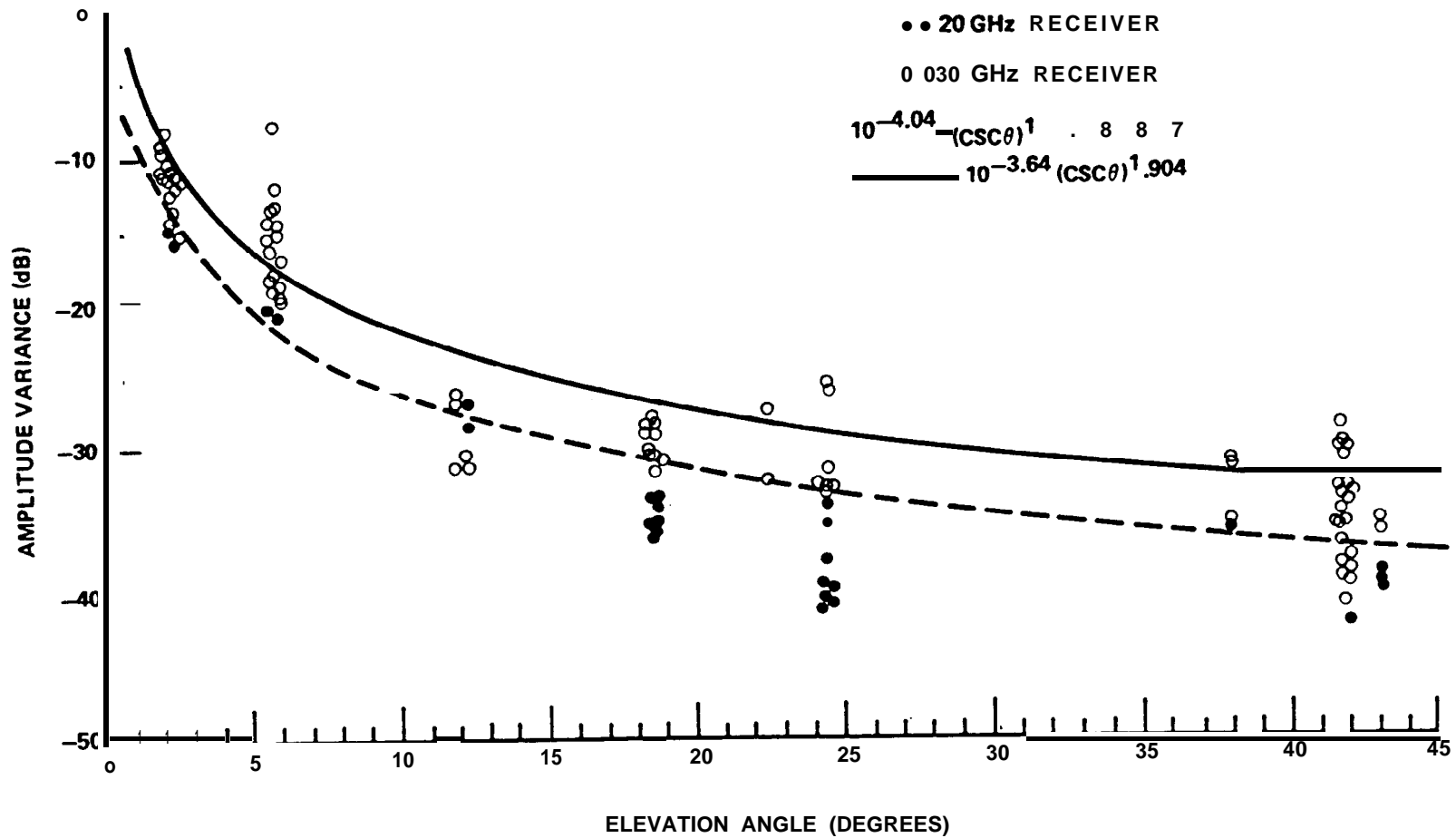


Figure 6.5-8. Measured Amplitude Variance Versus Elevation Angle (Columbus, Ohio)

Experimental measurements of the fade durations at 6 GHz for fades from 0 to 21 dB below the long term median are shown in Figure 6.5.9 (Strickland, et al-1977). These measurements were made at Eureka, Canada during the month of July 1974 when the moisture content (N-value) is above the yearly average, This data is probably typical of continental air mass data. The frequency and elevation angle scaling factors for this data are not thoroughly confirmed, but the Tatarski (1961) model appears to model experimental results (CCIR-1978, Rpt 718). The variance appears to scale proportional to frequency according to the relation:

$$\text{variance} = 42.2 \left(\frac{2\pi}{\lambda} \right)^{15/6} \int C_n^2(p) p^{5/6} dp \quad (6.5-4)$$

where p is the distance along the path.

The cumulative distribution for the rate of change of signal amplitude between 0.4 second samples was found to be identical for positive and negative-going signals (Strickland, et al-1977). The measured distribution is given in Figure 6.5-10, but again the frequency and elevation angle scaling factors are unknown.

6.5.3 Phase Variations

Phase variations arise due to the variable delay as the wave passes through a medium with variable refractivity and also due to wavefront ripple introduced by the "lumpy" medium. The former is termed phase delay fluctuations, while the latter effect is called phase scintillations.

6.5.3.1 Estimation of Phase Delay Fluctuations on Earth-Space Paths.

An expression for the rms phase fluctuation for a finite circular aperture antenna of diameter d_a ,

$$\sigma_\phi = \left(1 - \frac{d_a^2}{4l^2} \right) \left(2L_l \overline{\Delta N^2} \right)^{1/2} \frac{2\pi \times 10^{-6}}{\lambda} \quad (6.5-5)$$

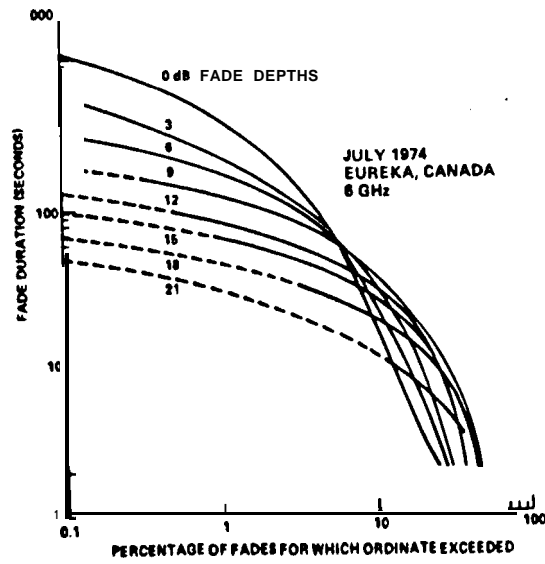


Figure 6.5-9. Cumulative Distributions of Fade Durations at 6 GHz

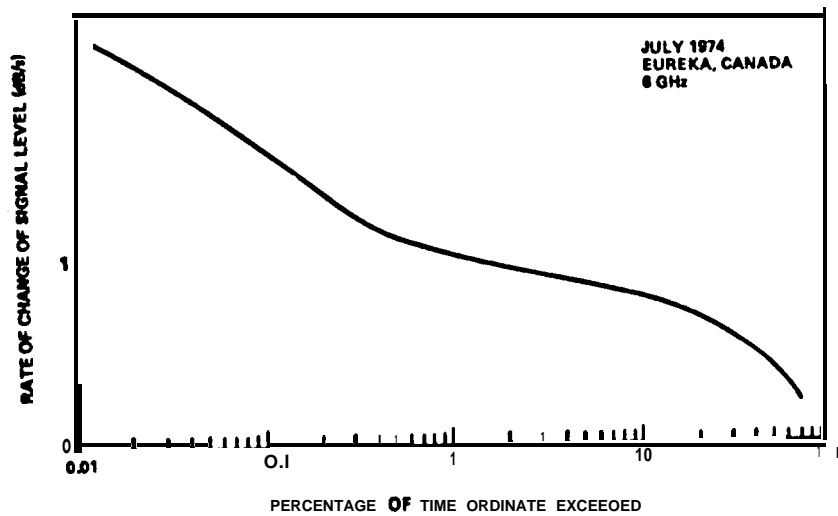


Figure 6.5-10. Cumulative Distribution of Rate of Change of 6 GHz Signal

has been presented by **Muchmore** and Wheelon (1955). The derivation employs a ray theory approach and assumes an exponential spatial correlation for the turbulence scale. θ is in radians, ℓ is the scale length of the turbulent eddy, L_t is the path length through the turbulence, λ is wavelength, and $\overline{\Delta N^2}$ is the mean-square fluctuation in the refractivity N. When using this expression, one should only assume values of ℓ and $\overline{\Delta N^2}$ such that

$$5m \leq \ell \overline{\Delta N^2} \leq 500m. \quad (6.5-6)$$

The results of using this relation at the limiting values of $\ell \overline{\Delta N^2}$ for 3 and 10 GHz are presented in Figure 6.5-11. Typical values of ℓ are 60 meters and $\overline{\Delta N^2} = 1/2$. This **model** indicates that the phase delay fluctuations increase linearly with frequency and become significantly less if the antenna diameter approaches the scale length.

Another technique for estimating these phase delay fluctuations based on the monthly variance of the surface refractivity and estimates of the frequency spectrum of the delay fluctuation have been made by **Nusple**, et al (1975).

6.5.3.2 Estimate of Phase Ripple Effects on Earth-Space Paths.

Accompanying the amplitude scintillations of a plane wave propagating through tropospheric turbulence are transverse phase ripple variations. According to the theory of Tatarski (1961) the mean-square phase variation over a distance transverse to the propagation path is.:

$$D_\theta(\rho_\theta) = K_\theta C_{no}^2 (2\pi/\lambda)^2 L_T \rho_\theta^{5/3} \quad (6.5-7)$$

where λ is wavelength, L_t is the propagation path length through the region of turbulence, and C_{no} is the surface structure constant. The constant K is equal to 2.91 for the exponential C_n^2 model (Tatarski-1961) and equal to 4.57 from Ohio data (**Theobald** and Hedge-1978). This expression may be used to estimate the expected mean-square

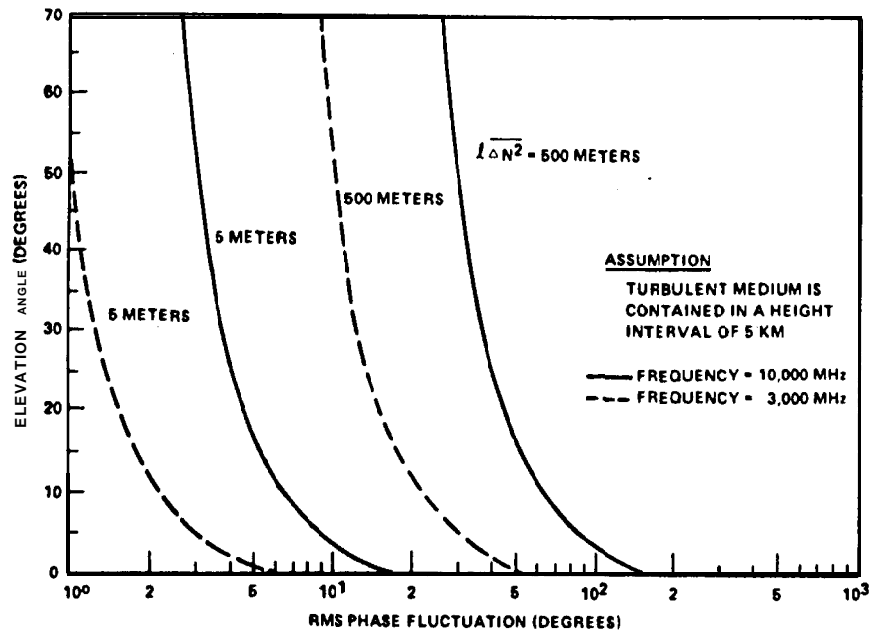


Figure 6.5-11. R.M.S. Phase Fluctuations for an Earth-Space Path

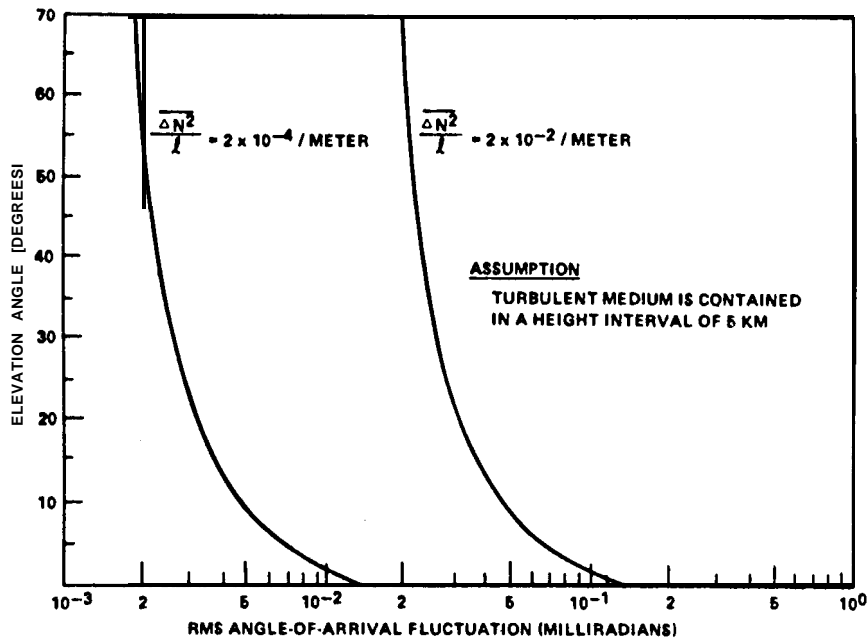


Figure 6.5-12. R.M.S. Angle-of-Arrival Fluctuations for an Earth-Space Path

phase variation between two points separated by a distance $\rho \theta$ normal to the direction of propagation, given an estimate of C_{no} .

Clearly, this phase incoherence appears as an apparent antenna gain degradation. Measurements made with a 22 m diameter antenna at 5 degrees elevation angle and 4 and 6 GHz indicate a 0.2 to 0.4 dB degradation (Yokoi, et al-1970). A 7 meter diameter antenna at 5 degrees elevation angle and 15.5 and 31.6 GHz yielded a gain degradation of 0.3 and 0.6 dB, respectively (Yamada and Yokoi-1974). This effect is clearly most pronounced for large antennas, high frequencies and elevation angles below 5 degrees (CCIR 1986b, Rpt. 564-3) .

6.5.4 Angle-of-Arrival Variation

The average ray bending (mean deviation from the geometric or vacuum line-of-sight) along a slant path has been estimated by a linear relation to the surface refractivity (Crane-1976a). Estimates of the apparent fluctuations of ray direction or the angle-of-arrival are given below. Because they are assumed to arise solely due to refractive effects the variations are symmetrical about the direction of propagation and the fluctuation frequency is of the order of the time for the turbulence length to pass through the beam.

The Muchmore and Wheelon expression for the rms angle-of-arrival fluctuation in radians is

$$\sigma_{\theta} = \left[\frac{2\sqrt{\pi} L_r \overline{\Delta N^2}}{l} \right]^{1/2} \times 10^{-6} \quad (6.5-8)$$

where all parameters are as previously defined. A Gaussian correlation function for the scale of turbulence was assumed and one should impose the limits

$$2 \times 10^{-4} \text{ m}^{-1} \leq \overline{\Delta N^2} / l \leq 2 \times 10^{-2} \text{ m}^{-1} \quad (6.5-9)$$

Figure 6.5-12 is an example for this expression, within the stated range of $\overline{\Delta N^2}/\ell$, for an earth-space propagation path through a turbulent region of height 5 km. Note that σ_θ^2 is directly proportional to path length and independent of operating frequency. Also, σ_θ decreases with increasing eddy size, ℓ , while phase fluctuation σ_θ increases with increasing eddy size.

Estimates (CCIR-1986b, Rpt. 564-3) indicate that the short-term variations in the angle-of-arrival may be of the order of 0.02 degrees (0.37 milliradians) at 1 degree elevation. This is higher than the theory predicts (see Figure 6.5-12), but the effect does decrease rapidly with increasing elevation angle. Crane (1976) reports values of σ_θ within the bounds of Figure 6.5-12 for 7 GHz measurements made at varying elevation angles with a 37 m diameter antenna.

Generally, for beamwidths greater than 0.01 degree and elevation angles above 10 degrees, the angle-of-arrival fluctuations are masked by other fluctuations.

6.5.5 Fading and Gain Degradation Design Information

6.5.5.1 Fade Distribution Function Estimation. The estimates of gain reduction and signal variance parameters, R and S^2 , have been presented. These quantities may be incorporated into distribution functions which are of the form used in link design. They represent the long term average fade statistics due to clear air amplitude and angle-of-arrival fluctuations. The estimates of R and S^2 may be more closely matched to local and seasonal conditions if a local estimate of C_n^2 is available. A hypothetical low elevation angle fade distribution is presented in Figure 6.5-13. The abscissa is referenced to the signal level received in the absence of turbulence, i.e., including free space loss and gaseous absorption. The point at which the signal level is R dB is also the mean of the received signal; thus, one point on the fade distribution is established. The fade distribution for turbulence-induced fluctuations is assumed to be log-normal, with mean and median being

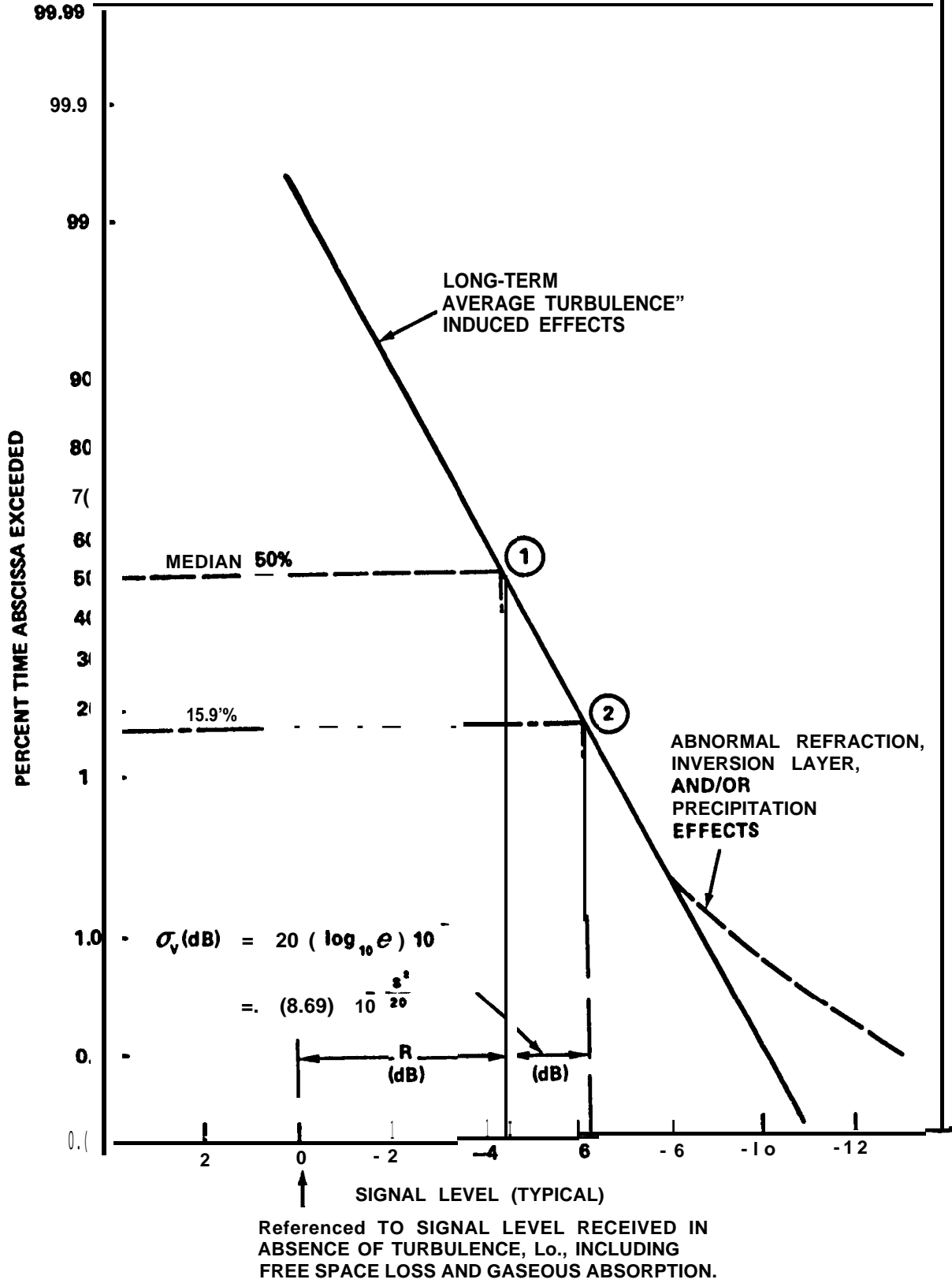


Figure 6.5-13. Hypothetical Fade Distribution Function for Low Elevation Angles

equal. The fade distributions resulting from the Ohio State University ATS-6 30 GHz beacon measurements (Devasirvatham and Hedge-1977) indicate that this log-normal assumption is valid for elevation angles above approximately 2° . A similar observation was made -concerning the 7.3 GHz fade distribution above 4° elevation angle observed by McCormick and Maynard (1972).

A fade distribution may now be produced using this assumption of linearity. Referring to Figure 6.5-13, it was noted that the point at which the received signal level is R dB represents the mean signal level. For a normal distribution, the mean is plotted at the 50% time abscissa exceeded point, indicated by 1 in the figure. One standard deviation to the right of the mean on a normal distribution occurs at the 15.9% time abscissa exceeded level. It may be easily shown that the standard deviation of received signal level, expressed in dB and denoted σ_{vdB} , may be written in terms of the signal variances s^2 . This point, σ_{vdB} , to the right of R , is denoted by 2 in the figure. A straight line drawn between points 1 and 2 now approximately represents the fade distribution, referenced to the mean signal level in the absence of turbulence induced fluctuations. This distribution was based on small fluctuation arguments and should be employed as a lower bound when estimating a particular fade distribution.

Deviation of this fade distribution from the expected form will occur at small time percentages. Additional fading due to precipitation, abnormal refraction, or inversions in the atmosphere will cause greater fade depths for the small time percentages. However, the turbulence effects, which are always present, are still dominant for larger time percentages. For high elevation angles, i.e., short path lengths, s^2 will be very small and the line drawn through points 1 and 2 will be virtually vertical.

However, the precipitation effects at the lower percentages will still be present for short path length cases and will become the dominant feature of the fade distribution.

6.5.5.2 Gain Degradation Design Information.

6.5.5.2.1 Estimation of Domains. The effects of amplitude and angle-of-arrival fluctuations **are, of course,** most prominent for very long path lengths and/or very narrow beamwidths. One may estimate whether or not gain degradation need be considered in a path design if elevation angle (or equivalent path length) and antenna beamwidth are known. Figure 6.5-14 presents regimes of average gain degradation between 0.5 and 3 **dB** and where they must be considered as a function of elevation angle and antenna **beamwidth.**

Realized gain, or expected gain less gain degradation, is plotted as a function of antenna beamwidth (for any frequency) or equivalent aperture diameter at 30 GHz in Figure 6.5-15. All equivalent aperture diameters are presented for an antenna aperture efficiency of 0.6. The curve representing zero path length L_t is simply the common gain approximation $G = 41253/B^2$ where B is the half power **beamwidth in degrees.** Realized gain curves for path lengths of 50 to 300 **km are** plotted using the model. Equivalent" earth-space path elevation **angles** assuming a 6 km high homogeneous atmosphere are presented in parentheses.

Notice that gain degradation due to turbulence-induced fluctuation is negligible for beamwidths wider than about 0.7° for all path lengths. Degradation effects then gradually increase as beamwidth narrows from 0.7° to 0.05° and at any particular beamwidth are approximately directly proportional, in **dB,** to path length. As beamwidth narrows beyond 0.05° , a saturation effect occurs and the degradation becomes constant for any one path length.

All design figures of Section 6.5.5 represent estimates for clear air effects in a temperate climate during daytime and in the warmer months of the year. If a local value of C^2_n is known, more accurate values of R and S^2 may be obtained. If local statistics of C^2_n are known, statistics of R and S^2 may be obtained.

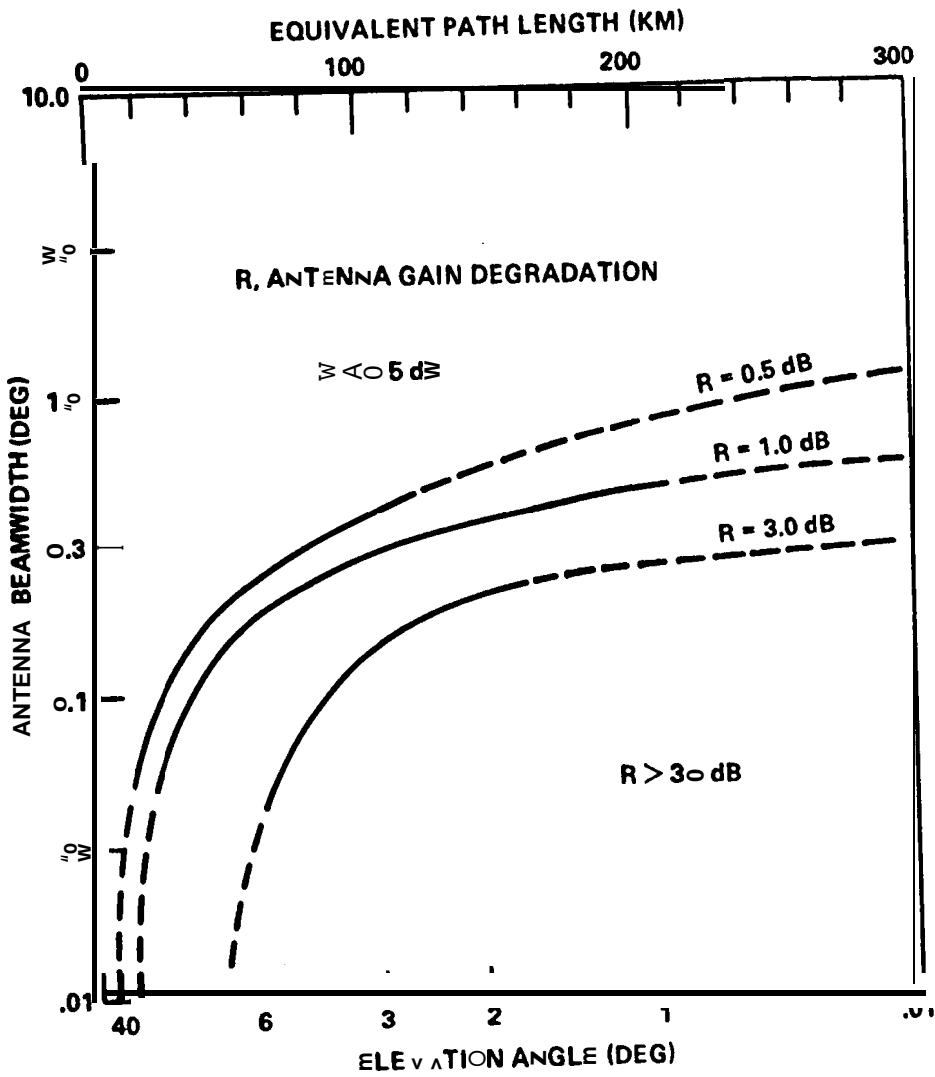


Figure 6.5-14. Gain Degradation Regimes as a Function of Beamwidth and Elevation Angle

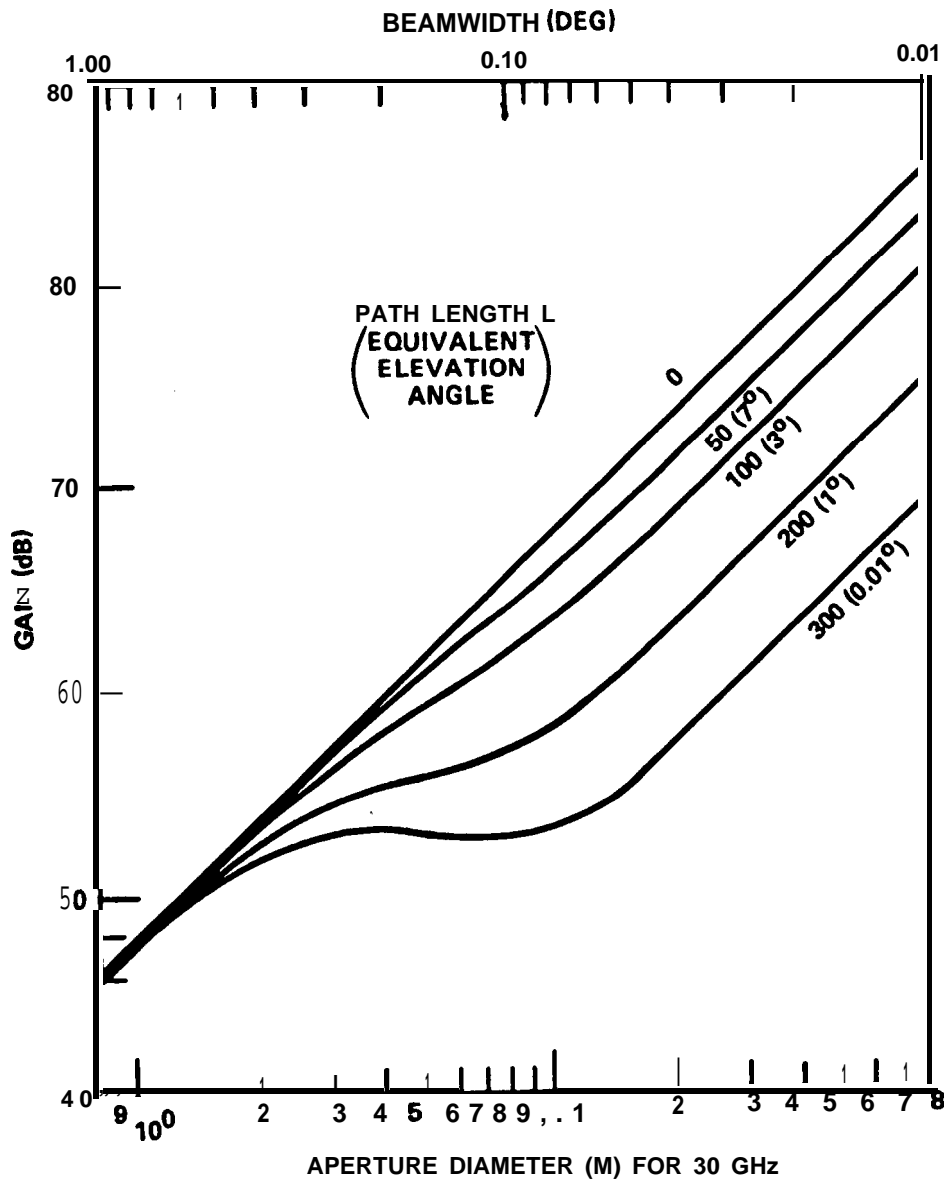


Figure 6.5-15. Realized Gain Versus Beamwidth or Aperture Diameter at 30 GHz

6.5.5.2.2 Spatial Diversity. Paths operating at very low elevation angles with narrow beamwidth antennas may experience unacceptable fading due to scintillation and **multipath** effects. The required reliability may be regained by the use of spaced site diversity. A site separation greater than 300 m transverse to the propagation path has been suggested (**CCIR-1986b**, Rpt 564-3) as necessary to alleviate severe turbulence-induced effects. In effect, separation on the order of or larger than the scale size of the largest inhomogeneities in refractive index along the propagation path, and especially near the surface where refraction is **greatest**, results in decorrelation of the instantaneous signal fluctuations and hence improved performance.

The aperture effects of large antennas may be circumvented if several phase-locked antennas, each with relatively wide **beamwidth**, are employed in an array to achieve the desired system gain. Of course, overall fade margins will be on the order of that for a single element, but angle-of-arrival effects are eliminated. In addition, such an array alleviates the need to mechanically track a geosynchronous satellite, as is necessary with large aperture, narrow beamwidth antennas.

6.5.6 A Sample Computation of Signal Fluctuations and Gain Degradation

In this section examples of the parameters described in Section 6.5 are worked out for a hypothetical ground station located at Columbus, Ohio with a 4.6m (15 ft) diameter parabolic antenna observing a 28.56 GHz **COMSTAR** beacon at 10 degrees elevation angle. Actually, the **COMSTAR** satellites are not at that low an angle, but in order to demonstrate the effects of gain reduction this value has been arbitrarily selected.

6.5.6.1 Amplitude Fluctuations. The variance of the received signal amplitude is calculated using the expression in Section 6.5.2.2. The full half-power beamwidth B in degrees is $70\lambda / d_a = 70 c / f d_a = (70)(3 \times 10^8 \text{m/sec}) / (28.56 \times 10^9 \text{sec}^{-1})(4.6 \text{m}) = 0.16$ degrees. The

path length of the turbulence L_t is computed from $h_t = 6$ km, $r_e = 6371$ km and $\theta = 10$ degrees using the equation

$$L_t = \left[h_t^2 + 2r_e h_t + (r_e \sin \theta)^2 \right]^{1/2} - r_e \sin \theta = 34 \text{ km} \quad (6.5-10)$$

The other constants are:

$$L_0 = 180 \text{ km}$$

$$\delta^2_1 = 1.18 \times 10^{-3}$$

$$\delta^2_2 = 8.35 \times 10^{-4}$$

$$I_i = 0.17$$

$$I_c = 0.83$$

and the signal variance relative to the average power is

$$S^2 = 10 \log_{10} \frac{9.79 \times 10^{-7} + 0.143}{0.83 + 0.14} - 0.14297$$

$$= 10 \log_{10} (2.03 \times 10^{-3}) \approx -27 \text{ dB}$$

Note that this agrees well with the results in Figure 6.5-2. Reference to Tatarski (1961) would have allowed evaluation in terms of C^2_n rather than the formulation by Theobald and Hedge (1978) utilized here.

Reference to Figure 6.5-4b indicates that 50% of the time the S^2 would be between -24 and -30 dB, while 90% of the time S^2 would be between -20 and -34 dB.

The power spectrum density of the fluctuations decreases at 26.5 dB/decade (see Figure 6.5-6). If one considers some lower - frequency cutoff for the amplitude fluctuations (say 0.1 Hz) the

fluctuation power at 1 Hz is on the average 26.5 dB below the value of 0.1 Hz. Only 10% of the time will the 1 Hz fluctuation power be only 10 dB below the 0.1 Hz fluctuation power. **Clearly**, most of the fluctuation power for clear air fluctuations is at the low frequencies (less than 1 Hz).

6.5.6.2 Phase and Angle-Of-Arrival Variations. Phase fluctuations are estimated from the model of **Muchmore** and **Wheelon** (1955) presented in Section 6.5.3. Data quoted in **Muchmore** and **Wheelon** indicate typical values for $\ell \approx 60\text{m} \approx 200$ feet and $\overline{\Delta N^2} = 1/2$. Thus $\ell \overline{\Delta N^2} = 30$ meters.

For a finite circular antenna of 4.6 m diameter, the rms phase delay fluctuation is 0.85 radians = 48 degrees. For a $C_{no} = 10^{-14}$, the phase ripple fluctuation across the antenna is very small.

The estimate of the angle-of-arrival fluctuations in radians (see Section 6.5.4) is calculated to be 3.2×10^{-5} radians = 1.8×10^{-3} degrees. This is a small number compared to 0.16 degree half-power beamwidth of the antenna. Also note that the limits on $\Delta N^2/\ell = 8.3 \times 10^{-3}\text{m}^{-1}$ are not exceeded.

6.5.6.3 Prediction of the Average Received Signal Gain Reduction. The average received signal reduction is calculated using the same parameters required for calculation of the amplitude fluctuations. Using the relation in Section 6.5.2.2.4.

$$R = 10 \log_{10} \frac{(0.83 + 0.17(0.84))}{1.0} = -0.12 \text{ dB}$$

Thus during clear weather this **COMSTAR** beacon will on the average be 0.12 dB below the value calculated considering clear air attenuation only. This same value could be estimated from Figure 6.5-15.

The long-term average distribution in Figure 6.5-13 is now constructed from R and s^2 . The point 2 (15.9% point) is found to be $20(\log_{10}e) 10^{-|s^2|/20} = 0.39 \text{ dB}$ which is the Standard deviation of the receiver voltage taken from a square law detector.

6.6 PREDICTION OF DEPOLARIZATION ON EARTH-SPACE PATHS

6.6.1 Introduction

Depolarization refers to that effect wherein an earth-space wave's polarization is altered in the troposphere. Depolarization is also referred to as cross-polarization. For linearly polarized waves a vertically (horizontally) polarized wave will, after passing through a medium, have a horizontally (vertically) polarized component in addition to the initial wave. For circularly polarized waves a RHCP (**LHCP**) wave will develop into an elliptical wave. For frequency reuse systems based on polarization isolation this coupling reduces isolation and increases "cross-talk."

6.6.1.1 Sources of Depolarization. The **major** source of depolarization at frequencies below 10 GHz is Faraday rotation of the plane of polarization by the Earth's ionosphere. Faraday rotation may be as much as 1° of rotation at 10 GHz. It **is** discussed in a companion publication of propagation effects at frequencies below 10GHz (Flock, 1987).

At frequencies above 10 GHz, the primary sources of depolarization are tropospheric and are due to the presence of

- . hydrometers (rain, ice, snow)
- multipath
- refractive effects

These hydrometer and scattering effects generate depolarization because of the non-spherical shapes of the hydrometer particles. For example, as raindrop sizes increase their shape departs from spherical and **becomes an oblate** spheroid with an increasingly . pronounced flat bottom. For large drop sizes a concave depression

develops (Pruppacher and Pitter-1971). Polarized microwave energy scattered from these particles can easily be converted into an orthogonal polarization.

6.6.1.2 Measures of Depolarization. The measurement of depolarization by propagation researchers usually has been done utilizing orthogonally-polarized feeds on a single antenna while observing singly-polarized satellite signals. This parameter is called the cross-polarization discrimination (**XPD**) or **cross-polarization ratio (XPR)** defined as (**Bostian, et al-1977**)

$$\begin{aligned} \text{XPD} &= \frac{\text{power output from co-polarized port}}{\text{power output from cross-polarized port}} \\ &= (\text{XPR})^{-1} \end{aligned}$$

For perfect transmitting and receiving antennas and a perfect medium this isolation could become, infinite, but with practical components some leakage is always present. Definitions and sample calculations of depolarization terms have been well documented in a tutorial report by **Stutzman (1977)**.

Unfortunately, the system designer desires the cross-polarization isolation (**XPI**) term defined as

$$\begin{aligned} \text{XPI (dB)} &= \text{co-polarized signal power (dB)} \\ &\quad - \text{cross-polarized signal power (dB) on the same channel} \end{aligned}$$

Fortunately, for most levels of attenuation observed, $\text{XPI} \approx \text{XPD} = (\text{XPR})^{-1}$ (**Watson and Arbabi-1973**).

6.6.1.3 Depolarization Measurements. Most experimental depolarization data has been obtained from the 11.7 GHz right-hand circularly polarized Communications Technology Satellite (**CTS**) beacon, the 19.04 and 28.56 GHz linear polarized AT&T **COMSTAR** satellite beacons, and the 11.6 GHz circularly polarized **SIRIO** beacon.

6.6.2 Rain Depolarization

6.6.2.1 Depolarization Versus Attenuation Relations. Correlation of depolarization with rain rate has not been too successful because of the many parameters required for these calculations. However, experimentally and analytically (Nowland, et al-1977a) it has been observed that rain-induced depolarization can be related to total attenuation by the formula

$$XPD = \tilde{a} - \tilde{b} \log_{10} (A) \quad (6*6-1)$$

where XPD is the cross-polarization discrimination in dB and A is the "total attenuation in dB due to rain (not including the clear air attenuation) . \tilde{a} and \tilde{b} are empirical constants.

6.6.2.1.1 CCIR Approximation. The CCIR (1986b, Rpt. 564-3) has developed analytical approximations for the empirical constants \tilde{a} and \tilde{b} which give reasonable agreement for the XPD with existing theory and available data. The relationships are,

$$\begin{aligned} \tilde{a} = & 30 \log(f) - 10 \log_{10} [0.516 - 0.484 \cos(4\tau)] \\ & - 40 \log_{10}(\cos\theta) + 0.00520^2 \end{aligned} \quad (6.6-2)$$

and

$$\begin{aligned} \tilde{b} = & 20 \quad \text{for } 8 \leq f \leq 15 \text{ GHz} \\ & = 23 \quad \text{for } 15 < f \leq 35 \text{ GHz} \end{aligned} \quad (6.6-3)$$

where:

f = frequency, in GHz

τ = polarization tilt angle with respect to the horizontal, in degrees ($\tau = 45^\circ$ for circular polarization)

e = path elevation angle, in degrees

σ = standard deviation of the raindrop canting angle, in degrees

The above relationships are valid over the ranges:

$$8 \leq f \leq 35 \text{ GHz}$$

$$\theta \leq 60^\circ$$

$$0^\circ \leq \tau \leq 90^\circ$$

Recommended values for the standard deviation σ are:

<u>Percent of Time</u>	<u>u</u>
1.0%	0°
0.1%	50
001%	10"
0.001%	15°

The above results do not include the effects of ice depolarization. A CCIR factor for ice induced XPD is discussed later in Section 6.6.3.3.

6.6.2.1.2 VPI & SU and Univ. of Texas Results. The Virginia Polytechnic Institute and State University (**VPI&SU**) have analyzed their CTS (11.7 GHz) and **COMSTAR** (16.04 and 28.56 GHz) beacon depolarization data in two manners. The first technique is to compare the measured cumulative XPD with the measured cumulative rain attenuation statistics. These results are termed the statistical depolarization results. The second technique pairs "instantaneous" (half-minute) intervals of data for both parameters and smooths the data to obtain \tilde{a} and \tilde{b} .

The results of these two techniques for 11.7 GHz data both from **VPI&SU** and the University of Texas (**C.W. Bostian, et al-1979**) are shown in Figure 6.6-1. Clearly these results indicate a wide spread of values have been obtained to date even though they are averaged over an entire year. The attenuation has been truncated at 5 **dB** because of the effects of ice depolarization (see Section 6.6.3).

VPI&SU has also related the XPD to attenuation for each month of 1978 for which 5 **dB** or greater fades occurred. These \tilde{a} and \tilde{b} results are shown in Table 6.6-1 for the number of half-minute samples indicated. The R^2 term, a correlation coefficient, is a measure of the goodness of the fit. The wide variations noted are **simalar** to those observed by other investigators.

Additional data from the University of Texas at Austin (Vogel - 1979) incorporating exceedance values is presented in Figure 6.6-2. These curves show the 10%, 50% (median) and 90% expectation of exceeded isolation for each attenuation. For example at 5 **dB** (meaning $4 \text{ dB} \leq A \leq 5 \text{ dB}$) the XPD exceeded 23 **dB** for 90%, exceeded 28 **dB** for 50% and exceeded 33 **dB** for 10% of the data. The logarithmic fit to these three curves is

$$\begin{aligned}
 10\% & : \text{XPD} - 42.9 - 17.5 \log_{10}A \\
 50\% & : \text{XPD} - 35.8 - 13.4 \log_{10}A \\
 90\% & : \text{XPD} - 31.5 - 12.6 \log_{10}A
 \end{aligned}$$

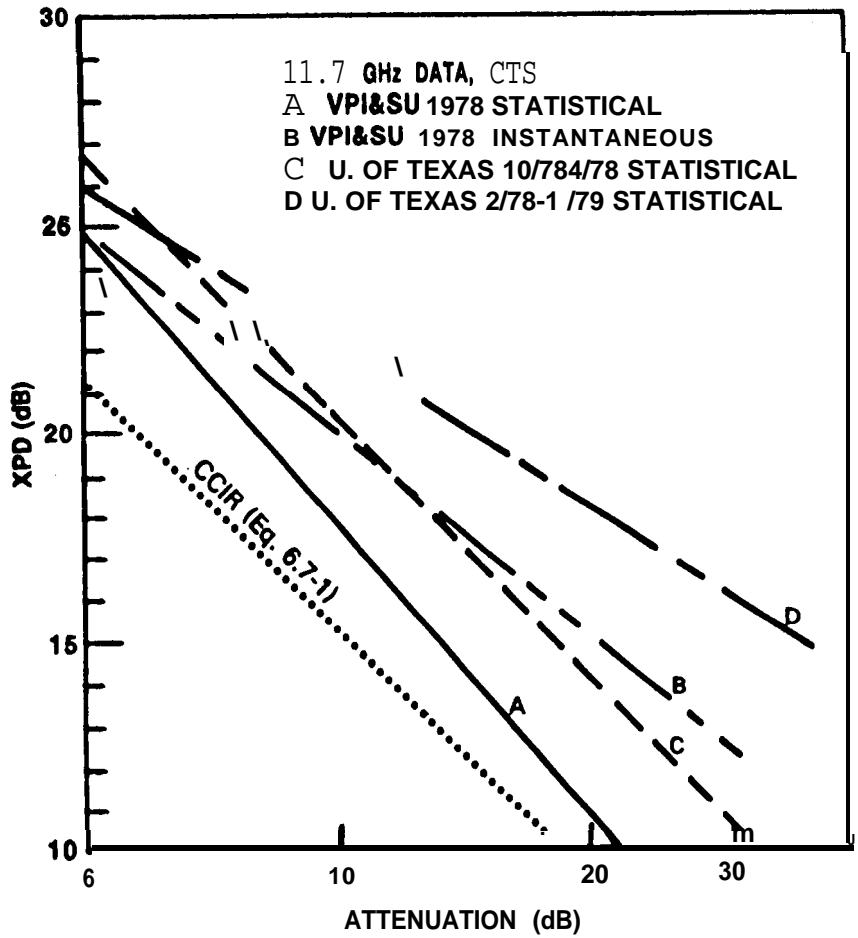


Figure 6.6-1. Cross-Polarization Discrimination Versus Attenuation for Statistical and Instantaneous Data

Table 6.6-1. Least-Mean Square Fits of Depolarization Coefficients by Month

XPD = $\tilde{a} - \tilde{b} \log_{10} A$		5 < A < 30 dB		VPI&SU 1978 CTS DATA
MONTH	\tilde{a}	\tilde{b}	R2	NO. OF 1/2 MINUTE INTERVALS
JAN	30.79	2.62	.00	22
MAR	51.18	36.18	.83	309
MAY	49.01	27.93	.90	30
JUNE	38.42	17.53	.56	38
JULY	42.23	21.94	.80	74
AUG	47.31	25.99	.47	28
SEPT	64.20	51.93	.32	60
NOV	27.59	4.11	.04	7
YEAR	36.29	16.22	.36	574

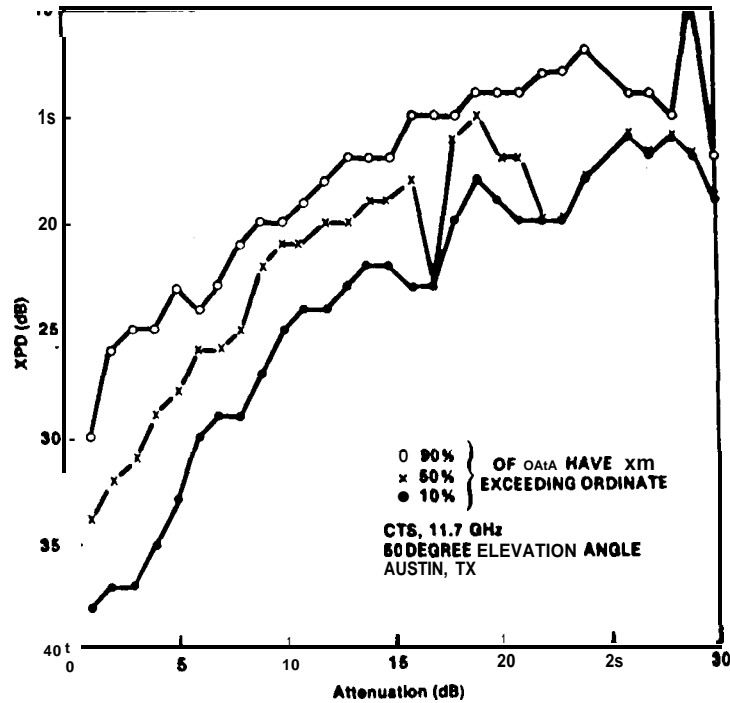


Figure 6.6-2. Twelve Month Isolation Versus attenuation Data

for the 11.7 GHz CTS beacon at 50 degrees elevation angle.

6.6.2.2 Frequency Scaling Depolarization Measurements. The Virginia Polytechnic Institute and State University (Bostian, et al-1978, 1979) has also made simultaneous measurements of the depolarization at 19 GHz vertical and horizontal and 28.56 GHz using the COMSTAR beacons. Their results for 1977 and 1978 are given in Table 6.6-2.

Table 6.6-2. Cross-Polarization Discrimination Versus Attenuation (Least-Mean-Square Fits)

Blacksburg, VA		Elevation Angle = θ
Period	Frequency/Polarization	$XPD = \tilde{a} - \tilde{b} \log_{10}(A)$
Aug 1977	11 GHz, RHCP (CTS, $\theta = 33^\circ$)	$XPD = 44.7 - 22.6 \log_{10}(A)$
1978	11 GHz, RHCP (CTS)	$XPD = 36.3 - 16.2 \log_{10}(A)$
Aug 1977	19 GHz, vertical (COMSTAR, $\theta = 44^\circ$)	$XPD = 47 - 24.5 \log_{10}(A)$
Sept 1977	19 GHz, horizontal (COMSTAR)	$XPD = 37.1 - 20.0 \log_{10}(A)$
1978	19 GHz, vertical (COMSTAR)	$XPD = 43.9 - 16.6 \log_{10}(A)$
Aug 1977	28 GHz, vertical (COMSTAR)	$XPD = 36.4 - 15.4 \log_{10}(A)$
1978	28 GHz, vertical (COMSTAR)	$XPD = 31.2 - 7 \log_{10}(A)$

The analysis of Nowland, et al (1977a) may be utilized to show the expected frequency dependence of the coefficients \tilde{a} and \tilde{b} in $XPD = \tilde{a} - \tilde{b} \log_{10}(A)$. Using Equations 11 and 12 of Nowland, et al (1977a) and many of the constants in the paper, the solid curve was derived in Figure 6.6-3. The dashed curve was derived using the effective path length $L_e = 12.82R^{-0.3}$ and the specific attenuation in Section 6.3. Several experimental data points are shown, but

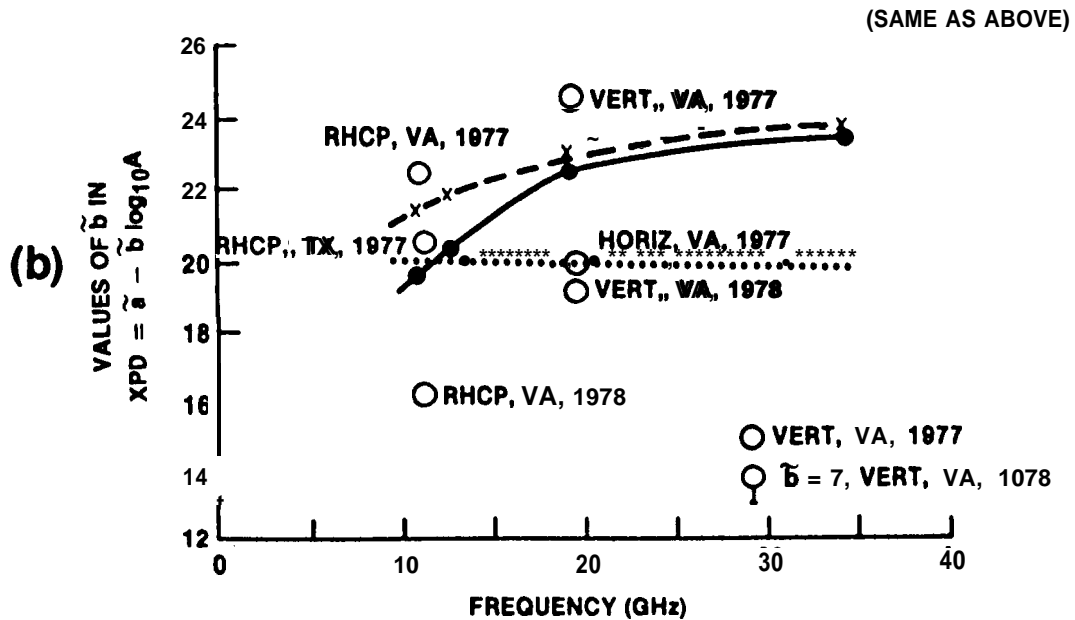
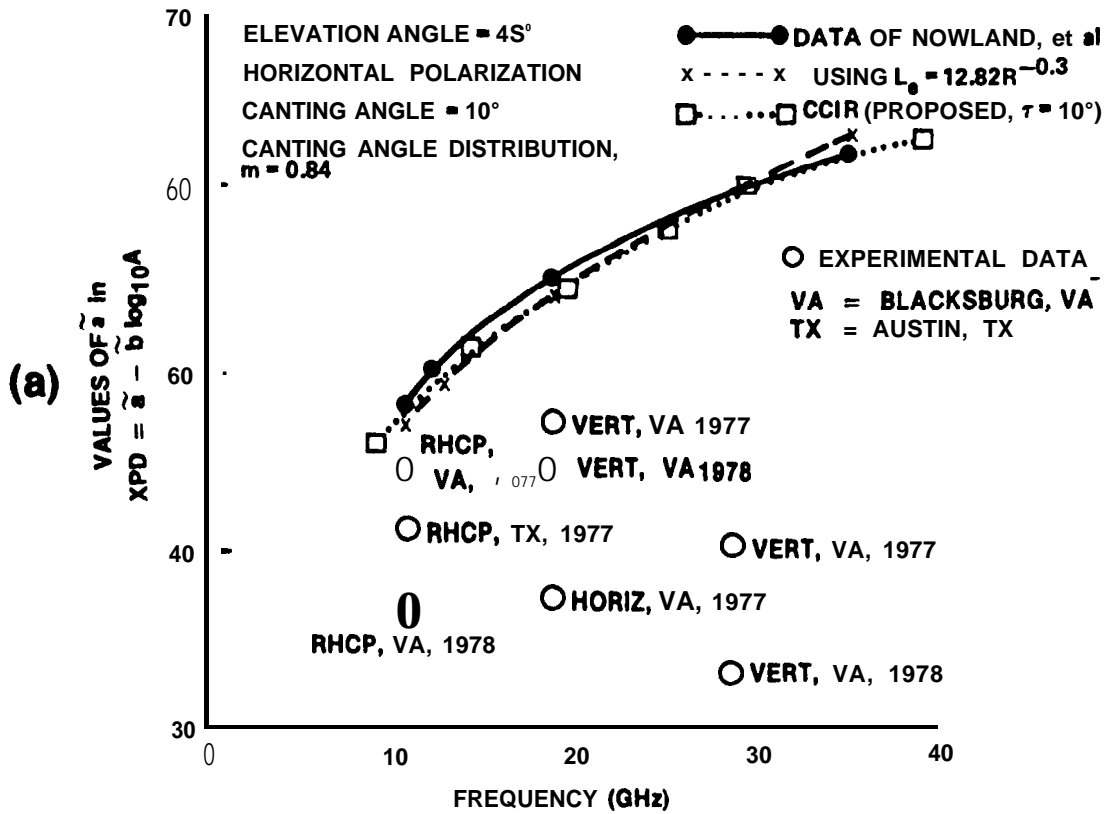


Figure 6.6-3. Frequency Dependence of the Coefficients in the Cross-Polarization Discrimination Relation

these do not correlate well with the theory (possibly because of the polarization dependence of \tilde{a}). The important results of these figures are that \tilde{a} increases with increasing frequency, while \tilde{b} appears to be relatively constant. In the relation $XPD = \tilde{a} - \tilde{b} \log_{10}(A)$ this would imply that the XPD increases with increasing frequency, but because of the rapid increase in A with frequency, XPD will actually decrease for increasing frequency and moderate rain rates.

Chu (1980) has found linear relations between the XPD and frequency throughout the 10 to 30 GHz frequency range. Specifically, XPD (expressed as a numerical ratio) is directly proportional to frequency for a fixed rain rate, and is inversely proportional to frequency for a fixed value of rain attenuation. Bostian (1979b) confirms this linear relation between the XPD (f_1) and XPD(f_2) from his monthly COMSTAR data for 1978, but, the value XPD(f_2)/XPD(f_1) varies from month to month.

6.6.2.3 Elevation Angle Dependence of Depolarization. In the U.S. and Canada depolarization measurements have been obtained at elevation angles from 10.7° in Blacksburg, VA (Bostian, et al-1986) to 49° at Austin, Texas (Vogel-1978). The general dependence of XPD versus A on elevation angle θ can be obtained from the theoretical results of Nowland, et al (1977a). Note that both the coefficient a and the total attenuation A depend on elevation angle.

The elevation angle dependent results of Nowland, et al (1977b) 11.7 GHz (experimental data) are shown in Figure 6.6-4. Clearly the a coefficient is elevation angle dependent, however the experimental data does not confirm this fact. The b coefficient appears to be nearly independent of elevation angle and does appear to agree with the limited data base.

Chu (1980) has observed that the differential propagation constant for depolarization is governed by a $\cos^2\theta$ relation.

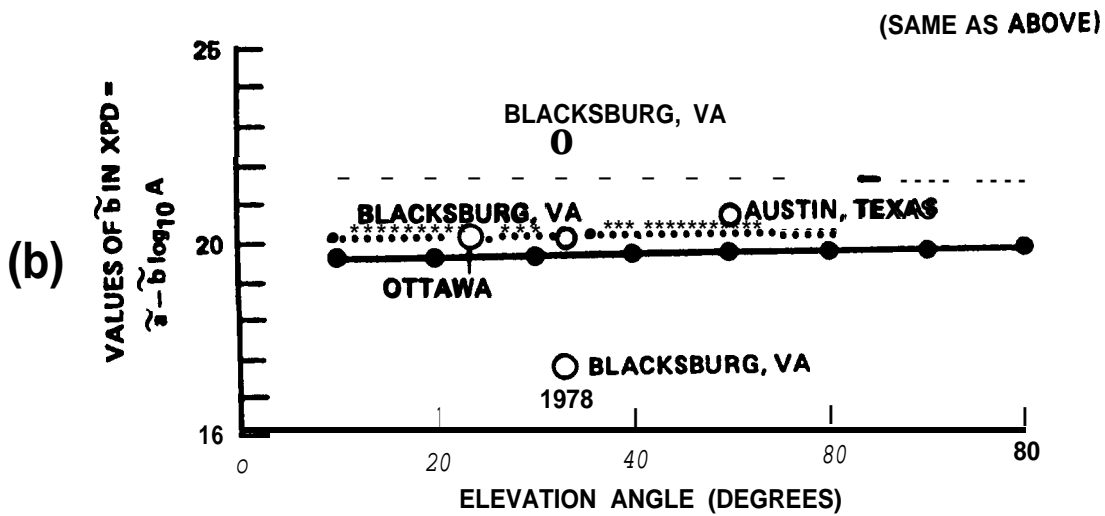
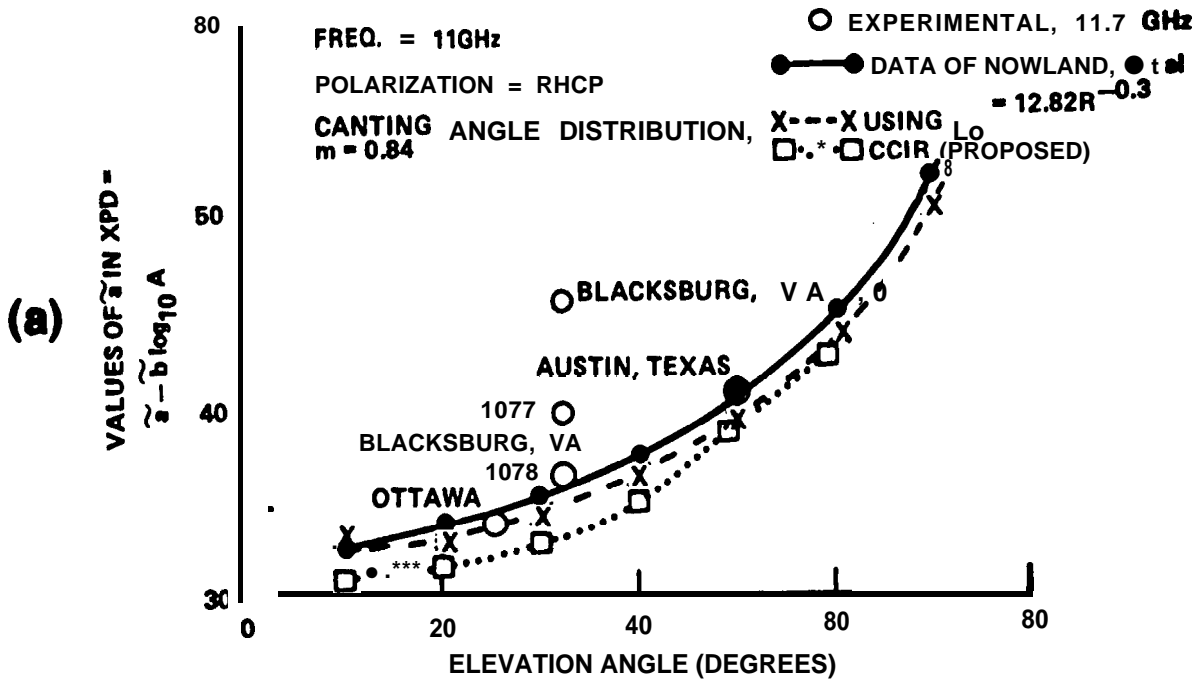


Figure 6.6-4. Elevation Angle Dependence of the Coefficients in the Cross-Polarization Discrimination Relation

However the XPD dependence on elevation angle must 'also take the effective path length effect into account (Chu-1974).

6.6.2.4 Phase Variations During Rain-Induced Depolarization Events.

At **Blacksburg, VA (Bostian, et al-1977)** measurements have been made of the phase difference between the co-polarized signal components. This phase difference has been observed to both decrease and increase by about 150 degrees for 3 dB fades and then not change significantly for higher attenuations: The phase difference has also been observed to increase and then decrease in the same storm. The mechanism for this plateau at 150 degrees and why the sign changes remains unexplained.

6.6.3 Ice-Crystal Depolarization

6.6.3.1 Meteorological Presence of Ice. Ice crystals form around dust particles in shapes influenced by the ambient temperature. In cirrus clouds they may exist for an indefinite time, but in cumulonimbus clouds they follow a cycle of growth by sublimation, falling and melting in the lower reaches of the cloud (**Bostian and Allnutt-1971b**) . Radio, radar and optical observations all confirm that cloud ice crystals possess some degree of preferred orientation related to the orientation of the electrostatic field. The crystals range in size from 0.1 to 1 mm and concentrations range from 10^3 to 10^6 crystals/m³. The variation in concentration and occurrence of events may be due to the variation of "seed" nuclei in various air masses. For example continental air masses contain more dust nuclei than maritime air masses and so occurrences of ice-crystal depolarization occur more frequently at inland ground stations. This general trend has been observed between observations at the Virginia Polytechnic Institute and State University (inland, most frequent), University of Texas at Austin (intermediate) and Bell Telephone Laboratories (maritime, least frequent).

6.6.3.2 Ice-Crystal Depolarization Measurements. Ice particles well above the height of the melting layer may have significant cross-polarization effects even for small values of attenuation

(typically below 3 to 5 **dB** at 11.7 **GHz**). This effect is believed to contribute to the poor correlation between the excess attenuation and the cross-polarization discrimination at these low values of attenuation.

In Austin, TX (Vogel-1978, 1979) ice depolarization was associated with either thunderstorms during the summer months or with clouds in the presence of polar air masses during the winter. An example of the percentage of time that XPD was less than or equal to the abscissa given that the excess attenuation was less than or equal to 1 **dB** is shown for the 18 month period from 12 June 1976 to 31 January 1978 and the period February 1978 to January 1979 in Figure 6.6-5. This curve shows that during 1976-78 45 per cent of the time that the XPD was less than or equal to 35 **dB**, there was less than 1 **dB** of attenuation; 24 per cent of the time that the XPD = 30 **dB** the A = 1 **dB** and 12 per cent of the time that XPD = 25 **dB** the A ; 1 **dB**. In contrast, using the rain depolarization relation for 1 **dB** yields XPD = 40 **dB**. Therefore systems requiring 30 **dB** or more XPD should expect a significant number of depolarization events due to ice.

Also, it has been observed (Shutie, et al-1978) that at 30 **GHz** ice crystals yield a constant value (typically 90 degrees) of the relative phase angle between the **crosspolar** and **copolar** signals as a function of XPD as shown in Figure 6.6-6. The corresponding polar plot for a heavy rain event is shown in Figure 6.6-7. In this case the XPD was reduced by signal attenuation and the signal to noise ratio of the relative phase measurement decreased as the XPD decreased. This effect appears to increase the scatter of the phase angle with decrease in XPD.

English investigators have also noted that rapid changes in relative phase and XPD are observed *in* thunderstorms and are associated with realignment of the ice crystal orientation by the electrostatic fields. In electrically-active **storms**, these

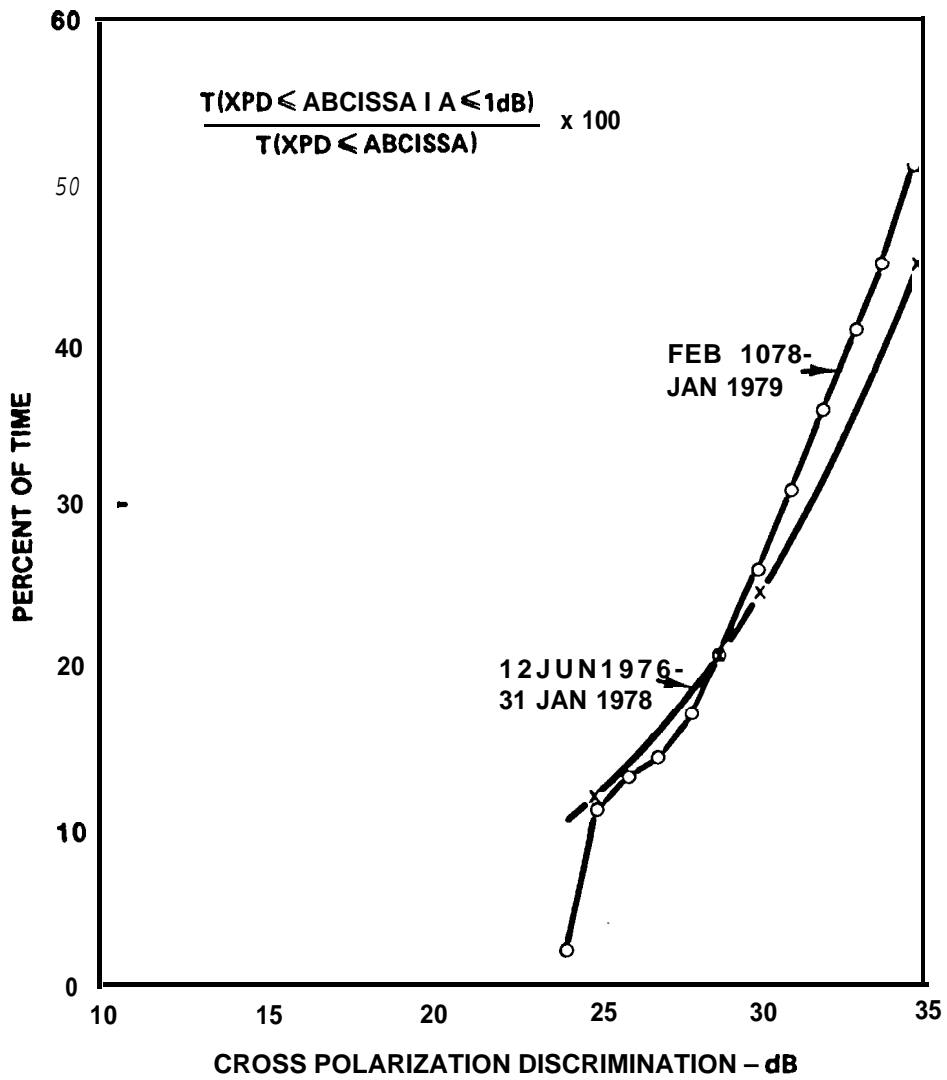


Figure 6.6-5. Contribution of Ice Depolarization to all Depolarization Events

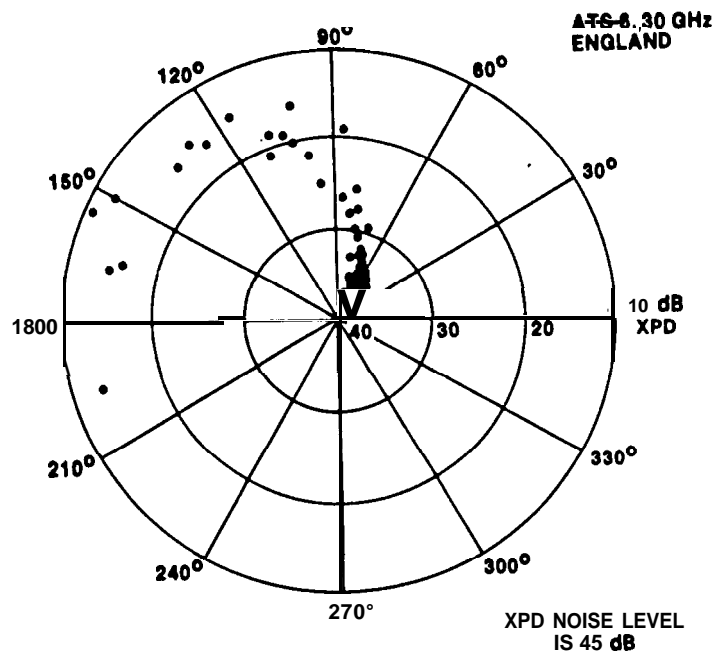


Figure 6.6-6. Polar Plot of the Cross Polarization Discrimination Arising from an Ice Cloud

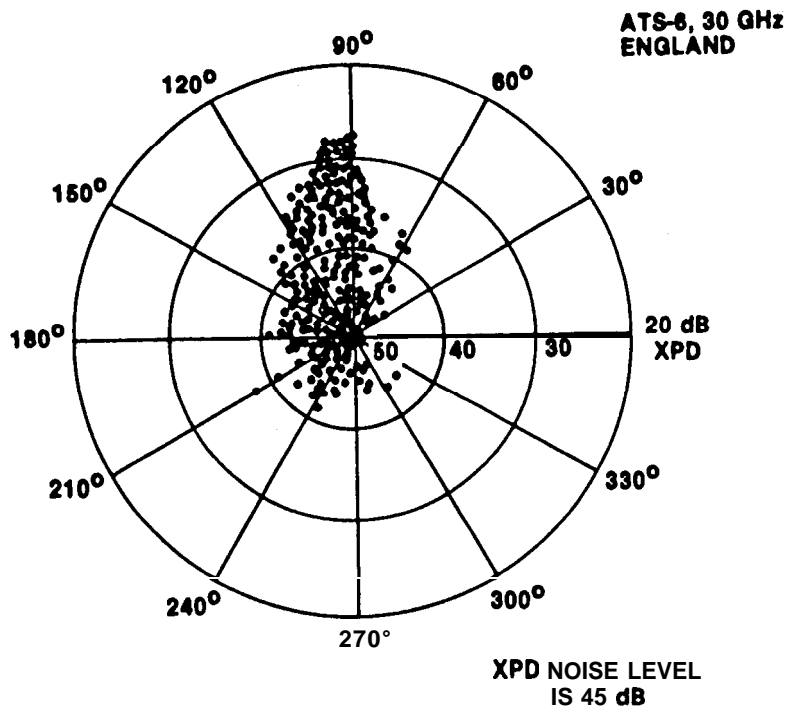


Figure 6.6-7. Polar Plot of the Cross Polarization Discrimination Arising from a Heavy Rain Event

electrostatic fields discharge rapidly resulting in" rapid relative phase shifts of 180°, and rapid decreases in XPD of 27 dB in 20 seconds (Shutie, et al-1977)' have been observed at the occurrence of a lightning flash. An example of this is shown in Figure 6.6-8 where the spikes in the relative phase occur for increasing XPD and result in large phase changes.

The spectra of rain and ice-induced crosspolarized signals have been analyzed (Hayworth, et al-1977) and it appears that a cancellation system with a 10 Hz bandwidth would track the majority of depolarizing events. However this bandwidth is probably insufficient during the sudden realignment of ice crystals in thunderstorms and in nonelectrically active precipitation. A suggestion has been made to consider use of a dual time constant system to accommodate all likely events.

For ice crystal depolarization the crosspolar phase shift is usually ±90 degrees of the copolarized signal and so differential attenuation dominates the XPD variations. This effect was displayed in Figure 6.6-6. However depending on the frequency, rain-induced XPD variations predominantly shift the phase near 20 GHz and below and induce differential attenuation from 20 to 60 GHz (Hogg and Chu-1975).

6.6.3.3 CCIR Estimation for Ice Depolarization. The CCIR (1986b, Rpt . 564-3) has provided an empirical factor, $C_{ice}(p)$, for estimating the contribution of ice depolarization at the percent of time p in terms of $XPD_{rain}(p)$, the cross polarization caused by rain. The resulting rain + ice XPD at the percent of time p, $XPD_T(p)$, is then determined from:

$$XPD_T(p) = XPD_{rain}(p) - C_{ice}(p) \quad , \text{ in dB} \quad (6.6-4)$$

where,

$$C_{ice}(p) = \frac{0.3 + 0.1109_{10} P}{2} XPD_{rain}(p) \quad (6.6-5)$$

Therefore,

$$\text{XPD}_T(p) = (0.85 - 0.05 \log_{10} P) \text{XPD}_{\text{rain}}(P) \quad (6*6-6)$$

This result, in conjunction with the CCIR estimation procedure for rain depolarization presented in Section 6.6.2.1.1, can be used to determine a total XPD distribution for a given set of link parameters.

6.6.4 Other Sources of Depolarization

6.6.4.1 Snow Depolarization. Snow depolarization occurs during both the winter and summer months. During the summer months snow exists above the 0°C isotherm. During winter, as the isotherm lowers, the thickness of the snow layer increases and the depolarization due to rain decreases.

In Canada (Hendry, et al-1976) tests using circularly polarized diversity radars at frequencies near 2.9 GHz (10.4 cm wavelength) and 16.7 GHz (1.8 cm wavelength) at an elevation angle of 3.2 degrees have diagnosed storms during both summer and winter. During June snow occurred during a storm from 2.6 to 8.2 km altitude and yielded a differential phase shift of 0.36 **deg/km** at 2.9 GHz. Winter data taken at 16.7 GHz gave more variable results of 0.16 to 1.17 **deg/km** for moderate to heavy snowstorms ranging in altitude from 70 m to 2.6 km. The mean value of differential phase shift was 0.69 **deg/km** at 16.7 GHz.

6.6.4.2 MultiPath Depolarization. The cross-polarized pattern of a parabolic reflector antenna normally has its peak at small angles off-axis. This allows oblique indirect rays, which may be present on earth-space paths at low elevation **angles**, to produce a significant cross-polarized component. Measurements have been made on terrestrial links at 11 GHz (Watson, et al-1973) and 22 GHz (Turner-1973). The magnitude of the indirect signal reflected from the earth can be roughly estimated from the data in Lord and Oliver (1946) taken near 3 GHz.

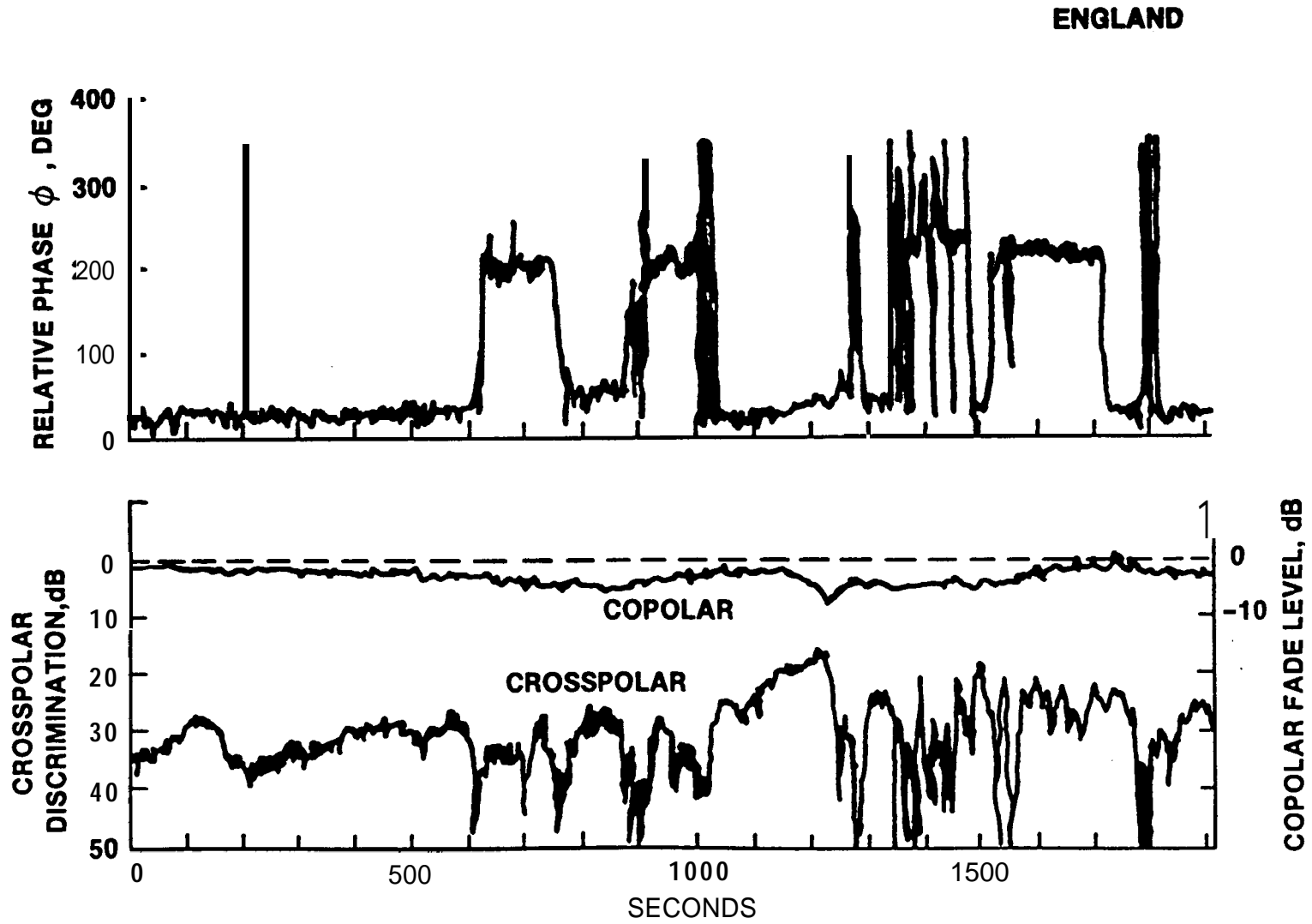


Figure 6.68. Phase, Copolar Fade and Crosspolar Discrimination for an Electrically Active Thunderstorm (15th July 1976)

6.6.4.3 Refractive Effects. Variations in the radio refractivity (dielectric constant of tropospheric layers) can cause rotation of the polarization plane of the rays refracting through the layers. This condition will occur for layers which are not perpendicular to the vertical plane containing the transmitter and receiver as described by LeFrancois, et al (1973).

6.6.5 Prediction of Depolarization Statistics

This section presents a summary of the procedure for developing a prediction of depolarization statistics, in the form of the cumulative distribution of XPD, for rain and ice-particle induced depolarization on a slant path. Figure 6.6-9 shows the methodology for developing the statistics. The XPD prediction requires the cumulative distribution of rain attenuation, either as measured or calculated from one of the methods described in Section 6.3.

The coefficients $\tilde{\alpha}$ and $\tilde{\beta}$ are determined at each percent p from the CCIR procedure, Eq. 's 6.6-2 and 6.6-3, for the given frequency, elevation angle, and polarization tilt angle (STEP 1). The rain induced XPD is then determined from the coefficients and from the rain attenuation distribution by Eq. 6.6-1 (STEP 2). The contribution from ice particles is determined from the **CCIR relationship**, Eq. 6.6-6 (STEP 3).

The procedure is valid in the frequency range $8 \leq f \leq 35$ GHz. Outside of this frequency range, attenuation statistics are not useful in predicting XPD **statistics**. For frequencies below 8GHz, relationships between XPD, point rain rate, and effective path length have been employed (see **Oguchi-1977, Kobayashi-1977**).

Long term XPD statistics obtained at one frequency and polarization tilt angle can be scaled (STEP 4) to another frequency and polarization tilt angle using the semi-empirical relation (**CCIR Rpt . 564-3, 1986b**),

$$\text{XPD}_2 = \text{XPD}_1 - 20 \log_{10} \left[\frac{f_2 \sqrt{1 - 0.484(1 + \cos 4\tau_2)}}{f_1 \sqrt{1 - 0.484(1 + \cos 4\tau_1)}} \right] \quad \text{for } 4 \leq f_1, f_2 \leq 30 \text{ GHz} \quad (6.6-7)$$

where XPD_1 and XPD_2 are the XPD values not exceeded for the same percentage of time at frequencies f_1 and f_2 and polarization tilt angles τ_1 and τ_2 , respectively. The above can be used to scale both rain and ice **depolarization**, since it has been observed that both phenomena have approximately the same frequency dependence at frequencies less than about 30 GHz.

Figure 6.6-10 show a sample calculation of the XPD procedure developed from cumulative attenuation statistics for Rosman, NC with the ATS-6 20 GHz satellite beacon. The attenuation statistics were obtained from the distribution extension technique described in Section 6.3. The curve labeled DEPOLARIZATION presents the XPD calculated from the procedure of Figure 6.6-9, with both the rain and rain + ice predictions shown.

Given: Location
 Frequency, f
 Elevation Angle, Θ
 Tilt Angle, T

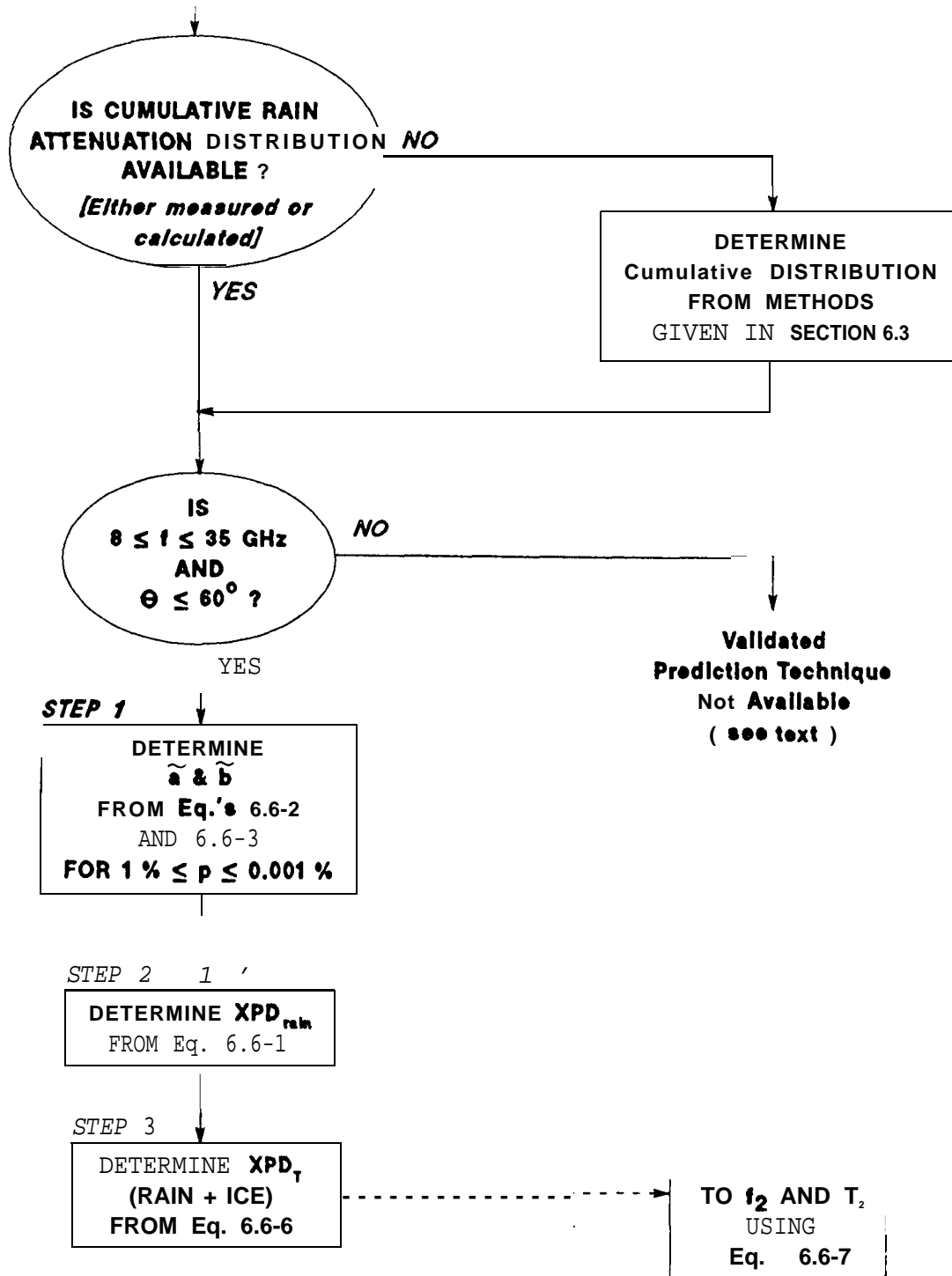


Figure 6.6-9. Technique for Prediction of Depolarization Statistics

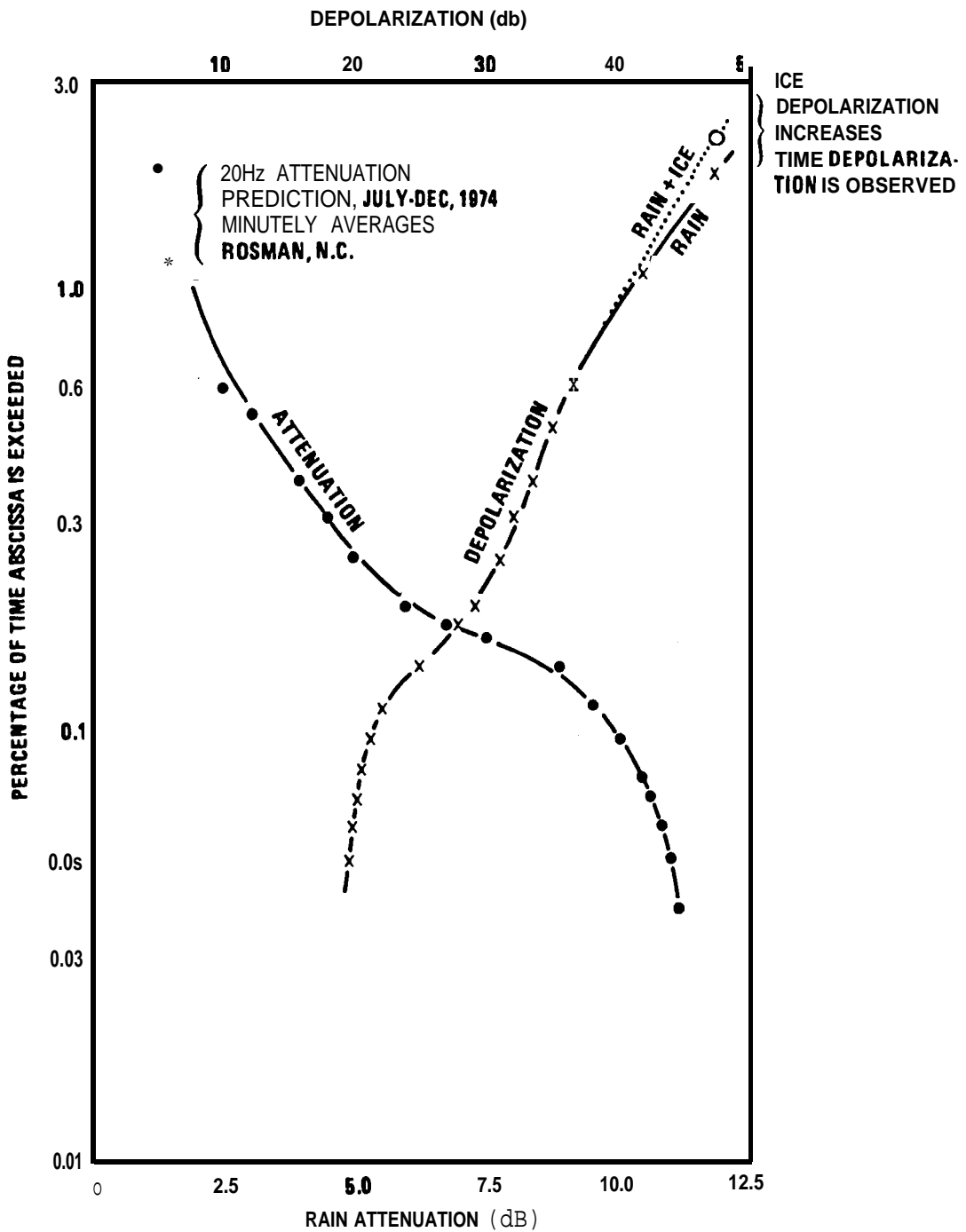


Figure 6.6-10. Attenuation and Depolarization Statistics for Rosman, N.E.

6.7 DISPERSION AND BANDWIDTH COHERENCE EFFECTS

When the dispersion of the propagating medium is sufficiently high, the phase and/or amplitude of wide-bandwidth transmissions may be selectively altered, causing a variation or reduction in the coherence bandwidth of the transmitted signal. **Both** tropospheric and ionospheric effects have been predicted and observed. This section reviews the analytical and experimental results for both tropospheric and ionospheric induced effects on radiowave paths operating above 10 GHz.

6.7.1 Tropospheric Effects on Bandwidth Coherence

6.7.1.1 Amplitude Variations

Theoretical estimates of the degradation of pulse shapes through rain have indicated **that** only minor effects are observed. The calculations (Crane-1967) indicated that pulse distortion does **not become significant until total rain attenuations of the order of 100 dB** are encountered. Since current link margins do not allow such high attenuations, the link will fail due to signal attenuation before pulse shape degradation affects transmission.

Amplitude variation with frequency **becomes significant at frequencies in the vicinity of molecular absorption bands, such as the 50-70 GHz oxygen absorption band.** The greatest dispersive effect would occur at the individual absorption lines which are quite narrow (Liebe -1955). However, due to the great path attenuation present at these frequencies, it is not likely they would be used for earth-space communications.

For rain the frequency dependence of the specific attenuation (db/km) is

$$\frac{\partial \alpha}{\partial f} = \frac{\partial (aR^b)}{\partial f} \propto \left[\frac{1}{a} \frac{\partial a}{\partial f} + (\ln R) \frac{\partial b}{\partial f} \right] \quad (6.7-1)$$

where, for example, for the frequency range from 8.5 to 25 GHz
(Olsen et al-1977)

$$\frac{\partial a}{\partial f} = 1.02 \times 10^{-4} f^{1.42} \quad (6.7-2)$$

$$\frac{\partial b}{\partial f} = -0.11 f^{-1.0779} \quad (6.7-3)$$

For example, at 20 GHz and R = 25 mm/hr,

$$a = 5.93 \times 10^{-2}$$

$$b = 1.12$$

$$\frac{\partial a}{\partial f} = 7.18 \times 10^{-3}$$

$$\frac{\partial b}{\partial f} = -4.36 \times 10^{-3}$$

$$\alpha = 2.18 \text{ dB/km}$$

so

$$\frac{\partial \alpha}{\partial f} = 0.23 \text{ dB/(km-GHz)}$$

or for a typical effective path length $L_e = 6 \text{ km}'$

$$\frac{\partial (\alpha L_e)}{\partial f} = L_e \frac{\partial \alpha}{\partial f} = 1.38 \text{ dB/GHz}$$

6.7.1.1.1 Experimental Results. The ATS-6 beacons at 20 and 30 GHz were both capable of being modulated with ± 180 , 360, 540 and ± 720 MHz sidetone signals. Typical selective fading events across the 1.44 GHz bands are shown in Figures 6.7-1 and 6.7-2, respectively (WEC-1975). These are four-second averages taken on day 270 of 1974 just before the onset of a fade event (2300002) at the beginning of the fade event (2323522), and before receiver lock was lost during the fade event (232428Z). Except for fade depths in excess of 20 dB, the accuracy of the attenuation measurements is +1 dB. These rain fade results, while representative of those taken at Rosman, do

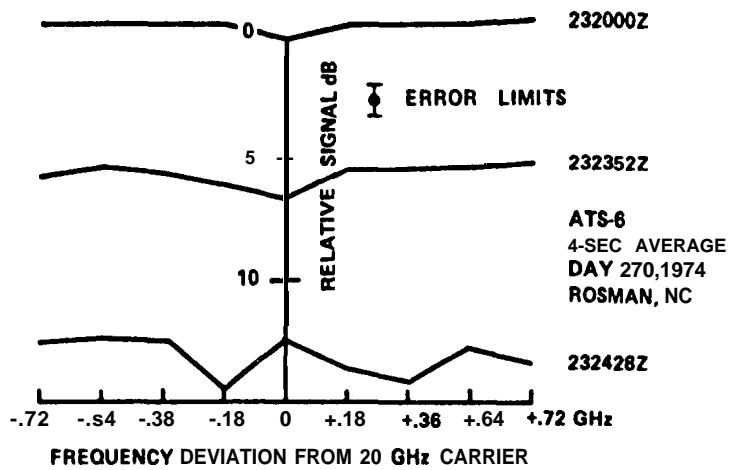


Figure 6.7-1. Selective Fading Near 20 GHz

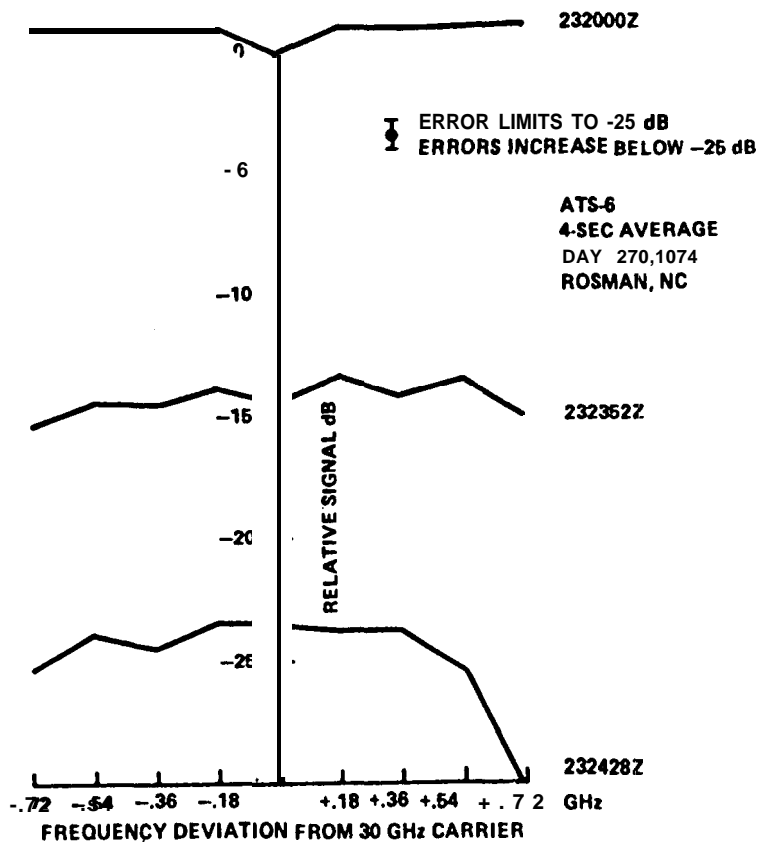


Figure 6.7-2. Selective Fading Near 30 GHz

not appear to be sufficiently accurate for deep fades because the signal levels approach the noise floor of the receiver. For one-minute averages, no measurable selective fading was observed (WEC-1975).

The cross-correlation of 4 and 6 GHz signals due to low angle fading in the Canadian arctic was found to be low (Strickland, et al-1977). During a 2.5 hour period on the day when the fading was most severe the correlation coefficient was 0.34 since the 6 GHz signal experienced 55% more fades than the 4 GHz signal. This would indicate significant dispersion was present, but the mechanism for this effect is tropospheric refraction and not rain. Frequency selective fading may be significant at low elevation angles.

6.7.1.2 Phase Variations. Phase measurements have not yielded significant results for frequencies above 10 GHz. The phase coherent sidetone signals on ATS-6 showed only minor variations across the 1.44 GHz bandwidths. These variations were most evident for the shorter (one and four second) averaging periods compared to the one-minute period (WEC-1975).

Phase measurements have been attempted for the one degree elevation angle satellites observed from the arctic (Strickland et al-1977). Unfortunately, no significant fade events occurred and no differential phase variations were recorded.

Phase effects are produced by the molecular absorption mechanism along with amplitude effects. Large values of phase dispersion would therefore be expected in the absorption bands.

6.7.2 Ionospheric Effects on Bandwidth Coherence

6.7.2.1 Amplitude Variations. Ionospheric attenuation at microwave frequencies is inversely proportional to the frequency squared (Flock, 1987) and is generally less than 0.001 dB at 15 GHz and an elevation angle $\theta = 90^\circ$. The variation is approximately related to cosecant θ . The attenuation is therefore usually less

than 0.01 dB above 10 GHz.

6.7.2.2 Phase Variations. The group delay due to the free electrons in the ionosphere is (Flock, 1987)

$$\Delta\tau = 40.3 \frac{N_e}{c f^2} = \frac{1.33 \times 10^{-7}}{f^2} N_e, \text{ sec} \quad (6.7-4)$$

where N_e is the total electron content in electrons/m², $c = 3 \times 10^8$ m/sec and f is in Hertz. This delay is equivalent to a phase delay (in radians)

$$\Delta\tau = \frac{\Delta\phi}{2\pi f} \quad (6.7-5)$$

so that

$$\Delta\phi = (2\pi)(40.3) \frac{N_e}{c f} \quad (6.7-6)$$

For a typical value of $N_e = 10^{17}$ m⁻², the total phase delay at 11.7 GHz is only 7.21 radians. The frequency dependence of this is only

$$\begin{aligned} \frac{\partial(\Delta\phi)}{\partial f} &= - \frac{2\pi(40.3) N_e}{c f^2} \\ &= -6.2 \times 10^{-10} \text{ radian/Hertz} \\ &= -0.62 \text{ radian/GHz} \\ &= -35 \text{ degrees/GHz.} \end{aligned}$$

For higher frequencies, the rate of change of phase with frequency decreases.

6.8 DOWNLINK NOISE AT EARTH STATIONS

6.8.1 Introduction

An Earth station observing a satellite at a high elevation angle

may be considered to be receiving sky noise from the antenna boresight direction. As the elevation angle of the satellite decreases, thermal noise emission from the Earth's surface will be increasingly observed in the antenna's sidelobes. This section reviews the sky noise component and its contribution to satellite communications system performance.

Antenna noise is conveniently treated in terms of noise temperature, since the two parameters are linearly related. In circuit theory the noise power, P_n , which is transferred to a matched load is

$$P_n = kTB \quad \text{watts} \quad (6.8-1)$$

where k is Boltzmann's constant, T is noise temperature in (degrees) Kelvin, and B is the bandwidth in Hertz. Thermal radiation from the gaseous atmosphere is given by the Rayleigh-Jeans longwave approximation to Plank's equation

$$p_n' = \frac{2kT}{\lambda^2} = 22.2kTf^2 \quad (6.8-2)$$

where f is the frequency in GHz. Note the ambiguity in the frequency dependence of the two relations. However, we will be considering noise temperature in its circuit theory usage so the difference is not of prime concern.

6.8.2 Clear Air Sky Noise

The thermal noise emission from a gas in thermodynamic equilibrium, from Kirchhoff's law, must equal its absorption, and this equality must be true at all frequencies.

The noise temperature T_b in a given direction through the atmosphere (also called the brightness temperature) is given by radiative transfer theory (Waters-1976, Wulfsberg-1964)

$$T_b = \int_0^{\infty} T_m \gamma e^{-\tau} dl + T_{\infty} e^{-\tau_{\infty}} \quad (6.8-3)$$

where T_m is the ambient temperature, γ is the absorption coefficient, and τ is the optical depth to the point under consideration. In radio engineering terms

$$\tau = 4.343 A \quad \text{dB} \quad (6.8-4)$$

where A is the absorption over the path in question, in dB. For frequencies above 10 GHz, the second term on the righthand side of Eq. (6.8-3) reduces to 2.7 K, the cosmic background component, unless the Sun is in the antenna beam, as illustrated in Figure 6.8-1.

For an isothermal atmosphere (T_m constant with height), substituting $\gamma dl = d\tau$ in Eq. (6.8-3) yields

$$T_b = T_m(1 - e^{-\tau}) = T_m \left(1 - 10^{-\frac{A}{10}} \right) \quad \text{K} \quad (6.8-5)$$

where A is again atmospheric absorption in dB. The value of T_m taken in Eq. (6.8-4) ranges from 260 to 280 K. One relationship used to determine a value of T_m from surface measured temperature is (Wulfsberg-1964)

$$T_m = 1.12 T_s - 50 \quad \text{K} \quad (6.8-6)$$

where T_s is the surface temperature in K.

Noise temperature (or brightness temperature) curves for 3, 7.5, and 17 g/m³ surface water vapor content, with the US Standard Atmosphere for the two lower values and the Tropical Atmosphere for the highest value, have been published by Smith (1982) and reproduced in CCIR Report 720-2 (CCIR-1986h). Examples for an average humidity state (7.5 g/m³ at the surface) are reproduced as Figures 6-8-2 and 6.8-3.

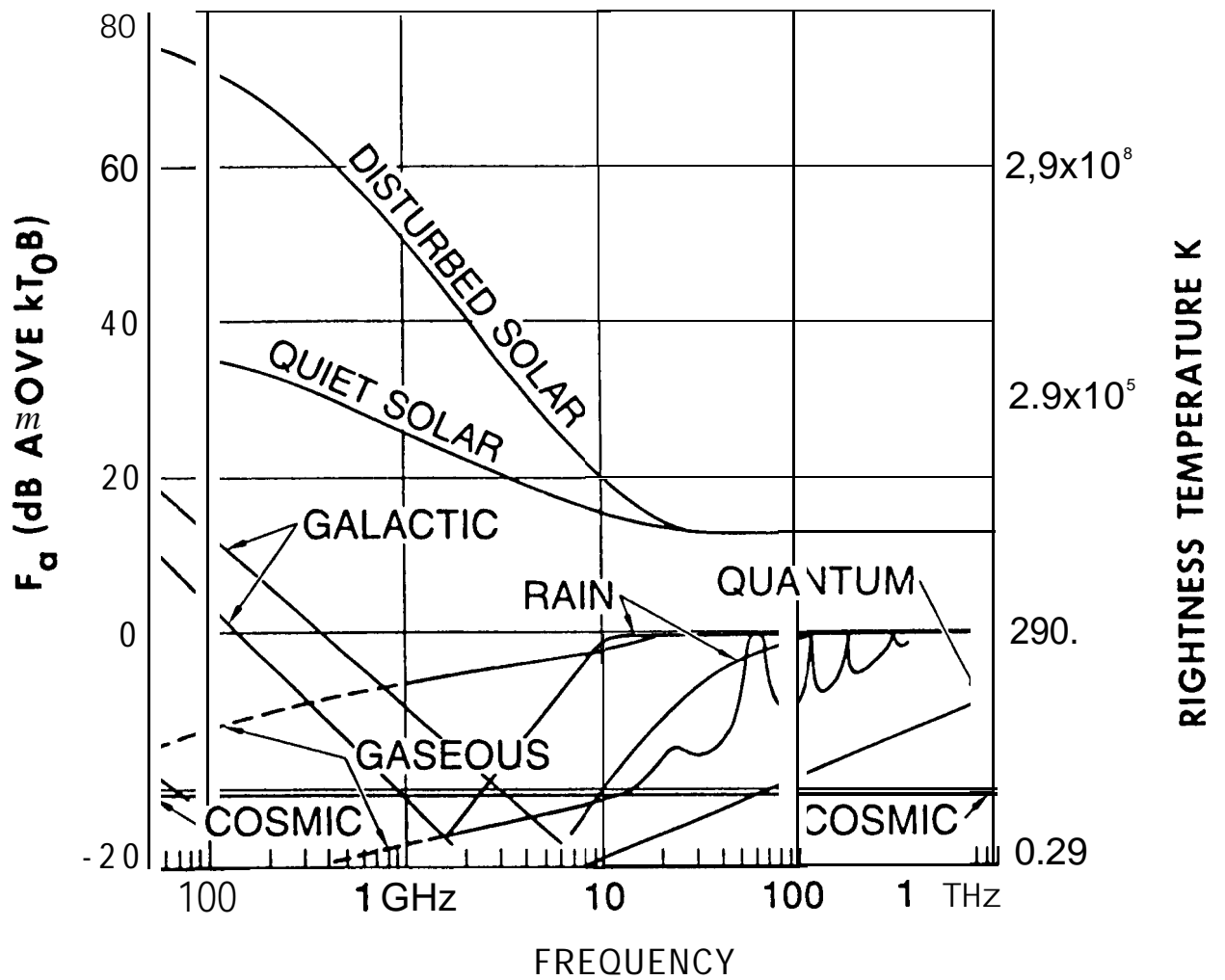


Figure 6.8-1. Noise Factor and Brightness Temperature from Natural Sources observed on Satellite Downlinks
 [Source: Spaulding and Hagn - 1978]

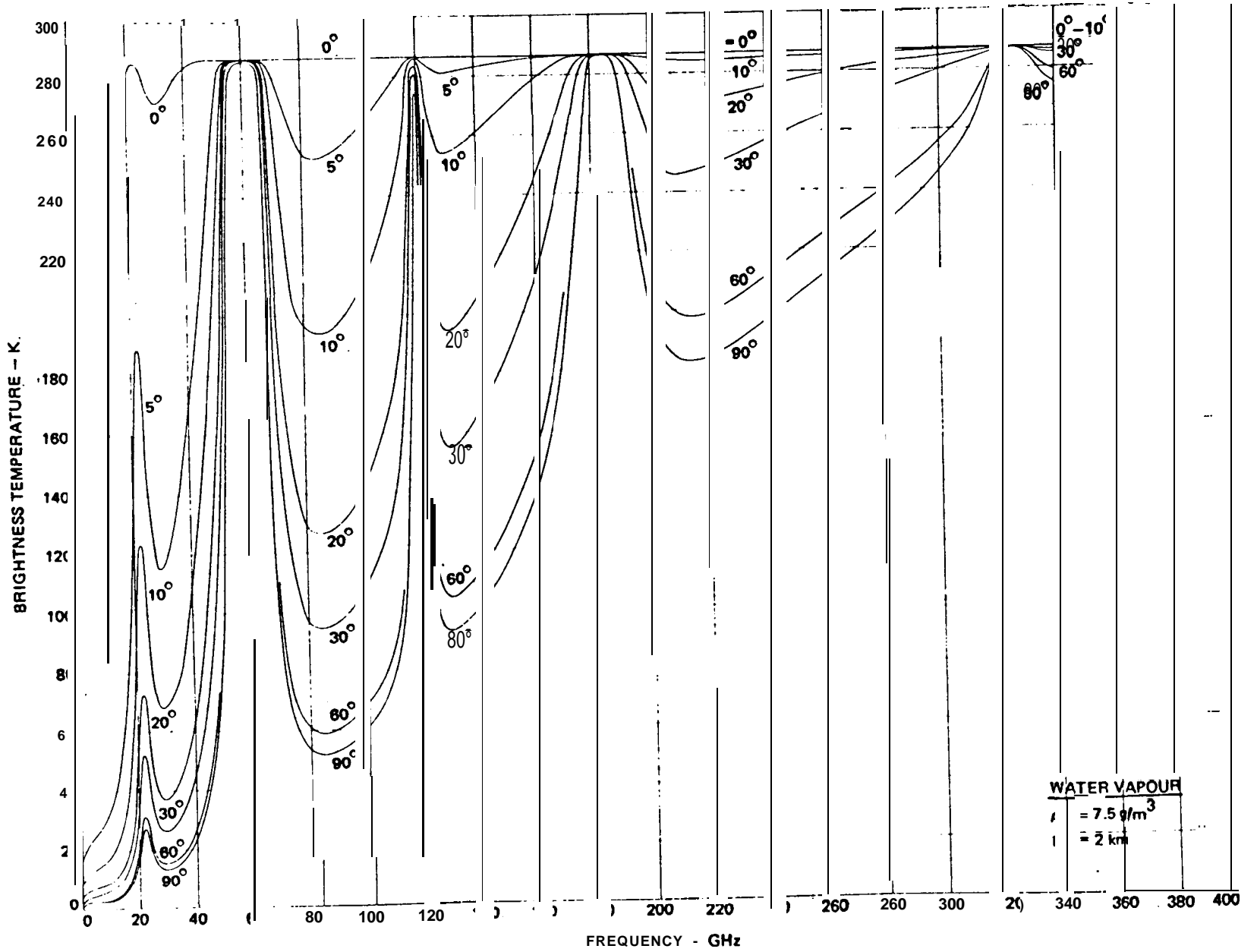


Figure 6.8-2. Brightness Temperature (Clear Air) for a Water Vapor Concentration of 7.5 g/m³, 1 to 350 GHz. [Smith - 1982]

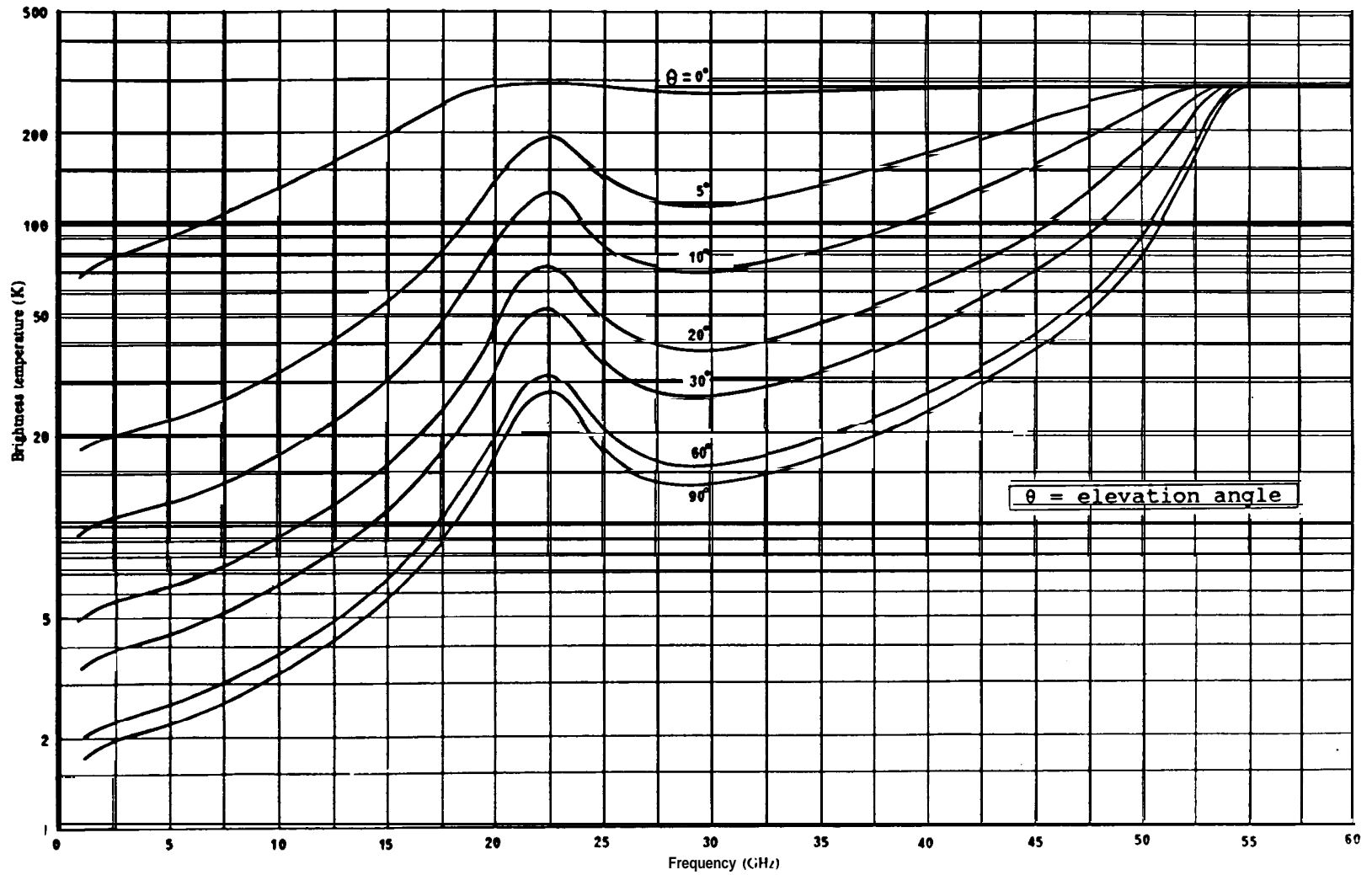


Figure 6.8-3. Brightness Temperature (Clear Air) for a Water Vapor Concentration of 7.5 g/m³, Expanded Scale, 1 to 60 GHz. [Smith - 1982]

6.8.3 Sky Noise Due to Rain

Kirchhoff's law applies to noise emission from rain as well as from atmospheric gases, but only to the absorption component of the rain attenuation and not to the scattered component. The scattered component increases with frequency, so that while Eq. (6.8-5) may be appropriate at 10 GHz, it will give too high a value at 70 GHz.

Values of T_s due to rain may be estimated from the rain attenuation calculation techniques presented in Section 6.3. For example, to compute the cumulative statistics of T_s , first compute the cumulative attenuation statistics due to rain, and then use Eq. 6.8.5 to convert attenuation to apparent sky noise temperature. An example of this process has been done for Rosman, NC at 20 GHz. The results are given in Table 6.8-1.

The sky noise temperature (see last column of Table 6.8-1) will degrade the overall system noise figure of the receiver system. For example, for a receiver with a 4 dB noise figure, the resultant noise figure for the rain rate corresponding to 0.01% of the year will be 5.4 dB, i.e., an increase of 1.4 dB.

6.8.4 Sample Calculations

Two illustrative examples of application of the sky noise relationships for clear air and for rain are presented below.

Example 1. A land mobile satellite system downlink is to operate at 20 GHz with a service reliability of 95 % of the time. The receiver system noise temperature, exclusive of antenna noise, is 100 K. The elevation angle to the satellite is 60°. The median surface humidity is estimated at 7.5 g/m³. What is the *required* propagation margin?

From Figure 6.8-3 we read $T = 20$ K for the parameters given above. For the worst .5 % of the time we arbitrarily double this value to $T = 40$ K.

The gaseous attenuation for the link can be determined from the

Table 6.8-1. Cumulative Statistics of Sky Temperature Due to Rain for Rosman, N.C. at 20 GHz. $T_m = 275$ K.

PERCENT OF YEAR	POINT RAIN RATE VALUES	AVERAGE RAIN RATE	TOTAL RAIN ATTENUATION*	SKY NOISE Temperature
0.001	102 mm/hr	89 mm/hr	47 dB	275 K
0.002	86	77	40	275
0.005	64	60	30	275
0.01	49	47	23	274
0.02	35	35	16	269
0.05	22	24	11	252
0.1	15	17	7	224
0.2	9.5	11.3	4.6	180
0.5	5.2	6.7	2.6	123
1.0	3.0	4.2	1.5	82
2.0	1.8	2.7	0*93	53

NOTES :

* At 20 GHz the specific attenuation $A = 0.06 R_{ave}^{1.12}$ dB/km and for Rosman, N.C. the effective path length is 5.1 km to ATS-6.

t For a ground temperature of $17^{\circ}\text{C} = 63^{\circ}\text{F}$ the $T_m = 275$ K.

CCIR estimation procedure given in Section 6.2.3. The resulting total (oxygen + water vapor) attenuation is found as

$$A_g = 0.34 \text{ dB}$$

Doubling the value for the worst 5 % of the time, the attenuation is 0.68 dB.

At the 95 % reliability level, attenuation caused by rain may be ignored, since rain occurs only 2-3 % of the total time for most regions.

The propagation margin is then computed as follows:

Decrease in signal level = 0.68 dB.

$$\begin{aligned} \text{Increase in noise temperature} &= 10 \log[(100 + 40 + 2.7)/100] \\ &= 1.54 \text{ dB} \end{aligned}$$

Required propagation margin = 0.68 + 1.54 = 2.22 dB.

Note that for this case the sky noise increase contribution is more than double the contribution due to the decrease in signal level to the total margin required.

Example 2. A satellite system is to operate in the fixed service with a downlink at 20 GHz. The required service reliability is 99.99 % of the time. The 0.01 % of the time rain rate has been measured to produce an attenuation of 30 dB in the direction of the satellite. The receiver system noise temperature, exclusive of antenna noise, is 300 K. What is the required propagation margin?

The clear air component is assumed to be the 95 % value from example 1, i.e. $T = 40 \text{ K}$, $A = 0.68 \text{ dB}$.

The sky noise increase due to a rain attenuation of 30 dB is determined from Eq. (6.8-5)

$$T_r = 280(1 - 10^{-30/10}) = 279.7 \text{ K}$$

The propagation margin is then computed as follows:

$$\text{Decrease in signal level} = 30 + 0.68 = 30.68 \text{ dB.}$$

$$\begin{aligned} \text{Increase in noise temperature} &= 10 \log[(279.7 + 300)/300] \\ &= 2.86 \text{ dB.} \end{aligned}$$

$$\text{Required propagation margin} = 30.68 + 2.86 = 33.54 \text{ dB.}$$

For this example the signal level decrease is the predominate factor in the margin requirement.

Note that the reliability criterion plays a significant role in propagation margins for the two above examples (2.22 vs 33.54 dB). The relative difference in receiver noise temperature, however, also accounts for the greater importance of noise over attenuation in the first example.

6.8.5 Sky Noise Due to Clouds, Fog, Sand and Dust. The major contributor to the sky noise temperature is the medium with the highest attenuation. Generally, clouds will present higher attenuations than fog, sand or dust. For example, for cumulus clouds with no precipitation the water density will be approximately 0.5 g/m^3 . For the Rosman example described earlier (20 GHz),

$$A = KC \rho_1 t_c \csc \theta \quad (6.8-7)$$

where t_c is the thickness of the clouds (typically 2 kilometers). Using typical numbers

$$\begin{aligned} A &= (0.4 \text{ dB m}^3/\text{gm km}) (0.5 \text{ gm/m}^3) (2 \text{ km}) \csc (47^\circ) \\ &= 0.55 \text{ dB} \end{aligned}$$

The corresponding sky noise contribution is then

$$T_S = T_{mc} [1 - 10^{-(0.55/10)}]$$

With T_{mc} equal to the temperature of the cloud (i.e., $T_{mc} =$

0°C = 273 K), T_s is 32 K. Clearly, at 20 GHz, rain represents a much more significant contributor to the sky noise temperature than clouds .

6.8.6 Total Sky Noise Temperature Arising from Several

Contributors. The sky noise temperatures from several sources do not add linearly. Rather, the attenuation from each contributor must be added and the total result substituted into the sky noise versus attenuation relation. For example, for the Rosman ground station observing the ATS-6, the clear air attenuation is 1.2 dB yielding a T_s (clear air) = 66 K. From Table 6.8-1 for 0.2% of the year (105 minutes) the rain induced sky temperature due to, clear air and rain is 203 K which is significantly less than the sum of each contributor (246 K) . During rain conditions the cloud contributions should also be added, but these will generally be even a smaller contribution than the clear air attenuation.

6.8.7 Extraterrestrial Sources of Sky Noise

6.8.7.1 Solar Noise. The sun generates very high noise levels when it is collinear with the Earth station-satellite path. For geostationary satellites, this occurs near the equinoxes, for a short period each day. The power flux density generated by the sun is given as a function of frequency in Figure 6.8-4 (Perlman, et al-1960) . Above about 20 GHz, it is practically constant at -188 dBW/Hz-m² for "quiet sun" conditions.

Reception of solar noise can be viewed as an equivalent increase in the antenna noise temperature by an amount T_s . T_s depends on the relative magnitude of the antenna beamwidth compared with the apparent diameter of the sun (0.480), and how close the sun approaches the antenna boresight. The following formula, after Baars (1973), gives an estimate of T_s (in Kelvins) when the sun, or another extraterrestrial noise source, is centered in the beam.

$$T_s = \frac{1 - e^{-\left(\frac{D}{1.201}\right)^2}}{f^2 D^2} \log^{-1}\left(\frac{S + 250}{10}\right) \quad (6.8-9)$$

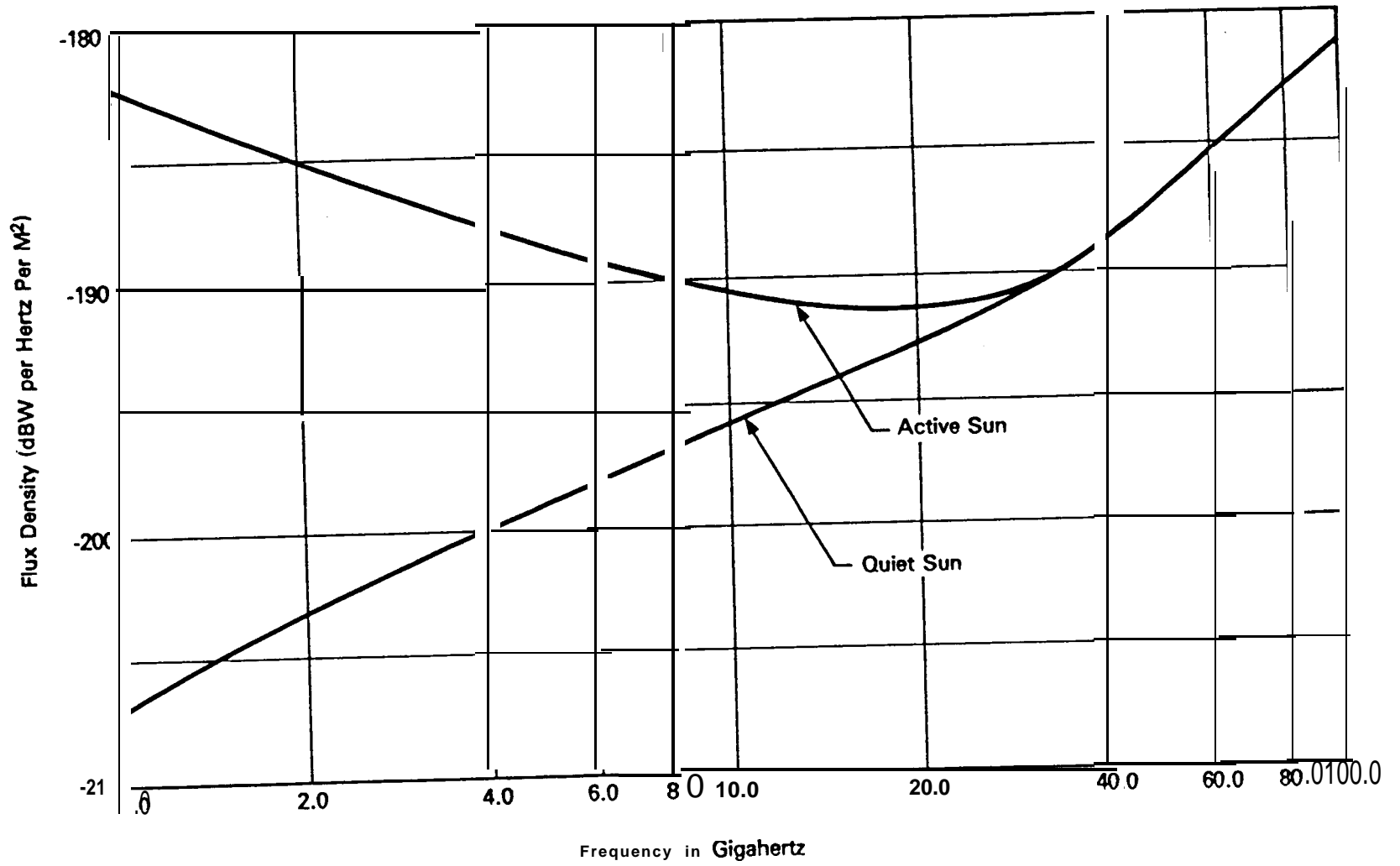


Figure 6.8-4. Values of Noise from Quiet and Active Sun

where D = apparent diameter of the sun, deg
 f = frequency, GHz
 S = power flux density, dBW/Hz-m²
 θ = antenna half-power beamwidth, deg

For an Earth station operating at 20 GHz with a 2 m diameter antenna (beamwidth about 0.5°) , the maximum increase in antenna temperature that would be caused by a ("quiet") sun transit is about 8100 K, according to the formula.

The sun's flux has been used extensively for measuring tropospheric attenuation. This is done with a sun-tracking radiometer, which monitors the *noise* temperature of an antenna that is devised to automatically remain pointed at the sun.

6.8.7.2 Lunar Noise. The moon reflects solar radio energy back to the Earth. Its apparent size is approximately 1/2 degree in diameter, like the sun. The noise power flux density from the moon varies directly as the square of frequency, which is characteristic of radiation from a "black body." The power flux density from the full moon is about -202 dBW/Hz-m² at 20 GHz. The maximum antenna temperature increase due to the moon, for the 20 GHz 2m antenna considered earlier, would be only about 320K. Because of the phases of the moon and the ellipticity of its orbit, the apparent size and flux vary widely, but in a regular and predictable manner. The moon has been used in measuring Earth station G/T (Johannsen and Koury-1974).

6.8.7.3 Radio Stars. The strongest radio stars are ten times weaker than the lunar emission. The strongest stars (Wait, et al-1974) emit typically -230 dBW/Hz-m² in the 10 to 100 GHz frequency range. Three of these strong sources are Cassiopeia A, Taurus A and Orion A. These sources are sometimes utilized for calibration of the ground station G/T. During the calibrations the attenuation due to the troposphere is usually cancelled out by comparing the sky noise on the star and subtracting the adjacent (dark) sky noise.

6.9 UPLINK NOISE IN SATELLITE ANTENNAS

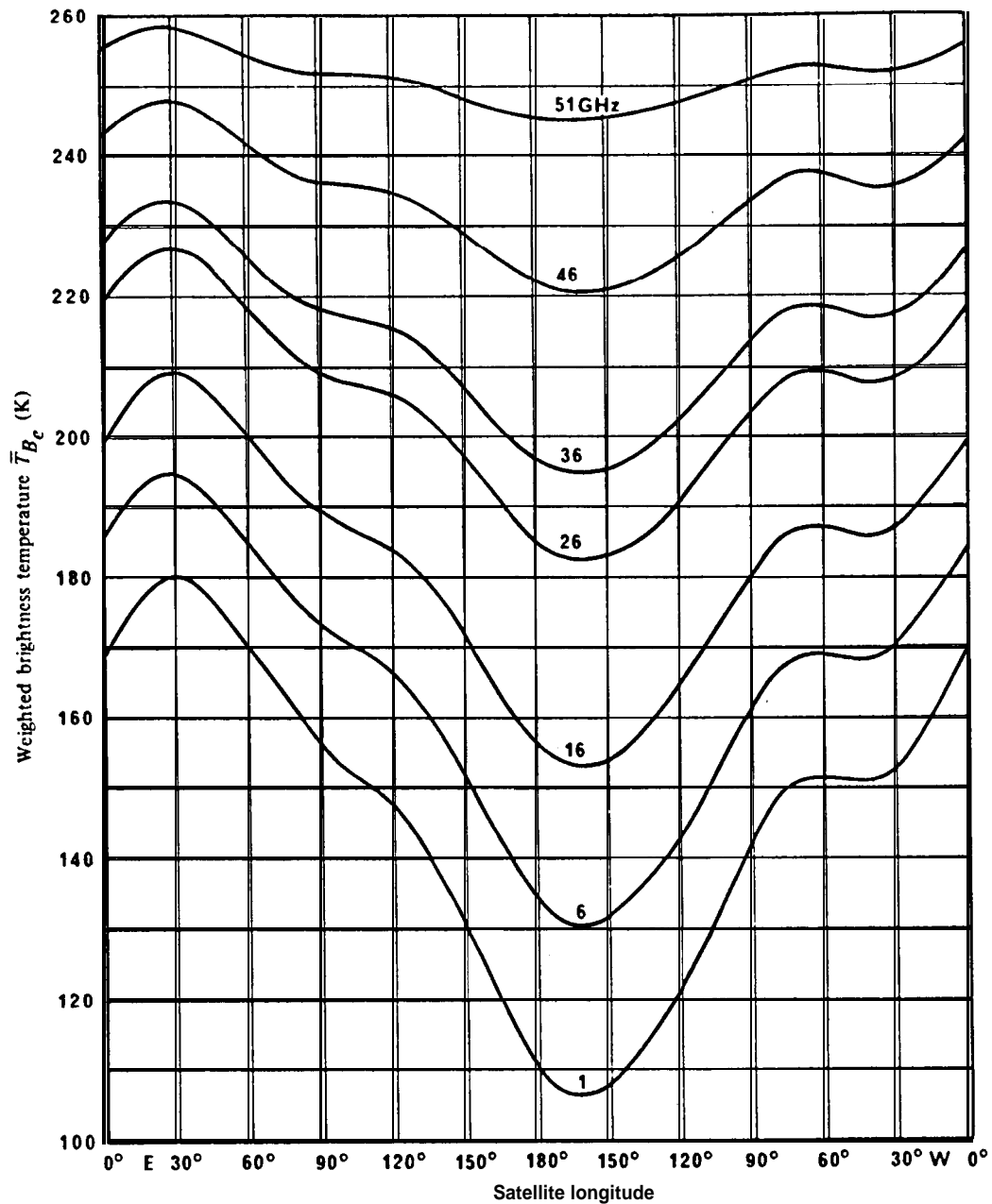
6.9.1 Components of Uplink Noise

The earth viewing (uplink) antenna of an orbiting satellite typically includes only a portion of the earth's surface within its half-power beamwidth. The observed noise is a complex function of atmospheric and surface temperature, elevation angle, frequency, and antenna gain (see, for example, Report 720-2, CCIR-1986h) . A major factor in the observed noise temperature is the fraction of land (high brightness temperature) to sea (low brightness temperature) in the main antenna beam. This factor is illustrated in Figure 6.9-1, which shows the variation in antenna temperature at a geostationary satellite using an earth-coverage antenna with a gaussian beam as it is moved around the geostationary orbit (Njoku and Smith - 1985) . At the lowest frequency (1 GHz) the variation with subsatellite longitude is entirely due to the land/sea fraction. As the frequency increases, the effects of the atmosphere come into play. The brightness temperature values used to compute Figure 6.9-1 are given in Figure 6.9-2, as a function of frequency and location (latitude), and they may be used for computation of more specialized satellite antenna coverage systems.

6.9.2 Sample Calculation

Consider a satellite in geostationary orbit that has a spot beam directed at the Washington D.C. area such that 60 % of the area within the 3 dB contour is land and 40 % is sea. The great-circle distance from the sub-satellite point to the center of the spot beam is 60° in equivalent latitude and the frequency is 40 GHz. What is the uplink antenna noise temperature at the satellite?

The satellite antenna noise temperature T_s may be approximated from Figure 6.9-2. The land portion will have a brightness temperature of 275 K, and the sea portion will be 185 K. Therefore



Curves are for US Standard Atmosphere with 7.5 g/cm^3 water vapor and 50% cloud cover. The Earth Coverage antenna pattern is given by

$$G(\phi) = -3 \left(\frac{\phi}{8.715} \right)^2 \text{ dB} \quad \text{for } 0 \leq \phi \leq 8.715$$

where ϕ is the angle off of boresight. (Njoku and Smith 1985)

Figure 6.9-1. Weighted Brightness Temperature of the Earth as a Function of Longitude, Viewed from Geostationary Orbit at Frequencies between 1 and 51 GHz.

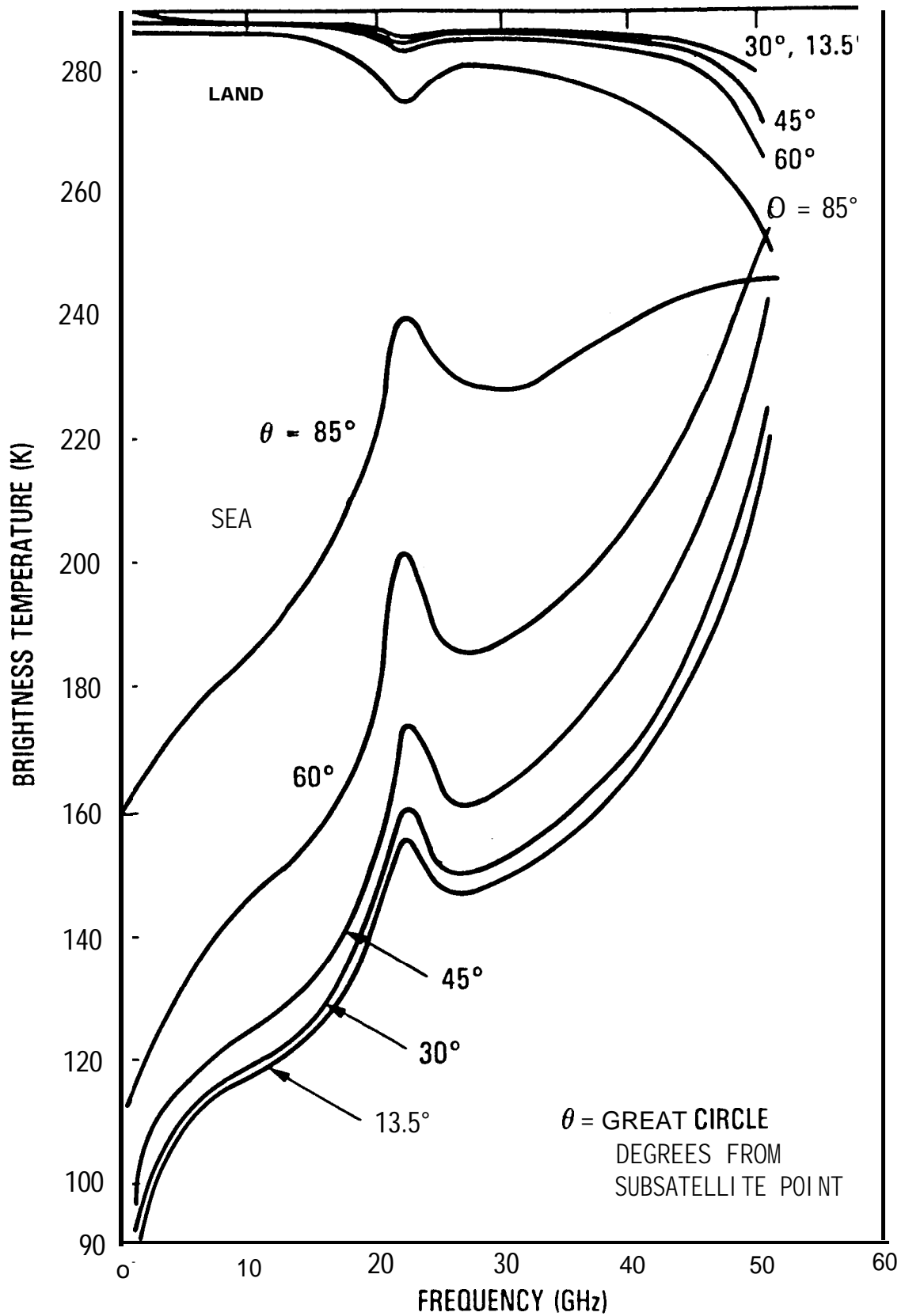


Figure 6.9-2. Brightness Temperature Contributions for Land and Sea, as a Function of Frequency and Latitude.

$$T_s = 0.6(275) + 0.4(185) = 239 \text{ K}$$

A more exact determination involves weighting each incremental area in the antenna beam by the appropriate off-boresight antenna gain. The additional accuracy is usually not necessary, however, since current satellite receiver noise temperatures are typically 1000 K or higher, and the incremental difference in the total system noise temperature would likely be very small.

6.10 REFERENCES

- Ahmed, I.Y. and L.J. Auchterlouie (1976), "Microwave Measurements of Dust Using an Open Resonator," Electronics Letters, Vol. 12, No. 17, p. 445.
- Allnutt, J.E. (1976), "Slant Path Attenuation and Space Diversity Results using 11.6 GHz Radiometers," Proceedings IEE, Vol. 123, p. 1197.
- Allnutt, J.E. (1985), "Low Elevation Angle Propagation Measurements in the 6/4 GHz and 14/11 GHz Band," IEE Conf. Publ. No. 248, IEE Fourth International Conf. On Antennas and Propagation, (ICAP 85), U. of Warwick, Coventry, U.K., 16-19 April, 1985, pp " 57-61.
- Altshuler, E.A. (1984), "A Simple Expression for Estimating Attenuation by Fog at Millimeter Wavelengths," IEEE Trans. Ant. & Prop., Vol. AP-32, No. 7, pp. 757-758.
- Altshuler, E.A. (1986), "Addendum to A Simple Expression for Estimating Attenuation by Fog at Millimeter Wavelengths," IEEE Trans. Ant. & Prop., Vol. AP-34, No. 8, pp. 1067.
- Ansari, A.J., and B.G. Evans, (1982), "Microwave Propagation in Sand and Dust Storms," Proc. IEE, vol. 129, Part 5, No. 5, pp. 315-322.
- Baars, J.W.M. (1973), "The Measurement of Large Antennas with Cosmic Radio Sources," IEEE Trans. Ant. Prop., Vol. AP-21, No. 4, pp. 461-474.
- Bashir, S.O., A.W. Dissanayake, and N.J. McEwan (1980), "Prediction of forward scattering and cross-polarization due to dry and moist haboob and sandstorms in Sudan in the 9.4 GHz band," Telecom. J., Vol 47, No. VII, pp. 462-467.
- Bean, B.R. and E.J. Dutton (1966), "Radio Meteorology," National Bureau of Standards Monograph 92, republished in paperback by Dover.
- Bergmann, H.J. (1977), "Satellite Site Diversity: Results of a Radiometer Experiment at 13 and 18 GHz," IEEE Trans. Ant. Prop., Vol. AP-25, p" 483.
- Bostian, C.W. and J.E. Allnutt (1979), "Ice-Crystal Depolarization on Satellite-Earth Microwave Radio Paths," Proc. IEE, Vol. 126, p. 951.
- Bostian, C.W., S.B. Holt, Jr., S.R. Kauffman, E.A. Manus, R.E. Marshall, W.L. Stutzman and P.H. Wiley (1977), "Rain Depolarization and Attenuation Measurements at 11.7, 19.04 and 28.56 GHz: A Description of the Experiment and Some

Preliminary Results, " URSI Comm. F Proc., April 28 - May 6, La Baule, France, pp. 403-408.

- Bostian, C.W., w.L. Stutzman, E.A. Manus, P.H. Wiley, R.E. Marshall and P. Santago (1979), "Summary of 1978 Attenuation and Depolarization Measurements Made With the CTS (11.7 GHz) and COMSTAR (19.04 and 28.56 GHz) Beacons," Invited Paper for the USNC/URSI Special Sessions on Propagation Above 10 GHz, June 18-20, Seattle, Washington.
- Bostian, C.W., Pratt, T., & Stutzman, W.L. (1986), "Results of a Three-Year 11.6 GHz Low-Angle Propagation Experiment Using the SIRIO Satellite," IEEE Trans. Ant. & Prop., Vol. AP-34, No. 1, pp. 58-65.
- Bostian, C.W., Stutzman, W.L., & Pratt, T. (1987), "SIRIO Results at Virginia Tech," Alta Frequenza, Vol LVI, N. 1-2, pp. 95-99.
- CCIR (1978), "Propagation In Non-Ionized Media," Volume V, Recommendations and Reports of the CCIR - 1978, International Telecommunication Union, Geneva.
- CCIR (1981a), Propagation Data Required for Space Telecommunication Systems, Report 564-1 (MOD F) , Dec. 5/1044, Geneva, Switzerland.
- CCIR (1981b), Radiometeorological Data Report 563-1 (MOD F), Dec. 5/5049, Geneva, Switzerland.
- CCIR (1981c), Attenuation by Precipitation and Other Atmospheric Particles, Report 721 (MOD F) Dec. 5/5026, Geneva, Switzerland.
- CCIR (1981), "Draft Revision of Report 720 (MOD #I) ," Document USSG 5/31, 12 March.
- CCIR (1982), Radio Propagation Factors Relating to Frequencies Near 12.5 and 17.5 GHz, Dec. A/68, 2 July 1982, Preparatory Meeting SAT-R2, Geneva, Switzerland.
- CCIR (1986a), Propagation in Ionized Media, Volume VI, Recommendations and Reports of the CCIR - 1986, International Telecommunication Union, Geneva.
- CCIR (1986b), "Propagation Data and Prediction Methods Required for Earth-Space Telecommunications Systems," Report 564-3, in Volume V, Recommendations and Reports of the CCIR - 1986, International Telecommunication Union, Geneva.
- CCIR (1986c), "Radiometerological Data," Report 563-3, in Volume V, Recommendations and Reports of the CCIR - 1986, International Telecommunication Union, Geneva.
- CCIR (1986d), "Attenuation By Atmospheric Gases," Report 719-2, in Volume V, Recommendations and Reports of the CCIR - 1986,

International Telecommunication Union, Geneva.

- CCIR (1986e), "Worst Month Statistics," Report 723-2, in Volume V, Recommendations and Reports of the CCIR - 1986, International Telecommunication Union, Geneva.
- CCIR (1986f), "Attenuation by Hydrometeors, In Particular Precipitation and Other Atmospheric Particles," Report 721-2, in Volume V, Recommendations and Reports of the CCIR - 1986, International Telecommunication Union, Geneva.
- CCIR (1986g), "Cross-polarization Due to the Atmosphere," Report 722-2, in Volume V, Recommendations and Reports of the CCIR - 1986, International Telecommunication Union, Geneva.
- CCIR (1986h), "Radio Emissions from Natural Sources in the Frequency Range Above About 50 Mhz," Report 720-2, in Volume V, Recommendations and Reports of the CCIR - 1986, International Telecommunication Union, Geneva.
- CCIR (1988), "Attenuation by Atmospheric Gases," Report 719-2, Dec. 5/156, International Telecommunication Union, Geneva, 18 April, 1988.
- Canada Atmospheric Environment (1973), Short Duration Rainfall Intensity-Duration-Frequency Graphs, Downsview, Ontario, Canada.
- Chu, T.S. (1974), "Rain-Induced Cross-Polarization at Centimeter and Millimeter Wavelengths," Bell Syst. Tech. Jrnl., Vol. 58, No. 8, pp. 1557-1579.
- Chu, T.S. (1979), "Effects of Sandstorms on Microwave Propagation," Bell System Tech. J., Vol. 58, pp. 549-555.
- Chu, T.S. (1980), "Microwave Depolarization of an Earth-Space Path," Bell System Technical Journal, Vol. 59, No. 6, pp. 987-1007.
- Crane, R.K. (1967), "Coherent Pulse Transmission through Rain," IEEE. Trans. Ant. Prop., Vol. AP-15, p. 252.
- Crane, R.K. (1976), An Algorithm to Retrieve Water Vapor Information from Satellite Measurements, NEPRF Tech-Rept. 7-76, Final Report, Project No. 1423, Environmental Research & Technology, Inc., Concord, Mass.
- Crane, R.K. (1976a), "Refraction Effects in the Neutral Atmosphere," Astrophysics, Part B. Radiotelescopes, Vol. 12 of Methods of Experimental Physics, M. C. Weeks, ed., Academic Press, N. Y.
- Crane, R.K. (1977), "Ionospheric Scintillations," Proc. IEEE, Vol. 65, pp. 180-199.
- Crane, R.K. (1980), "Prediction of Attenuation by Rain," IEEE Trans.

- Crane, R.K. (1980a), "Earth-Space and Terrestrial Microwave Propagation - Estimation of Rain Attenuation with the Global Model," ERT Technical Report P-A414-TR, prepared for NASA Headquarters under Contract NASW-3337 (October 1980).
- Crane, R.K. and D.W. Blood (1979), Handbook for the Estimation of Microwave Propagation Effects-Link Calculations for the Earth Space Paths, Environmental Research & Technology, Inc., Concord, Mass., report to NASA/GSFC under Contract NAS5-25341.
- Crane, R.K. and W.E. DeBrunner (1978), "Worst-Month Statistics," Electronics Letters, Vol. 14, No. 2, pp. 38-40.
- Davies, P.G. (1976), "Diversity Measurements of Attenuation at 37 GHz with Sun-Tracking Radiometers in a 3-site Network," Proceedings IEE, Vol. 123, p. 765.
- Davies, P.G. and D.L. Croom (1974), "Diversity Measurements of Attenuation at 37 GHz with Solar-Tracking Radiometers," Electronics Letters, Vol. 10, p. 482.
- Devasirvatham, D. and D.B. Hedge (1977), "Amplitude Scintillations on Earth-Space Propagation Paths at 2 and 30 GHz," The Ohio State University ElectroScience Lab., Tech. Rpt. 4299-4.
- Dintelmann, F. (1981), "Analysis of 11 GHz Slant Path Fade Duration and Fade Slope," Electronics Letters, Vol. 11, No. 22, pp. 547-548.
- Engelbrecht, R.S. (1979), "The Effect of Rain on Satellite Communications Above 10 GHz," RCA Review, Vol. 40, p. 191.
- Ferguson, A. and R.R. Rogers (1978), "Joint Statistics of Rain Attenuation on Terrestrial and Earth-Space Propagation Paths," Radio Science, Vol. 13, p. 471.
- Flock, W.L. (1987), "Propagation Effects on Satellite Systems at Frequencies Below 10 GHz - A Handbook for Satellite Systems Design," Second Edition, NASA Reference Publication 1108 (02), December 1987.
- Flock, W.L., S.D. Slobin, and E.K. Smith (1982), "Propagation Effects on Radio Range and Noise in Earth-Space Telecommunications," Radio Science, Vol. 17, pp. 1141-1144, Nov.-Dec. 1982.
- Freeny, A.E. and J.D. Gabbe (1969), "A Statistical Description of Intense Rainfall," Bell System Technical Journal, Vol. 48, p 1 7 8 9 .
- Funakawa K. and Y. Otsu (1974), "Characteristics of Slant Path Rain Attenuation at 35 GHz Obtained by Solar Radiation and

- Ghobrial, S.I., I.A. Ali, and H.M. Hussein (1978), "Microwave Attenuation in Sandstorms," Summaries of Papers, 1978 International Symposium on Antennas and Propagation, Sendai, Japan.
- Gibbins, C.J. (1986), "Improved Algorithms for the Determination of Specific Attenuation as Sea Level by Dry Air and Water Vapor, in the Frequency Range 1-350 GHz," Radio Science, Vol. 21, pp. 949-954, Nov.-Dec. 1986.
- Goldhirsh, J. (1976), "Path Attenuation Statistics Influenced by Orientation of Rain Cells (1976)," IEEE Trans. Ant. Prop., Vol. AP-24, p. 792.
- Goldhirsh, J. (1982), "A parameter review and assesment of attenuation and backscatter properties associated with dust storms over desert regions in the frequency range of 1 to 10 GHz," IEEE Trans. on Ant. and Prop., Vol. AP-30, pp. 1121-1127.
- Gumbel, E.J. (1958), Statistics of Extremes, Columbia Univ. Press, New York, New York.
- Gutteberg, O. (1981), "Measurement of Tropospheric Fading and Cross-polarization in the Artic using Orbital Test Satellite," IEE Conf. Publ. No. 195, Part 2, IEE Second Int. Conf. on Antennas and Propagation, Heslington, York, U.K., pp. 71-75.
- Hall, J.E. and J.E. Allnutt (1975), "Results of Site Diversity Tests Applicable to 12 GHZ Satellite Communications," IEE Conference Publication No. 126, Satellite Communication Systems Technology, London.
- Harris, J.M. (1977), "Tropospheric Scintillation of Microwaves Propagated on Low Elevation Angle Earth-space Path," COMSAT Tech. Memo CL-54-77.
- Hendry, A., G.C. McCormick and B.L. Barge (1976), "Ku-Band and S-Band Observations of the Differential Propagation Constant in Snow," IEEE Trans. Ant. Prop., Vol. AP-24, No. 4, pp. 521-525.
- Hedge, D.B., D.M. Theobold, and R.C. Taylor (1976b), "ATS-6 Millimeter Wavelength Propagation Experiment,tl Ohio State University, ElectroScience Laboratory, Rept. 3863-6.
- Hogg, D.C. (1968), "Millimeter Wave Communication through the Atmosphere," Science, Vol. 159, p. 39.
- Hogg, D.C. and T.S. Chu (1975), "The Role of Rain in Satellite Communications ," Proc. IEEE, Vol. 63, No. 9, pp. 1307-1331.

- Hopfield, H.S. (1971), "Tropospheric Effect on Electromagnetically Measure Range: Prediction from Surface Weather Data," Radio Science, Vol. 6, pp. 357-367.
- Hyde, G. (1976), "Data Analysis Report - ATS-F Comsat Millimeter Wave Propagation Experiment," Comsat Laboratories, Clarksburg, Maryland.
- Ippolito, L.J. (1976), "20 and 30 GHz Millimeter Wave Experiments with the ATS-6 Satellite," NASA Tech. Note TN D-8197, April 1976.
- Ippolito, L. J. (1979), "11.7 GHz Attenuation and Rain Rate Measurements with the Communications Technology Satellite (CTS), NASA TM 80283, Goddard Space Flight Center, Greenbelt, MD.
- Ippolito, L.J. (1986), Radiowave Propagation in Satellite Communications, Van Nostrand Reinhold, New York.
- Ishimaru, A. (1978), Wave Propagation and Scattering in Random Media, Single Scattering and Transport Theory, Vol. 1, Academic Press, New York, N. Y.
- Johannsen, K.G. and A. Koury (1974), "The Moon as a Source for G/T Measurements," IEEE Trans. Aerosp. Elect. Syst., Vol. AES-10, No. 5, pp. 718-727.
- Kaul, R. (1980), "Extension of an Empirical Site Diversity Relation to Varying Rain Regions and Frequencies," URSI Commission F Symposium, Lennoxville, Quebec.
- Kobayashi, T. (1977), "Degradation of cross-polarization isolation due to rain," J. of Radio Research Labs. (Japan), Vol. 24, No. 114, pp. 101-107.
- Koester K L and L H Kosowsky (1970), "Attenuation of Millimeter Waves in Fog," Fourteenth Radar Meteorology Conference, November 17-20, Tuscon, Arizona.
- Koester, K.L. and L.H. Kosowsky (1978), "Millimeter Wave Propagation in Ocean Fogs and Mists," proceedings IEEE Ant. Prop. Symposium.
- Kraus, J.D. (1966), Radio Astronomy, McGraw-Hill Book Co., New York.
 LeFrancois, G.L., Martin and M.: Rooryck (1973), "Influence de la Propagation Sur la Valeur de Decouplage de Deux Polarisations Orthogonales," Ann. des Telecomm., Vol. 28, July-August, in French.
- Liebe, H.J. (1975), "Molecular Transfer Characteristics of Air Between 40 and 140 GHz," IEEE Trans. Microwave Theory and Techniques, MTT-23, No. 4.
- Lo, Lai-Inn, B.M. Fannin and A.W. Straiton (1975), "Attenuation of

- Lo, P.S.L., O.P. Banjo, and E. Vilar (1984), "observations of Amplitude Scintillations on a Low Elevation Earth-space Path," Electronics Letters, Vol. 20, No. 7, pp. 307-308.
- Lord, L.H. and R. Oliver (1946), "An Experimental Investigation of the Reflection and Absorption of Radiation of 9-cm Wavelength," Proc. Phys. Soc., Vol. 58, pp. 265-280.
- Marini, J.W. (1972a), "Correction of Satellite Tracking Data for an Arbitrary Tropospheric Profile," Radio Science, Vol. 7, pp. 223-231.
- Marini, J.W. (1972b), "Tropospheric Range-Rate Tracking Data Correction," NASA/Goddard Space Flight Center, Dec. X-551-72-277 .
- Mason, B.J. (1971), The Physics of Clouds, Clarendon Press, Oxford, pp.119-121.
- McCormick, K.S. and L.A. Maynard (1972), "Measurements of SHF Tropospheric Fading Along Earth Paths at Low Elevation Angles," Electronics Letters, Vol. 8, No. 10.
- McEwan, N.J., P.A. Watson, A.W. Dissanayake, D.P. HaWorth and V.T. Vakili (1977) , "Crosspolarization from High Altitude Hydrometers on a 20 GHz Satellite Radio Path," Electronics Letters, Vol. 13, pp. 1314.
- Muchmore, R.B. and A.D. Wheelon (1955), "Line-of-Sight Propagation Phenomena - I. Ray Treatment," Proc. IRE. Vol. 43, pp. 1437-1449.
- Njoku, E.G. and E.K. Smith (1985), "Microwave Antenna Temperature of the Earth from Geostationary Orbit," Radio Science, Vol. 20, No. 3, pp. 591-599.
- Nowland, W.L., R.L. Olsen and I.P. Shkarofsky (1977a), "Theoretical Relationship Between Rain Depolarization and Attenuation," Electronics Letters, Vol. 13, No. 22, pp. 676-677.
- Nowland, W.L., I.I. Strickland, J. Schlesak and R.L. Olsen (1977b), "Measurements of Depolarization and Attenuation at 11.7 GHz by Using the Communications Technology Satellite," Electronics Letters, Vol. 13, No. 24, pp. 750-751.
- Nusple, POP., N.G. Davies and R.L. Olsen (1975), "Ranging and Synchronization Accuracies in a Regional TDMA Experiment," Proc. Third Intl. Digital Satellite Comm. Conf., Kyoto, Japan.
- Oguchi, T. (1977) , "Scattering Properties of Pruppacher and Pitter Form Raindrops and Cross Polarization Due to Rain:

Calculations at 11, 13, 19.3 and 34.8 GHz," Radio Science, Vol. 12, No. 1, pp. 41-51, Jan.-Feb. 1977.

- Olsen, R.L., D.V. Rogers and D.B. Hedge (1978), "The aR^b Relation in the Calculation of Rain Attenuation," IEEE Trans. Ant. Prop., AP-26, pp. 318-329.
- Pruppacher, H.R. and R.L. Pitter (1971), "A Semi-empirical Determination of the Shape of Cloud and Rain Drops," J. Atmos. Science, Vol. 28, pp. 86-94.
- Radio Regulations, International Telecommunication Union, Geneva.
- Rice, P.L. and N.R. Holmberg (1973), "Cumulative Time Statistics of Surface Point Rainfall Rates," IEEE Trans. Comm., Vol. COM-21, No. 10; pp. 1131-1136.
- Rogers, D.V. (1981), "Diversity- and Single-Site Radiometric" Measurements of 12-GHz Rain Attenuation in Different Climates," IEE Conference Publication No. 195, International Conf. on Ant. & Prop., AP-26 U.K. pp. 3.18-123.
- Rogers, R.R. 1976, A Short Course in Cloud Physics, Chapter 12, Pergamon Press, London.
- Segal, B. and R.E. Barrington (1977), Tropospheric Refractivity Atlas for Canada, Dept. of Communications, CRC Report No. 1315-E, Ottawa.
- Shutie, P.F., J.E. Allnutt and E.C. MacKenzie (1977), "Depolarization Results at 30 GHz Using Transmissions from the ATS-6 Satellite," Proc. URSI Symposium on Propagation in Non-Ionized Media, La Baule, France, April 28 - May 6, pp. 367-369.
- Shutie, P.F., E.C. MacKenzie and J.E. Allnutt (1978), "Relative Phase Measurement at 30 GHz Between Copolar and Induced Crosspolar Signals Produced by Ice Particles on a Satellite-to-Ground Link," Electronics Letters, Vol. 14, No. 4, pp. 105-107.
- Slobin, S.D. (1982), "Microwave noise temperature and attenuation in clouds : Statistics of these effects at various sites in the United States, Alaska, and Hawaii," Radio Science, Vol. 17, pp. 1443-1454, Nov.-Dec. 1982.
- Smith, E.K. (1982), "Centimeter and Millimeter Wave Attenuation and Brightness Temperature due to Atmospheric Oxygen and Water Vapor," Radio Science, Vol. 17, No. 6, pp. 1455-1464.
- Spaulding, A.D., G.H. Hagn (1978), "Worldwide Minimum Environmental Radio Noise Levels (0.1 Hz to 100 GHz)," Symposium Proceedings, Effects of the Ionosphere on Space and Terrestrial Systems, J.M. Goodwin, Ed., ONR/NRL, pp. 177-182, Jan. 24-26, 1978.

- Strickland, J.I. (1974), "Radar Measurements of Site Diversity Improvement During Precipitation," Journal de Recherches Atmospherique, Vol. 8, p. 45.
- Strickland, J.I., R.I. Olsen and H.L. Werstiuk (1977), "Measurements of Low Angle Fading in the Canadian Arctic," Ann. Telecomm., Vol. 32, Nos. 11-12, pp. 530-535.
- Strickland, R.I., R.O. Olsen, and H.L. Werstiuk, (1977), "Measurements of Low Angle Fading in the Canadian Arctic," Ann. des Telecomm., Vol. 11-12, pp. 530-535.
- Stutzman, W.L., C.W. Bostian, C.W. Manus, E.A. Marshall, and P.H. Wiley (1975), "ATS-6 Satellite 20 GHz Propagation Measurements at Low Elevation Angles," Electronics Letters, Vol. 11, pp. 635-636.
- Stutzman, W.L. (1977), "Mathematical Formulations and Definitions for Dual Polarized Reception of a Wave Passing Through a Depolarizing Medium (A Polarization Primer)," Virginia Polytechnic & State Univ., prepared under NASA Contract NAS5-22577.
- Suzuki, Y., T. Shinozuka, H. Kuroiwa, H. Inomata (1982), "TDMA Site Diversity Switching Experiments with Japanese CS," Record, International Conference on Communication, Philadelphia, PA.
- Tang, D.D., D. Davidson, and S.C. Bloch (1982), "Diversity Reception of COMSTAR Satellite 19/29 - GHz Beacons with the Tampa Triad, 1978-1981," Radio Science, Vol. 17, No. 6, pp. 1477-1488.
- Tatarski, V.I. (1961), Wave Propagation in a Turbulent Medium, McGraw-Hill Book Co., New York N. Y.
- Theobald, D.M. (1978), "Tropospheric Refraction," report prepared for ORI, Inc. under NASA Contract NASS-23438.
- Theobald, D.M. and D.B. Hedge (1978), "Gain Degradation and Amplitude Scintillation Due to Tropospheric Turbulence," The Ohio State University ElectroScience Lab., Tech. Rpt. 784229-6, Revision 1.
- Thompson, M.C., Jr., L.E. Woods, H.B. Janes and D. Smith (1975), "Phase and Amplitude Scintillations in the 10 to 40 GHz Band," IEEE Trans. Ant. Prop., Vol. AP-23, pp. 792-797.
- Towner, G.C., R.E. Marshall, W.L. Stutzmann, C.W. Bostian, T. Pratt, E.A. Manus, P.H. Wiley (1982), "Initial Results from the VPI and SU SIRIO Diversity Experiment," Radio Science, Vol. 17, No. 6, pp. 1489-1494.
- Turner, D.J.W. (1973), "Measurements of Cross-Polar Discrimination at 22 and 37 GHz," IEE Conf. Proc. No. 98.

- U.S. Dept. of Commerce (1947), Weather Bureau, "Maximum Recorded United States Point Rainfall," Tech. Paper No. 2, Washington, D.C.
- U.S. Dept. of Commerce (1955), Weather Bureau, "Rainfall Intensity-Duration-Frequency Curves," Tech. Paper No. 25, Washington, D.C.
- Vogel, W.J. (1978), CTS Attenuation and Cross-Polarization Measurements at 11.7 GHz, Final Report, Elect. Eng. Res. Lab., Univ. Texas at Austin, prepared under NASA Contract NAS5-22576.
- Vogel, W.J., A.W. Straiton, B.M. Fannin and N.K. Wagner (1976), "Attenuation Diversity Measurements at 20 and 30 GHz," Radio Science, Vol. 11, p. 167.
- Vogel, W.J., A.W. Straiton and B.M. Fannin (1977), "ATS-6 Ascending: Near Horizon Measurements Over Water at 30 GHz," Radio Science, Vol. 12, September-October, pp. 757-765.
- Wait, D.F., W.C. Daywitt, M. Kanda and C.K.S. Miller (1974), A Study of the Measurement of G/T Using Casseopeia A, National Bureau of Standards, Rept. No. NBSIR 74-382.
- Waters, J.W. (1976), "Absorption and Emissions by Atmospheric Gases," Methods of Experimental Physics, Vol. 12B, Radio Telescopes, Ed. M. L. Meeks, Academic Press, New York, NY.
- Watson, P.A. and M. Arbabi (1973), "Cross-polarization Isolation and Discrimination," Electronics Letters, Vol. 9, No. 22, pp. 516-517.
- Watson, P.A., F. Goodall and M. Arbabi (1973), "Linear Cross-Polarization and Attenuation Measurements at 11 and 36 GHz," IEE Conf. Proc. No. 98.
- Webber, R.V., and K.S. McCormick (1980), "Low Angle Measurements of the ATS-6 Beacons at 4 and 30 GHz," Proc. URSI (Commission F) International Symposium on Effects of the Lower Atmosphere on Radio Propagation at Frequencies Above 1 GHz, Lennoxville, Canada.
- Webster, W.J., Jr., T.T. Wilheit, T.C. Chang, P. Gloersen and T.J. Schmutge (1975), "A Radio Picture of the Earth," Sky and Telescope, Vol. 49, No. 1, pp. 14-16.
- WEC (Westinghouse Electric Corporation) (1975), "ATS-6 Millimeter Wave Propagation Experiment - Final Data Analysis Report," Baltimore, Md., prepared under NASA/GSFC Contract NAS5-20904.
- Weickmann, H. and H.J. aufm Kampe (1953), "Physical Properties of Cumulus Clouds," Journal of Meteorology, vol. 10.

- Wulfsberg, K.N. (1964), "Apparent Sky Temperatures at Millimeter-Wave-Frequencies, " Phys. Science Res. Paper No. 38, Air Force Cambridge Res. Lab., No. 64-590.
- Wulfsberg, K.N. (1973), "Path Diversity for mm-wave Earth-to-Satellite Links," Radio Science, Vol. 8, p. 1.
- Yamada, M. and H. Yokoi (1974), "Measurements of Earth-Space Propagation Characteristics at 15.5 and 31.6 GHz Using Celestial Radio Sources," Elect. and Comm. in Japan, Vol. 57-B, p. 2.
- Yokoi, H., M. Yamada and T. Satoh (1970), "Atmospheric Attenuation and Scintillation of Microwaves from Outer Space," Astronomical Society, Japan, Vol. 22, pp. 511-524.